ADVANCED MATERIALS
www.advmat.de

Sulfide-Based Solid-State Electrolytes: Synthesis, Stability, and Potential for All-Solid-State Batteries

Qing Zhang, Daxian Cao, Yi Ma, Avi Natan, Peter Aurora, and Hongli Zhu**

Due to their high ionic conductivity and adeciduate mechanical features for lamination, sulfide composites have received increasing attention as solid electrolyte in all-solid-state batteries. Their smaller electronegativity and binding energy to Li ions and bigger atomic radius provide high ionic conductivity and make them attractive for practical applications. In recent years, noticeable efforts have been made to develop high-performance sulfide solid-state electrolytes. However, sulfide solid-state electrolytes still face numerous challenges including: 1) the need for a higher stability voltage window, 2) a better electrode–electrolyte interface and air stability, and 3) a cost-effective approach for large-scale manufacturing. Herein, a comprehensive update on the properties (structural and chemical), synthesis of sulfide solid-state electrolytes, and the development of sulfide-based all-solid-state batteries is provided, including electrochemical and chemical stability, interface stabilization, and their applications in high performance and safe energy storage.

1. Introduction

Driven by the increasing demand for energy worldwide, development of high-energy and high-power energy storage devices that are also safe and reliable is at the forefront of energy research. Since their invention, lithium-ion batteries (LIB) have been the dominating energy storage solution for portable electronics and electric vehicles, because of their high energy density and cyclability compared to other rechargeable battery systems.[1] After continuous developments on the LIB technologies, the specific energy and energy density of a LIB at cell level can reach 256 Wh kg^{-1} and 697 Wh $L^{-1,}$ respectively.[2] However, to achieve mass utilization, the goals for electric vehicles' advanced batteries set by the U.S. Department of Energy and U.S. Advanced Battery Consortium are 350 Wh kg^{-1} and 750 Wh L^{-1} at cell level, and 235 Wh kg^{-1} and 500 Wh L^{-1} at system level by 2020.[3] In order to fulfill these requirements, improvements to the whole battery system, including anode materials, cathode materials and electrolytes and separators, are currently being researched.[4]

Conventional LIBs use organic liquid electrolytes (OLEs), which consist of a lithium salt such as lithium hexafluorophosphate ($LiPF_6$) dissolved in organic solvents such as ethylene carbonate (EC) and dimethyl carbonate (DMC).[5] The high flammability of organic solvents (EC flash point 150 °C and DMC flash point 18 °C) presents safety risks during battery operation.[6] Further, OLEs are depleted during charge/discharge cycles, due to the repeated breakdown and reformation of solid electrolyte interphase (SEI) films. Therefore, conventional batteries with OLEs normally contain extra electrolyte to overcome depletion during extended cycling, which increases manufacturing costs.

Due to the limitations of the aforementioned OLEs, current LIB technologies are not able to meet the higher energy density and better safety required for existing and new applications. The ideal battery, that meets these new needs, will be made with a solid-state electrolyte (SSE), a Li metal anode and a high-voltage cathode, what is known as an all-solid-state battery (ASSB). Most SSEs are nonflammable and have a wider operating temperature range, making them much safer than their liquid counterparts in the event of short circuiting.[7] It is worth noting that in ASSBs, battery module structures can be simplified by stacking bipolar electrodes and solid electrolyte in alternating layers in a single battery case, which reduces number of battery cases as what is needed in liquid batteries.[8] Based on a cell-level calculation of lithium–sulfur chemistry, at the same areal capacity, cells employing SSE could double the gravimetric energy density of cells with conventional liquid electrolyte.[9] As shown in the Ragone plots in **Figure 1**a, the LIBs with liquid cells cannot achieve high energy and high power simultaneously. Whereas ASSBs showed obvious advantages in energy and power.[10]

Conventional OLE, $LiPF_6$ in EC/DMC, exhibits an ionic conductivity of 1×10^{-2} S cm^{-1} at room temperature,[11] and lithium bis-(trifluromethanesulfonyl)imide (LiTFSI) in carbonate systems exhibits- an ionic conductivity in the range of 2.1×10^{-3} to 5.8×10^{-3} S cm^{-1} at room temperature.[12,13] In contrast, solid electrolyte, lithium phosphorous oxynitride (LiPON) exhibits a much lower ionic conductivity of $\approx 10^{-6}$ S cm^{-1} compared to

Dr. Q. Zhang, Dr. P. Aurora
Kostas Research Institute
LLC at Northeastern University
141 South Bedford St, Burlington, MA 01803, USA
E-mail: paurora@umich.edu
Dr. Q. Zhang, D. Cao, Y. Ma, A. Natan, Prof. H. Zhu
Department of Industrial and Mechanical Engineering
Northeastern University
360 Huntington Ave, Boston, MA 02115, USA
E-mail: h.zhu@neu.edu
The ORCID identification number(s) for the author(s) of this article can be found under https://doi.org/10.1002/adma.201901131.

DOI: 10.1002/adma.201901131

their liquid counterparts.[14] However, there have been new discoveries and advancement of SSE classes, such as the improved oxide SSEs with garnet-like structures which can reach the an ionic conductivity in the range of $\approx 10^{-3}$–10^{-4} S cm^{-1}.[15] The ionic conductivity of sulfide-based SSEs have reached $\approx 10^{-2}$ S cm^{-1}, which is comparable to the OLEs (Figure 1b).[16–19] Furthermore, unlike in OLEs where Li ions move in solvated shells, the ions migrate via ionic motion across the crystal lattice in SSEs. This is why SSEs are usually single-ion conductors with higher Li transference number (close to one), compared to the that of OLEs (≈0.4–0.5).[13] Because of that, the ion conduction of some SSEs have the ability to surpass that of OLEs.[6]

In order to achieve high ionic conductivity, a crystal has to satisfy several conditions: i) there must be a large number of mobile ions for conducting; ii) there must be a large number of available sites for the mobile ions to migrate; iii) the occupied and empty sites must be energetically similar so the mobile ions do not have to overcome a large energy barrier to migrate; iv) the structure of a good ionic conductor must has relatively open channels that can act as conduction pathways.[24–26] Usually highly polarizable anion frameworks are preferable for ion conduction, which is why sulfide materials display the highest ionic conductivities (up to $\approx 10^{-2}$ S cm^{-1}) among the various categories of discovered SSEs, as seen in Figure 1b.[10,16] Compared to oxygen atoms, sulfur atoms have a lower electronegativity and binding energy to Li ions, which makes Li ions more mobile in sulfide than oxide lattice structures. On top of that, sulfur has a bigger atomic radius which creates larger channels for Li ion conduction in the crystal lattice.[24,25] Moreover, sulfide materials are softer and more malleable than oxide materials. They can be densely packed by cold-pressing, during which process the particles gain close contact and grain boundary resistances can be neglected.[27] Typical types of sulfide SSEs are glassy Li–P–S (LPS) sulfides,[28] glass ceramics derived from the LPS glass systems,[29] argyrodite Li_6PS_5X,[30] thio-LISICONs (lithium superionic conductor) and similar compounds,[24] and $Li_{10}GeP_2S_{12}$ (LGPS) and similar compounds.[16,31] The sulfide material with the highest ionic conductivity discovered so far is $Li_{9.54}Si_{1.74}P_{1.44}S_{11.7}Cl_{0.3}$, which demonstrates an ionic conductivity of 2.5×10^{-2} S cm^{-1} at room temperature.[10] Another superionic conductor is $Li_{10}GeP_2S_{12}$, which has an ionic conductivity of 1.2×10^{-2} S cm^{-1} at room temperature.[16] Other groups such as argyrodite Li_6PS_5Cl and $Li_7P_3S_{11}$ also have conductivities higher than 10^{-3} S cm^{-1}.[30,32]

Regarding crystal structure and coordination environment, Wang et al. found that a body-center cubic (bcc) anion framework (primarily the tetrahedral sites) is the most desirable for Li ion conduction. This crystal structure allows Li to hop between neighboring tetrahedral sites. For example, Wang et al. discovered that Li ions are more stable in tetrahedral sites in sulfide conductors. Furthermore, Li ions migrate significantly easier between two face-sharing tetrahedral sites in bcc frameworks. In comparison, Li migration between two tetrahedral sites in face-center cubic (fcc) and hexagonal close-packed (hcp) lattices must go through an intermediate octahedral site which means much higher energy barriers. Superconducting sulfides LGPS and $Li_7P_3S_{11}$ can be very well matched to a bcc anion framework. While argyrodites Li_6PS_5X do not have bcc lattices, they consist entirely of tetrahedral

Qing Zhang is currently a postdoctoral research associate with Kostas Research Institute at Northeastern University. She is working on the development of all-solid-state batteries using superionic solid-state electrolytes and high-energy cathode materials. She received her Ph.D. degree in materials science and engineering from Stony Brook University. Her doctoral research was to investigate materials for lithium-based batteries and beyond with a focus on understanding the structural and interfacial properties of the materials.

Peter Aurora conducted his doctoral and postdoctoral research at the University of Michigan. Currently, he is a lead scientist at Cabot Corporation in the energy materials division. His work focuses on the R&D of lithium and beyond-lithium batteries, supercapacitors, fuel cells, and solar-energy devices. Prior to this, he was a senior research scientist at the Kostas Research Institute at Northeastern University focusing on advanced energy storage systems. He has over 12 years of experience in energy generation and storage as a scientist and expert in engineering, research and development, and test and evaluation.

Hongli (Julie) Zhu is currently an assistant professor at Northeastern University. Her group works on electrochemical energy storage, biomass-derived multifunctional materials, and emerging advanced manufacturing technologies. From 2012 to 2015, she worked at the University of Maryland as a post doc, focusing on the research of flexible nanopaper electronics and energy storage. From 2009 to 2011, she conducted research on materials science and processing of biodegradable and renewable biomaterials from natural wood in the KTH Royal Institute of Technology in Sweden. Her expertise is on the research of environmentally friendly natural materials and energy storage, design, and application of transparent nanostructured paper for flexible electronics, and R2R manufacturing. In energy storage, her group works extensively on flow batteries, solid-state batteries, and alkali metal ion batteries, such as Li^+, Na^+, K^+ batteries.

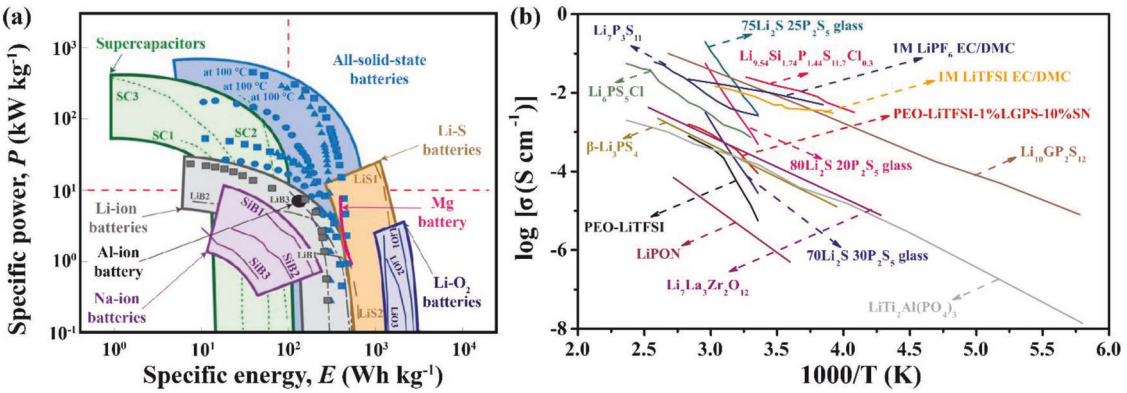

Figure 1. a) Ragone plots of ASSBs, conventional batteries and capacitors. Reproduced with permission.[10] Copyright 2016, Springer Nature Publishing AG. b) Arrhenius of SSEs compared to OLEs. Data from the following references are combined and replotted here: $Li_{9.54}Si_{1.74}P_{1.44}S_{11.7}Cl_{0.3}$;[10] $Li_{10}GeP_2S_{12}$;[16] $Li_7P_{2.9}S_{10.85}Mo_{0.01}$, $Li_7P_3S_{11}$;[18] PEO–LiTFSI–1%LGPS–10%SN, PEO-LiTFSI;[20] $70Li_2S{\cdot}30P_2S_5$ glasses, $75Li_2S{\cdot}25P_2S_5$ glasses, and $80Li_2S{\cdot}20P_2S_5$ glasses;[21] β-Li_3PS_4;[22] $Li_6PS_5Cl_{0.5}Br_{0.5}$, Li_6PS_5Cl;[23a] 1M LiTFSI EC/DMC, 1M $LiPF_6$ EC/DMC;[23b] LiPON;[23c] $Li_7La_3Zr_2O_{12}$;[23d] $LiTi_2Al(PO_4)_3$.[23e]

sites, which allow for Li ion conduction through face-sharing tetrahedral sites.[33]

Conventionally, the understanding of fast ionic conduction in superionic crystals is based on diffusion of individual ions, which occurs through hopping within the crystal lattice and thermally introduced disordering.[34] According to the Arrhenius equation, where σ is ionic conductivity, T is temperature, A is a pre-exponential factor, n is the concentration of mobile-ion carriers, E_a is the activation of thermally activation process and k_B is the Boltzman constant, a linear relationship can be established between $\log\sigma T$ and $\frac{1}{T}$, Equation (1)[35]

$$\sigma = \frac{A}{T} n \exp\left(-\frac{E_a}{k_B T}\right) \quad (1)$$

Point defects, such as Schottky and Frenkel, play a key role in ion conduction in crystals. The vacancies and interstitial atoms associated with these point defects are the dominant diffusion carriers for ion conduction. Point defects or structural disordering usually occur when the crystallographic sites are partially occupied and when aliovalent substitution in the structure creates vacancies.[36] Using ab initio modelling, He et al. showed that for superionic conductors, conduction occurs through concerted migration of multiple ions at low energy barrier, and not isolated ion hopping. The low energy barrier of multi-ion diffusion is the result of unique mobile ion configuration with high energy ion occupancy. The energy of mobile ions decreases during the concerted diffusion, which explains why the diffusion process maintains a low energy barrier.[37] Then, He's group proposed that the strategy for making superionic conductors is to insert ions into the high energy sites, which could activate concerted diffusion with low energy barrier.[37]

We begin with a systematic examination of several sulfide SSE systems, including LPS glass, LPS glass ceramics, argyrodite Li_6PS_5X (X = Cl, Br, and I), and thio-LISICONs $Li_{4-x}Ge_{1-x}P_xS_{4-x}$ and $Li_{11-x}M_{2-x}P_{1+x}S_{12}$ (M = Ge, Sn, and Si) compounds. The ionic conductivities of these sulfide systems have been summarized and ion conduction mechanisms were elucidated based on crystalline structure. We follow with an analysis of the advantages and disadvantages of different synthesis processes and their resulting ionic conductivities. Further, we highlight the intrinsic electrochemical and chemical stabilities of sulfides against Li metal, cathode materials, and humid air. In this section, we also include corresponding approaches to improve the chemical compatibility of sulfides. In the ASSBs' section, we summarize promising results for ASSBs published in the last 10 years, which we consider essential to understand the current research progress of sulfide-based ASSBs. Last, relevant reports on potential methods for the scalable manufacturing of the sulfide based ASSBs were reviewed, providing good understanding of large-scale production and application of ASSBs.

2. Sulfide-Based Solid-State Electrolytes

This section will feature a review of the structure and ion conduction mechanisms of several types of sulfide SSEs, including Li–P–S-based glasses and glass ceramics, Li_6PS_5X (X = Cl, Br, or I) argyrodites, thio-LISICONs, $Li_{11-x}M_{2-x}P_{1+x}S_{12}$ (M = Ge, Sn, and Si) compounds and composite SSEs. **Table 1** provides a detailed summarization of the ionic conductivity and activation energy of the SSEs.

2.1. Glasses

Inorganic glass materials are generally believed to have higher ionic conductivity than their corresponding crystalline materials, because of their open structure and large free volume. The most well-studied glass sulfides are the binary $xLi_2S{\cdot}(100 - x)P_2S_5$ system (x = mole percentage), where single phase glass was found to form between $x = 0.4$ and $x = 0.8$.[28,38] As shown in **Figure 2**, according to Dietrich's study, $xLi_2S{\cdot}(100-x)P_2S_5$ glass of different Li_2S content is consisted of different building blocks. Glass with lower Li_2S content ($x \leq 60$) has more di-tetrahedral $P_2S_7^{4-}$ units, which has

Table 1. Ionic conductivity of sulfide-based solid electrolytes.

Material	σ_{RT} [S cm^{-1}]	*Ea*	Reference
$60Li_2S{\cdot}40P_2S_5$ glass	3.2×10^{-6}	50.7 kJ mol^{-1}	[21]
$67Li_2S{\cdot}33P_2S_5$ glass	3.8×10^{-5}	42.3 kJ mol^{-1}	[21]
$70Li_2S{\cdot}30P_2S_5$ glass	3.7×10^{-5}	43.5 kJ mol^{-1}	[21]
$75Li_2S{\cdot}25P_2S_5$ glass	2.8×10^{-4}	38.5 kJ mol^{-1}	[21]
$80Li_2S{\cdot}20P_2S_5$ glass	1.3×10^{-4}	42.3 kJ mol^{-1}	[21]
$55(66Li_2S{\cdot}33P_2S_5){\cdot}45LiI$ glass	10^{-3}	7 kcal mol^{-1}	[47]
$95(60Li_2S{\cdot}40SiS_2){\cdot}5Li_3BO_3(Li_3AlO_3)$ glass	10^{-3}	28 kJ mol^{-1}	[45]
$77(75Li_2S{\cdot}\ 25P_2S_5){\cdot}33LiBH_4$ glass	1.6×10^{-3}	N/A	[46]
$40Li_2S{\cdot}\ 28SiS_2{\cdot}30LiI$ glass	1.8×10^{-3}	N/A	[49]
$30Li_2S{\cdot}\ 26B_2S_3{\cdot}33LiI$ glass	1.7×10^{-3}	N/A	[50]
$Li_7P_3S_{11}$	3.2×10^{-3}	12 kJ mol^{-1}	[52]
$Li_7P_3S_{11}$ analogue $Li_7P_{2.9}S_{10.85}Mo_{0.01}$	4.8×10^{-3}	22.7 kJ mol^{-1}	[18]
$Li_7P_3S_{11}$ analogue $Li_7P_{2.9}Mn_{0.1}S_{10.7}I_{0.3}$	5.6×10^{-3}	20.8 kJ mol^{-1}	[56]
Argyrodite Li_6PS_5Cl (cal.)	1.9×10^{-3}	0.22 eV	[67]
Argyrodite Li_6PS_5Br (cal.)	6.8×10^{-3}	0.27 eV	[67]
Argyrodite Li_6PS_5I (cal.)	4.6×10^{-7}	0.32 eV	[67]
Argyrodite Li_7PS_6	1.6×10^{-6}	0.16 eV	[74]
Argyrodite $Li_7Ge_3PS_{12}$	1.1×10^{-4}	25 kJ mol^{-1}	[73]
Argyrodite $Li_{6.35}P_{0.65}Si_{0.35}S_5Br$	2.4×10^{-3}	0.15 eV	[71]
Argyrodite $Li_{6.6}P_{0.4}Ge_{0.6}S_5I$	5.4×10^{-3}	0.16 eV	[72]
Thio-LiSICON $Li_{3.25}Ge_{0.25}P_{0.75}S_4$	2.2×10^{-3}	20 kJ mol^{-1}	[24]
Thio-LiSICON analogue Li_4SnS_4	7.0×10^{-5}	0.41 eV	[77]
Thio LiSICON analogue $Li_{11}AlP_2S_{12}$	8.0×10^{-4}	25.4 kJ mol^{-1}	[80]
Thio-LiSICON analogue $Li_{3.833}Sn_{0.833}As_{0.166}S_4$	1.4×10^{-3}	0.21 eV	[78]
$Li_{10}GeP_2S_{12}$	1.2×10^{-2}	24 kJ mol^{-1}	[16]
LGPS analogue $Li_{10}SnP_2S_{12}$	4×10^{-3}	0.60 eV	[17]
LGPS analogue $Li_{10}SiP_2S_{12}$	2.3×10^{-3}	0.196 eV	[87]
LGPS analogue $Li_{9.54}Si_{1.74}P_{1.44}S_{11.7}Cl_{0.3}$	2.5×10^{-2}	23 kJ mol^{-1}	[10]
$70Li_2S{\cdot}30P_2S_5$-1,4-butanediol	9.7×10^{-5}	34 kJ mol^{-1}	[90]
$75Li_2S{\cdot}25P_2S_5$-PFPE	10^{-4}	N/A	[93]
$77.5Li_2S{\cdot}22.5P_2S_5$-methly-imine	9.2×10^{-5}	34.8 kJ mol^{-1}	[95]
(PEO_{18}-LiTFSI)–LGPS (LGPS 1 wt%)	1.2×10^{-5}	112 kJ mol^{-1}	[97]
(PEO_{18}-LiTFSI)–LGPS (LGPS 1 wt%)–SN (SN 10 wt %)	9.1×10^{-5}	82.77 kJ mol^{-1}	[20]
β-Li_3PS_4 –LZNO (2 wt%)	2.4×10^{-4}	N/A	[98]
β-Li_3PS_4–Al_2O_3 (2 wt%)	2.3×10^{-4}	N/A	[98]
β-Li_3PS_4–SiO_2 (2 wt%)	1.8×10^{-4}	N/A	[98]
β-Li_3PS_4–LLZO (30 wt%)	1.8×10^{-4}	N/A	[99]

one bridging S atom and three terminal S atoms in each unit. Conversely, glass with higher Li_2S ($x \geq 70$) has more monotetrahedral PS_4^{3-} units, where all the S atoms are terminal. $75Li_2S\cdot25P_2S_5$ glass with only PS_4^{3-} units showed the highest ionic conductivity, 2.8×10^{-4} S cm^{-1} at room temperature.[21] The $75Li_2S\cdot25P_2S_5$ glass was reported in other studies to have similar ionic conductivities, in the range of 10^{-4} S cm^{-1}.[39] The decrease in crystallinity when x is higher than 75 is likely due to the presence of crystalline Li_2S, which hinders Li^+ ion conduction.[28] Other binary glass systems such as $xLi_2S\cdot(100-x)B_2S_3$ and $xLi_2S\cdot(100-x)SiS_2$ of wide composition ranges have been developed with ionic conductivities of $\approx10^{-4}$ S cm^{-1} at room temperature.[38,40] On the other hand, $xLi_2S\cdot(100-x)GeS_2$ has shown lower ionic conductivity in the range of $\approx10^{-5}$–10^{-7} S cm^{-1}.[41]

In the glass systems, ionic conductivity can be improved by increasing the concentration and mobility of charge carrier ions in the SSE system.[42] Doping the glass electrolytes with lithium

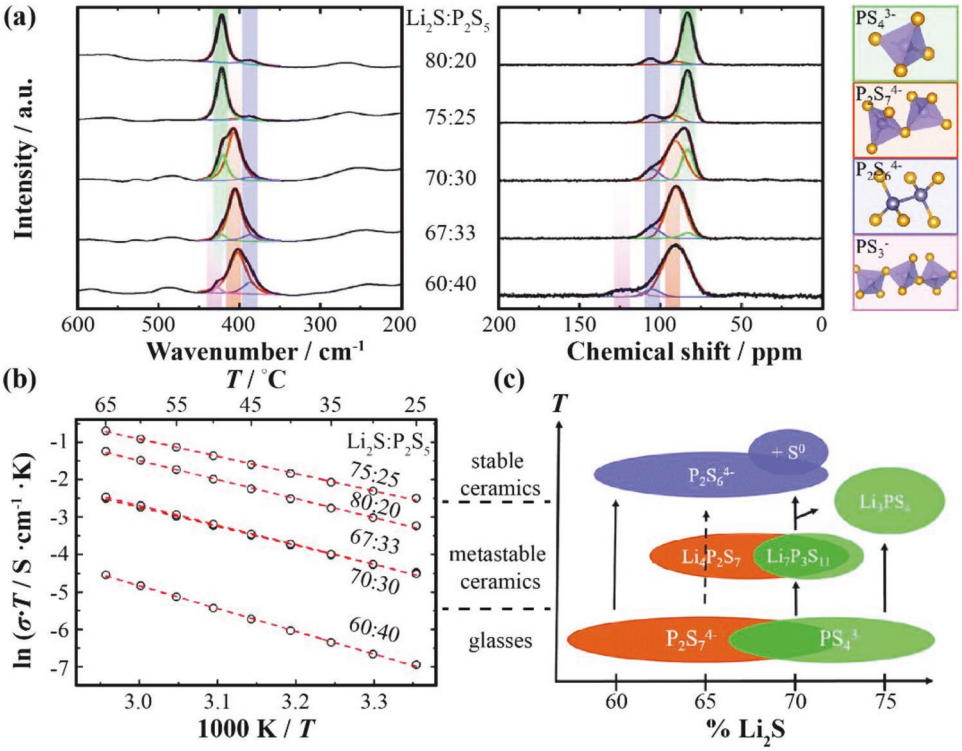

Figure 2. a) Raman and ^{31}P MAS NMR spectra of xLi$_2$S·(100 – x)P$_2$S$_5$ glasses of different stoichiometries xLi$_2$S·(100 – x)P$_2$S$_5$. b) Arrhenius plots of the resultant ionic conductivity (σT) of xLi$_2$S·(100 – x)P$_2$S$_5$ glasses. c) Local structure phase diagram derived from pair distribution function crystallization experiments. All glass compositions cleave at elevated temperatures to form sulfur and Li$_4$P$_2$S$_6$, which deteriorates Li ion conduction in SSEs. Only the 75Li$_2$S·25P$_2$S$_5$ glass consisting of PS$_4^{3-}$ withstands the reduction to P$_2$S$_6^{4-}$ at elevated temperatures and is therefore favorable for use as an SSE. a–d) Reproduced with permission.[21] Copyright 2017, Royal Society of Chemistry.

salts is an effective way to increase the Li$^+$ concentration and thus enhance the conductivity of the materials. xLi$_2$S·(100 – x)SiS$_2$ doped with Li$_3$PO$_4$, Li$_4$SiO$_4$, and Li$_4$GeO$_4$ showed significantly higher conductivity higher than 10^{-3} S cm^{-1} with a wide electrochemical window.[43,44] Addition of LiBO$_3$ and LiAlO$_3$ improve thermal stability against crystallization while maintaining the conductivity at ≈10^{-3} S cm^{-1}.[45] LiBH$_4$ is a good ionic conductor and can be used as a doping agent. For instance, 77(75Li$_2$S·25P$_2$S$_5$)·33LiBH$_4$ showed a high Li$^+$ ion conductivity of 1.6 × 10^{-3} S cm^{-1} with electrochemical stability up to 5 V versus Li$^+$/Li.[46] Adding lithium halides to the glass is another effective way to improve ionic conductivity, where the larger halide ions the higher ionic conductivity.[47–50] For instance, xLi$_2$S·(100 – x)B$_2$S$_3$ and xLi$_2$S·(100 – x)SiS$_2$ glass both have ionic conductivities of ≈10^{-4} S cm^{-1} at room temperature.[38,40] With the addition of LiI, 30Li$_2$S·26B$_2$S$_3$·33LiI glass showed a room temperature ionic conductivity of 1.7 × 10^{-3} S cm^{-1},[50] and 40Li$_2$S·28SiS$_2$·30LiI glass showed a room temperature ionic conductivity of 1.8 × 10^{-3} S cm^{-1}.[49]

2.2. Crystalline Materials

2.2.1. Li–P–S Glassy Ceramics

Several sulfide crystals have been found to crystallize in the LPS glass system: Li$_2$P$_2$S$_6$ (50Li$_2$S·50P$_2$S$_5$),[51] Li$_7$P$_3$S$_{11}$(70Li$_2$S·30P$_2$S$_5$),[52] Li$_3$PS$_4$ (75Li$_2$S·25P$_2$S$_5$),[53] Li$_7$PS$_6$ (88Li$_2$S·12P$_2$S$_5$),[54] and Li$_4$P$_2$S$_6$ (67Li$_2$S·33P$_2$S$_5$).[55] The types of crystal formed depends on the glass composition and heat-treatment conditions.[21] Crystallization of glass usually leads to reduction of ionic conduction, which is attributed to the formation of individual crystals with lower ionic conductivity. For example, the formation of Li$_4$P$_2$S$_6$ which has a conductivity of ≈10^{-7} S cm^{-1} significantly lowers the ionic conductivity of 67Li$_2$S·33P$_2$S$_5$ glass.[29] However, in the binary xLi$_2$S·(100 – x)P$_2$S$_5$ system (x ≥ 70), at high temperature superionic metastable crystalline phases precipitate in the glass materials, which leads to higher ionic conductivity than the original glass. The ionic conductivities of the glass ceramics depend on the composition because of the different phases crystallized from the starting glass (**Figure 3**a).[29]

The glassy ceramic obtained by heating 70Li$_2$S·30P$_2$S$_5$ glass at 531–633 K (258–360 °C) exhibited higher ionic conductivity of ≈10^{-3} S cm^{-1}, which is greater than pristine glass.[39] Using synchrotron powder X-ray diffraction (XRD), it was found that the crystalline phase generated from 70Li$_2$S·30P$_2$S$_5$ glass at 531–633 K was Li$_7$P$_3$S$_{11}$, which has a triclinic cell and space group P-1. The structure of Li$_7$P$_3$S$_{11}$ is an analogue to a low temperature ion conductor, α-Ag$_7$P$_3$S$_{11}$, where corner-sharing P$_2$S$_7^{4-}$ di-tetrahedra and PS$_4^{3-}$ tetrahedra are surrounded by Li ions with a different orientation of PS$_4^{3-}$ tetrahedra.[52] The fast Li$^+$ ion conduction is due to the high number of interstitial sites and large open volume between P$_2$S$_7^{4-}$ di-tetrahedra and PS$_4^{3-}$

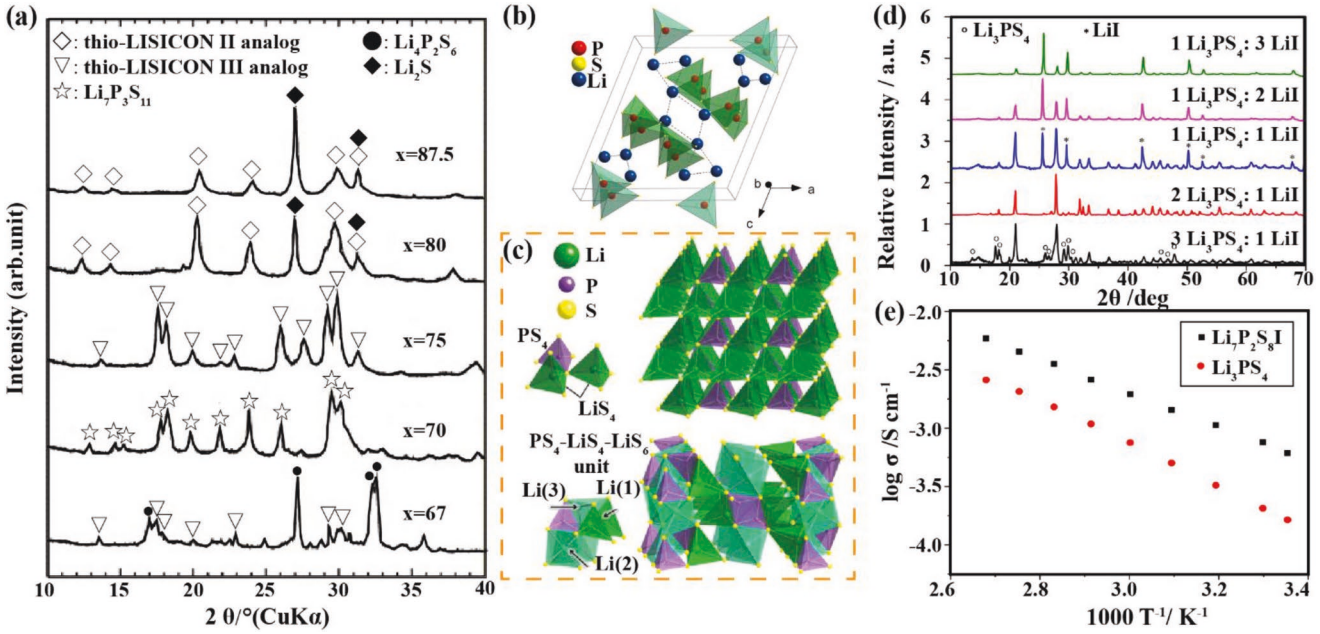

Figure 3. a) XRD patterns of the $xLi_2S{\cdot}(100-x)P_2S_5$ glass-ceramics obtained by heating the glasses up to their first crystallization temperatures: $x = 67$, 70, 75, 80, and 87.5. Reproduced with permission.[29] Copyright 2006, Elsevier. b) Crystal structure of triclinic $Li_7P_3S_{11}$ with PS_4^{3-} tetrahedra (light green) and $P_2S_7^{4-}$ di-tetrahedra (dark green) viewed along the [010] direction. Reproduced with permission.[63] Copyright 2016, Elsevier. c) Crystal structure of γ-Li_3PS_4 and β-Li_3PS_4. Reproduced with permission.[59] Copyright 2011, Elsevier. d) XRD data illustrating the formation of a new phase at the 2:1 stoichiometric composition of β-Li_3PS_4:LiI. An excess of either phase leads to the observation of the respective phase as a secondary impurity in addition to the newly formed phase. e) Arrhenius plot of the new phase, demonstrating the 400% increase in ionic conductivity and lower activation energy for the new phase in comparison with β-Li3PS4. d,e) Reproduced with permission.[61] Copyright 2015, American Chemical Society.

tetrahedra (Figure 3b). Because the PS_4^{3-} tetrahedra, the ionic conductivity of $Li_7P_3S_{11}$ crystal could reach 3.2×10^{-3} S cm^{-1} at room temperature.[32,52] Xu et al. doped $Li_7P_3S_{11}$ with molybdenum and achieved a unit formula of $Li_7P_{2.9}S_{10.85}Mo_{0.01}$. P is partially replaced by Mo and, in turn, point defects were introduced to promote the Li ion conduction. The Mo containing material showed higher ionic conductivity of 4.8×10^{-3} S cm^{-1} at room temperature with a better stability against Li metal.[18] Another doped version of $Li_7P_3S_{11}$ is $Li_7P_{2.9}Mn_{0.1}S_{10.7}I_{0.3}$, which exhibits an ionic conductivity of 5.6×10^{-3} S cm^{-1} at room temperature with good electrochemical stability. The doping of manganese and iodine widens the Li ion conduction channels and reduces the activation energy of Li ion conduction.[56]

In another study of the $70Li_2S{\cdot}30P_2S_5$ glass and glassy ceramics formed at 240 °C, the formation of glass ceramics was found to greatly enhance the room temperature ionic conductivity of the original glass from 5.4×10^{-5} to 3.2×10^{-3} S cm^{-1}. The crystalline phase in the glassy ceramics was found to be $Li_4P_2S_7$ using Raman spectroscopy. Interestingly, the crystalline material prepared using a solid-state method with the same $70Li_2S{\cdot}30P_2S_5$ composition showed different crystalline phases, $Li_4P_2S_6$, and Li_3PS_4, with much lower ionic conductivity, 2.6×10^{-8} S cm^{-1}. Thus this super-ionic metastable phase can only form via crystallization of glass, and cannot be directly prepared by solid-state reaction.[57]

With increasing ratio of Li_2S, stoichiometric Li_3PS_4 phase precipitates at the composition of $75Li_2S{\cdot}25P_2S_5$.[29] Li_3PS_4 is often considered as a thio-LISICON III phase because it is in the third composition region of the Li_4GeS_4–Li_3PS_4 binary system (explained in Section 2.2.3). Li_3PS_4 has three structural polymorphs—the low-temperature γ phase, the medium-temperature β phase and the high-temperature α phase. γ-Li_3PS_4 was first discovered in 1984, and the reported conductivity was 3×10^{-7} S cm^{-1} at 25 °C.[58] Both γ and β phase have orthorhombic structures with space group *Pmn*21. The PS_4^{3-} tetrahedra are packed along the same direction in the γ phase, and Li atoms occupy two tetrahedral positions. With more structural disorder, the PS_4^{3-} tetrahedra are packed in zig-zag directions with their apexes alternatively oriented in opposite directions in the β phase. Li atoms are situated at two tetrahedral and one octahedral site, as shown in Figure 3c. The same zig-zag packing is also seen in α phase. The Li—S bond distance is increased after transformation from γ phase to β phase, and the large Li site thermally rendered β phase a more ionic conducting state. The β phase has an abrupt increase of ionic conductivity of 3×10^{-2} S cm^{-1} at 500 K (227 °C).[59] Changes in structure could stabilize the metastable β phase at room temperature, to this end nanostructuring the material has demonstrated a high ionic conductivity of 1.6×10^{-4} S cm^{-1} at 25 °C. The nanoporous material has a high surface-to-bulk ratio, and its formation could generate several surface lattice defects. This leads to the belief that the high ionic conductivity is mainly attributed to surface conduction.[22] A similar thio-LISICON III analogue crystallizes in $78Li_2S{\cdot}22P_2S_5$ glass, and by controlling the crystallization kinetics, the conductivity at room temperature can be optimized to 8.5×10^{-4} S cm^{-1}.[60] Rangasamy et al. incorporated LiI into the β-Li_3PS_4. The new phase $Li_7P_2S_8I$ exhibited an ionic conductivity of 6.3×10^{-4} S cm^{-1} at

30 °C, which is four orders of magnitude higher than that of its starting β-Li_3PS_4 and three orders magnitude higher than LiI (Figure 3d,e).[61] With the increase of Li_2S, another superionic crystal precipitates at the composition of $80Li_2S \cdot 20P_2S_5$, $Li_{3.25}P_{0.95}S_4$, which is a phosphorous deficient thio-LISICON II analogue and has a monoclinic structure.[62] With the formation of thio-LISICON II phase, the ionic conductivity can be improved to 1.3×10^{-3} S cm^{-1} at room temperature.[29] However, thio-LISICON II phase precipitated from $80Li_2S \cdot 20P_2S_5$ glass is only stable around 250 °C. Heating the material at higher temperature results in different phases. Thio-LISICON III phase forms at 360 °C and $Li_{3.55}P_{0.89}S_4$ crystal is obtained at 550 °C.[29]

2.2.2. Li_6PS_5X (X = Cl, Br, and I) Argyrodite

The first known material with cubic argyrodite structure was Ag_8GeS_6 (space group $F\bar{4}3\ m$).[64] This material has 136 tetrahedral sites formed by chalcogen atoms in each unit cell, and these sites are partially occupied by Ag^+ and Ge^{4+}.[65] Because of the highly disordered cation arrangement, this material is characterized by its high ionic conductivity and high mobility of Ag^+, where Cu can be substituted for Ag and still maintain the argyrodite structure.[66] Inspired by the similar radii of Cu^+ and Li^+, Deiseroth et al. proposed Li^+ substitution and the replacement of one chalcogen atom by one halogen atom.[30] The lattice parameters of Li_6PS_5Cl, Li_6PS_5Br, and Li_6PS_5I are 9.85, 9.98, and 10.14 Å, respectively. The ionic conductivities of crystalline Li_6PS_5Cl, Li_6PS_5Br, and Li_6PS_5I compound are 1.9×10^{-3}, 6.8×10^{-4}, and 4.6×10^{-7} S cm^{-1}, respectively, at room temperature.[67] The difference in ionic conductivity of the three materials lies in the difference in anion disorder.[68–70] In Li_6PS_5Cl and Li_6PS_5Br, the S^{2-}/X^- anion is disordered because of the partial swapping between the normal S^{2-} and X^- sites, while in LPSI, the large I^- cannot be swapped with S^{2-} and thus leads to an ordered anion framework (**Figure 4**a).[69] There are generally three Li sites in argyrodite and the 3D pathway networks are consisted of interconnected pathway cages around anion sites. Li1 (48*h*) is the equilibrium site and has the lowest energy, Li2 (24*g*) is the interstitial site between Li1. Three Li1 and three Li2 form a low energy hexagon, and four of these hexagons are connected by interstitial Li3(16*e*) sites to form pathway cage around anion sites. 3D pathway cages further interconnect to form another set of pathways. Li_6PS_5I shows a much higher activation energy between Li1 and Li3 sites, resulting in low long-range ion conduction when compared with Li_6PS_5X with smaller Cl^- and Br^-.[69,70] Deiseroth et al. used static ^{7}Li nuclear magnetic resonance (NMR) spectroscopy to study the Li transportation dynamics. Homonuclear ^{7}Li–^{7}Li magnetic dipole–dipole interactions determine the line shapes of ^{7}Li NMR in the low temperature range and line sharpening indicates motional narrowing as the temperature increases. Among Li_6PS_5Cl, Li_6PS_5Br, and Li_6PS_5I, the narrowing effect of Li_6PS_5Br takes place at a particularly low temperature, indicating that Li_6PS_5Br has the highest Li ion mobility (Figure 4b). Further, ^{31}P NMR in Figure 4c showed that the spectrum of Li_6PS_5I was well defined, the spectrum of Li_6PS_5Cl was broad, and the spectrum of Li_6PS_5Br had both sharp and broad components. This implies that the Li_6PS_5I was fully ordered (due to the large difference in ionic radii of S^{2-} and I^-), Li_6PS_5Cl was fully disordered and Li_6PS_5Br structure was consisted of both ordered and disordered components.[30]

Minafra et al. found that replacing the P^{5+} in the Li_6PS_5Br argyrodite structure with Si^{4+} can expand the unit cell. This change is able to drive extra Li^+ ions from the equilibrium site to the transition Wyckoff 24*g* site and enhance the correlated motion of Li^+ ions. The result is a threefold increase in conductivity, 2.4×10^{-3} S cm^{-1} at room temperature, for the substituted material $Li_{6.35}P_{0.65}Si_{0.35}S_5Br$.[71] In a similar study, Kraft et al. explored aliovalent doping of Li_6PS_5I with Ge^{4+}. However, the incorporation of Ge^{4+} into Li_6PS_5Br or Li_6PS_5Cl cannot be carried out due to the large size of Ge^{4+} ions. As introduced before, Li_6PS_5I does not show any site disorder. However, with increasing occupancy of Ge^{4+} on the P^{5+} site, the onset of I^-/S^{2-} site disorder was observed at 20 at% Ge^{4+} substitution. In addition, the Li occupancy of Wyckoff 24*g* site directly correlated with the amount of Ge^{4+}, which is a similar effect as the case of $Li_{6.35}P_{0.65}Si_{0.35}S_5Br$. Increasing Li occupancy in the 24*g* site resulted in higher Coulombic repulsion and thus longer 48*h*–24*g*–48*h* distance. The intercage jump distance for Li was reduced. Another concurrent increase was found in the volume of Li(48*h*)S_3I tetrahedra and the area of Li(24*g*)S_3 triangular plane, providing possible wider Li migration pathways, Figure 4e. A maximum ionic conductivity of 5.4×10^{-3} S cm^{-1} at room temperature was found for $Li_{6.6}P_{0.4}Ge_{0.6}S_5I$, which is so far the highest value in the argyrodite family.[72]

An argyrodite-structure material, $Li_7Ge_3PS_{12}$ was discovered in the ternary Li_2S–GeS_2–P_2S_5 system. Both Li and Ge are distributed in 48*h* site, and substitution of Li by smaller Ge contracted the cubic structure, thus the lattice parameter of $Li_7Ge_3PS_{12}$ (9.80 Å) was smaller than that of Li_7PS_6 (9.99 Å). The structure of $Li_7Ge_3PS_{12}$ is featured by ordered arrangement of $(P/Ge)S_4^{3-}$ tetrahedra, in contrary to the ordered PS_4^{3-} tetrahedra in Li_7PS_6 and anion-substituted Li_6PS_5X structure (Figure 4d). The ionic conductivity of $Li_7Ge_3PS_{12}$ was determined to be 1.1×10^{-4} S cm^{-1} at 25 °C (with the presence of 2.4 wt% $Li_4P_2S_6$ impurities), which is higher than that of Li_7PS_6 (10^{-6} S cm^{-1}).[73,74]

2.2.3. Thio-LISICONs

Thio-LISICON (Lithium SuperIonic CONductor) structures were discovered in the Li_2S–GeS_2, Li_2S–GeS_2–ZnS, and Li_2S–GeS_2–Ga_2S_3 systems. In these compounds, S atoms are in hexagonal close packing, heavy metal cations are in tetrahedral sites, and Li atoms are in disordered octahedral sites.[75] Six materials have been discovered to have this structure (Li_2GeS_3, Li_4GeS_4, Li_2ZnGeS_4, $Li_{4-2x}Zn_xGeS_4$, Li_5GaS_4, and $Li_{4+x+y}(Ge_{1-y-x}Ga_x)S_4$), they all have stability up to 5 V versus Li/Li^+. Among all of these thio-LISICONs, the orthorhombic $Li_{4+x+y}(Ge_{1-y-x}Ga_x)S_4$ showed highest conductivity of 6.5×10^{-5} S cm^{-1} at room temperature. Meanwhile, the orthorhombic Li_4GeS_4 (space group *Pnma*), showed a conductivity of only 2.0×10^{-7} S cm^{-1} at room temperature.[75] Though, thin films, 100 nm thick, made with Li_4GeS_4 were found to possess a conductivity as high as 7.5×10^{-4} S cm^{-1} at room temperature.[76] The discovery of thio-LISICONs led to a wide range of new materials formed with PS_4, SnS_4, GeS_4, and SiS_4 tetrahedra building blocks.[75] One

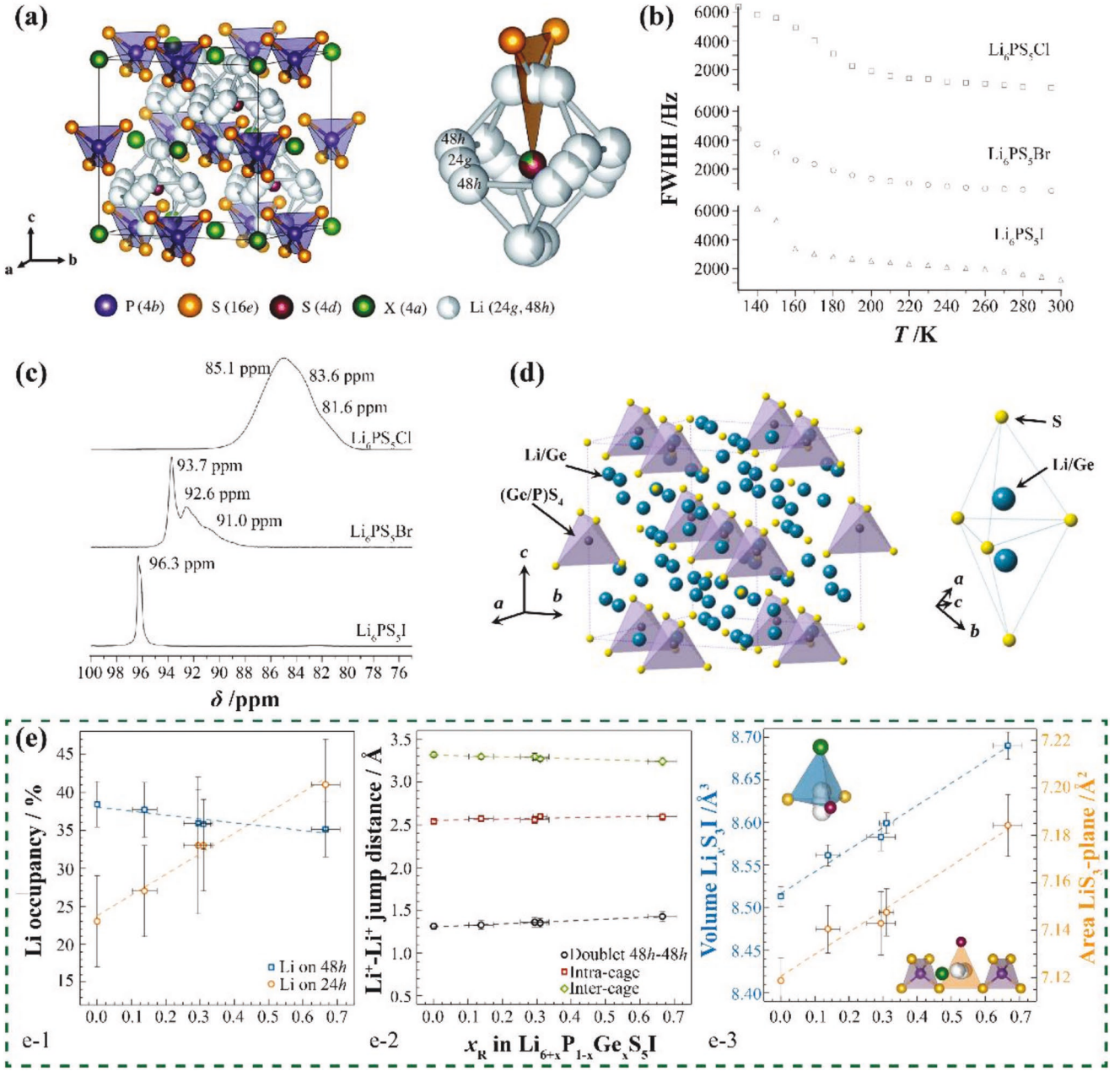

Figure 4. a) Crystal structure of Li_6PS_5Br. In the ordered structure, Br^- anions form a fcc cubic lattice with the free S^{2-} in the tetrahedral sites and PS_4^{3-} in the octahedral voids. In Li_6PS_5Br, a site disorder between S^{2-} and Br^- is known as indicated. Li^+ positions forming polyhedral cages and a jump path that bypasses a transition state coordinated by the anions. Three different jump processes are possible such as the 48*h*–24*g*–48*h* jump, as well as 48h–48h jumps in the cage and between cages. Reproduced with permission.[71] Copyright 2018, Royal Society of Chemistry. b) Static ^7Li NMR full widths at half height for Li_6PS_5Cl, Li_6PS_5Br, and Li_6PS_5I as a function of temperature. c) ^{31}P MAS-NMR spectra of Li_6PS_5Cl, Li_6PS_5Br, and Li_6PS_5I. b,c) Reproduced with permission.[30] Copyright 2008, Wiley-VCH. d) Crystal structure of the argyrodite-type $Li_7Ge_3PS_{12}$ structure as determined by Rietveld analysis. Yellow and blue spheres correspond to sulfur and to (Li/Ge) atoms, respectively. Purple tetrahedra represent the (Ge/P)S_4 units. And the coordination environment of the (Li/Ge)S_4 tetrahedra. Lithium atoms occupy the tetrahedral 48*h* site with an occupation parameter of ≈0.3. The tetrahedra form bi-pyramidal structures with face sharing connections. Reproduced with permission.[73] Copyright 2017, Elsevier. e) Changes to the Li substructure in $Li_{6+x}P_{1-x}Ge_xS_5I$, as obtained from the neutron diffraction data as a function of the refined Ge content x_R. With increasing Ge^{4+} occupancy, additional Li^+ is incorporated into the structure to maintain charge neutrality. e-1) Percentage of sites occupied by Li^+ with the additional Li^+ being placed on the Wyckoff 24*g* position. e-2) The increasing Li^+ content produces an increase in the distance between the 48*h*–24*g*–48*h* positions (doublet distance), which can be attributed to increased Coulombic repulsion, and a decreasing jump distance between the Li^+ cages (intercage jump). e-3) With increasing unit cell size and size of the adjacent (P/Ge)S_4 tetrahedra, the Li(48h)S_3I polyhedra and Li(24*g*)S_3 triangle areas are increasing, corresponding to wider diffusion pathways for Li^+. e) Reproduced with permission.[72] Copyright 2018, American Chemical Society.

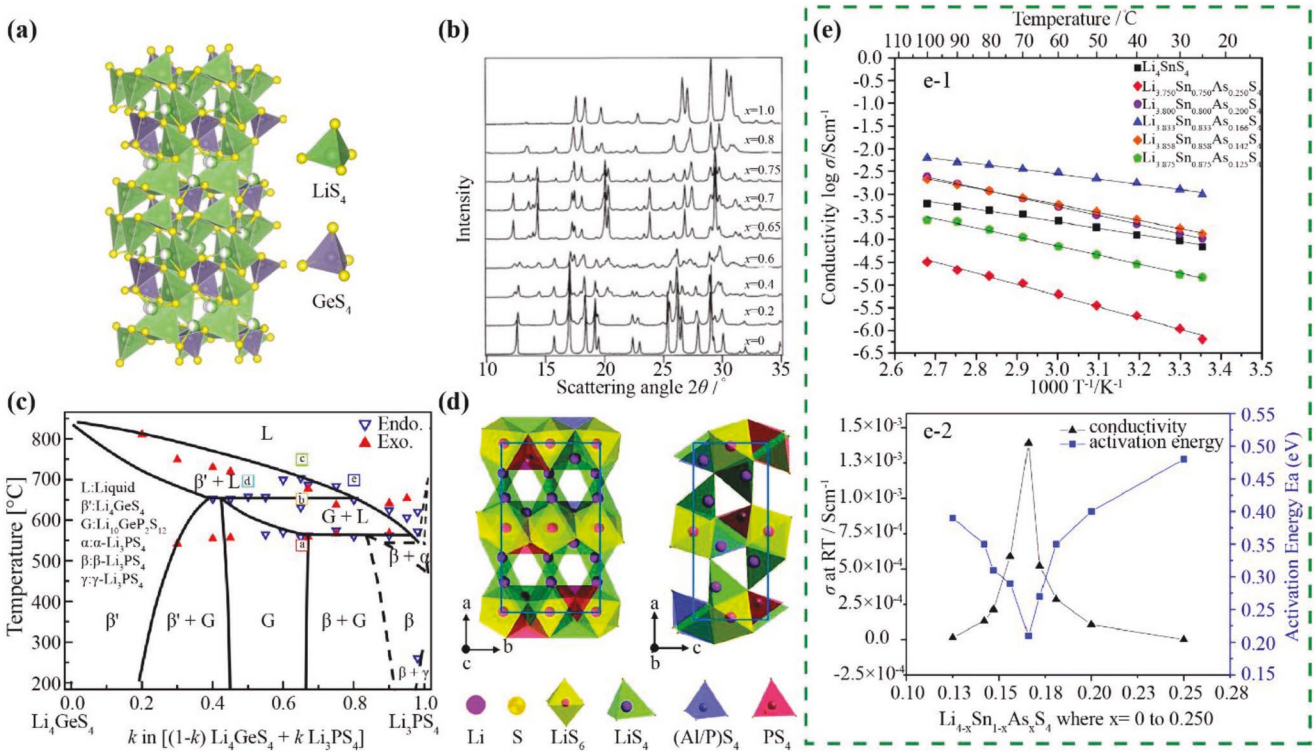

Figure 5. a) The structure of the thio-LISICON. The structure drawn in the Figure is based on the parent structure of Li_4GeS_4. The 3D framework structure is composed of GeS_4 tetrahedra. b) XRD patterns of $Li_{4-x}Ge_{1-x}P_xS_4$. a,b) Reproduced with permission.[24] Copyright 2001, The Electrochemical Society. c) Phase diagram for the Li_4GeS_4–Li_3PS_4 system. Empty and solid triangles, respectively, indicate endo- and exothermic reaction temperatures determined from DTA data. Phase boundaries indicated by dotted lines are assumed from experimental results but were not as evident as those shown by solid lines. Reproduced with permission.[79] Copyright 2015, The American Ceramic Society, published by Wiley. d) Crystal structure of $Li_{11}AlP_2S_{12}$ with a thio-LISICON analogous structure. Reproduced with permission.[80] Copyright 2016, Royal Society of Chemistry. e-1) Arrhenius plot of ionic conductivity of Li_4SnS_4 and As-doped Li_4SnS_4, i.e., $Li_{4-x}Sn_{1-x}As_xS_4$ (where x ranges from 0.125 to 0.25) with various molar ratios of As:Sn. e-2) Room-temperature ionic conductivity (left y-axis) and activation energies (right y-axis) as functions of composition. e) Reproduced with permission.[78] Copyright 2015, Royal Society of Chemistry.

of the later thio-LiSICON discovered was the Li_4SnS_4 (space group *Pnma*), which is isostructural to Li_4GeS_4 and exhibits an ionic conductivity of 7.0×10^{-5} S cm^{-1} at room temperature.[77] Further, aliovalent doping with As ($Li_{3.833}Sn_{0.833}As_{0.166}S_4$) can dramatically increase its conductivity to 1.4×10^{-3} S cm^{-1}.[78]

The crystalline thio-LISICON $Li_{4-x}Ge_{1-x}P_xS_{4-x}$ family (space group $P2_1/m$) was discovered based on aliovalent substitution of Ge^{4+} with P^{5+} in Li_4GeS_4 in the Li_2S–GeS–P_2S_5 system. Crystal structure is shown in **Figure 5**a based on the parent structure Li_4GeS_4. It can be considered as a solid solution of Li_4GeS_4 and γ-Li_3PS_4, as shown in the XRD pattern in Figure 5b. Based on structural properties derived from the XRD pattern, three regions were identified of the $(1 - x)Li_4GeS_4$–xLi_3PS_4 solid solution: orthorhombic thio-LISICON I region ($x \leq 0.6$), monoclinic thio-LISICON II region ($0.6 < x < 0.8$) and monoclinic thio-LISICON III region ($x \geq 0.8$).[16] The highest room temperature ionic conductivity of 2.2×10^{-3} S cm^{-1} was found for $x = 0.75$ ($Li_{3.25}Ge_{0.25}P_{0.75}S_{3.25}$) in the $Li_{4-x}Ge_{1-x}P_xS_{4-x}$ family.[16] Later on, Hori et al. constructed a more detailed phase diagram of the $(1 - x)Li_4GeS_4$–xLi_3PS_4 binary system using room-temperature and high-temperature X-ray diffraction (XRD) and differential thermal analysis (DTA) (Figure 5c).[79] All of the diffraction peaks can be attributed to Li_4GeS_4, $Li_{10}GeP_2S_{12}$ (LGPS), and Li_3PS_4. Single-phase region of Li_4GeS_4, LGPS, and β-Li_3PS_4 lied within $0.1 \leq x \leq 0.2$, $0.5 \leq x \leq 0.67$, and $0.9 \leq x \leq 0.98$, respectively. The solid solution range might expand at elevated temperature, for instance, the mixture of Li_4GeS_4 and LGPS changed to single phase Li_4GeS_4 at 650 °C.[79]

Similar materials can also be made based on modification of Li_4SiS_4. The ionic conductivity of thio-LISICONs is strongly dependent on the size and polarizability of constituent ions, which is why the germanium system shows better conductivities than the silicon series. However, to avoid the use of the rare and expensive germanium, Ge^{4+} can be substitute with Al^{3+}, which could eliminate nonbridging sulfur and facilitate ionic conductivity. Furthermore, $Li_{11}AlP_2S_{12}$ (can also be written as $Li_{(4-1/3)}Al_{1/3}P_{2/3}S_4$) a thio-LISICON analogue has been studied, and its crystal structure is shown in Figure 5d.[80,81] The predicted ionic conductivity of $Li_{11}AlP_2S_{12}$ is 3.3×10^{-2} S cm^{-1};[31] however, the experimentally achieved ionic conductivity is only 8.02×10^{-4} S cm^{-1} at room temperature.[80] Another exceptional material derived from the thio-LISION family is phosphorus-free As-substituted Li_4SnS_4, developed by Sahu et al.[78] Due to the hypersensitivity to air and moisture of the P-containing sulfides, Sn and As were used as the center elements to be compounded with sulfur. The resulting Li_4SnS_4 material was

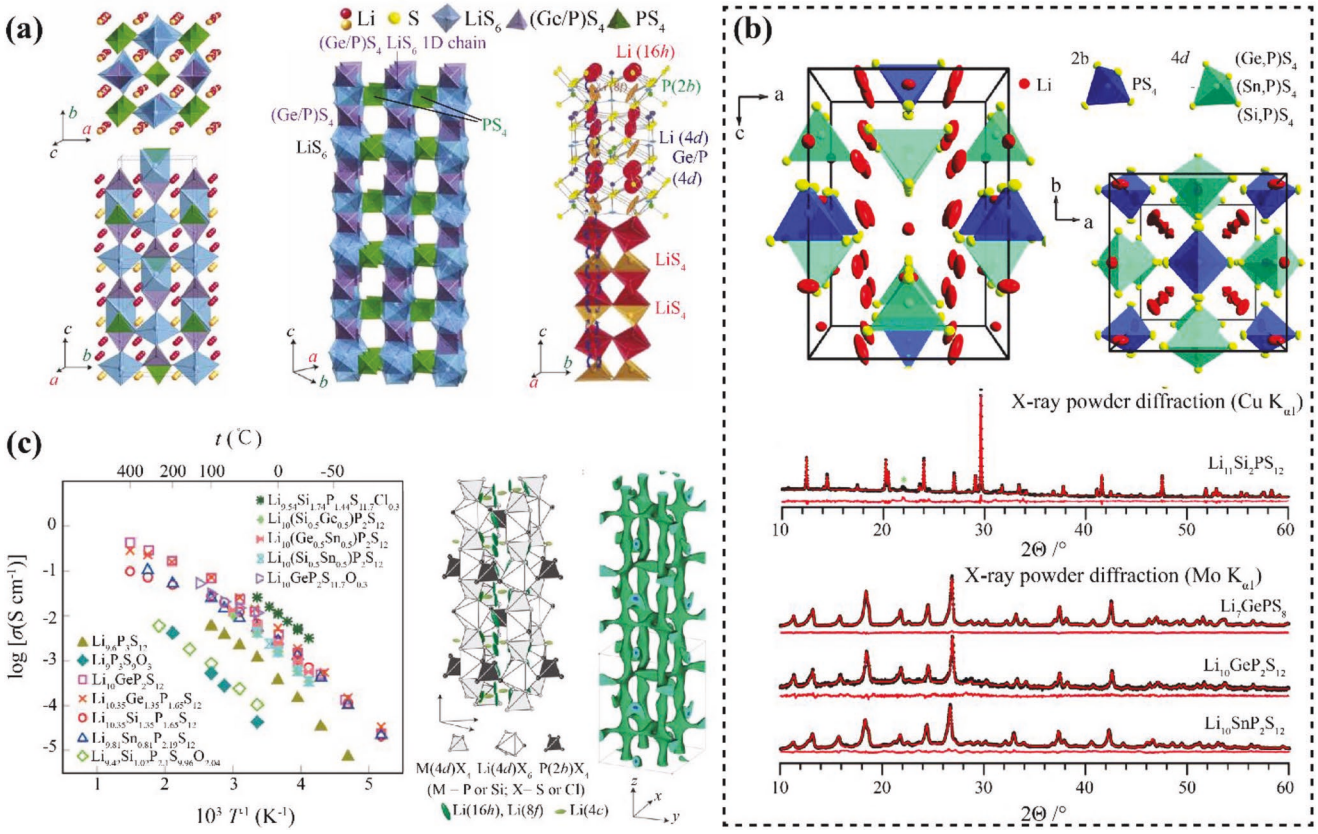

Figure 6. a) Crystal structure of LGPS. a-1) the framework structure and lithium ions that participate in ionic conduction. a-2) Framework structure of LGPS. 1D chains formed by LiS_6 octahedra and $(Ge_{0.5}P_{0.5})S_4$ tetrahedra, which are connected by a common edge. These chains are connected by a common corner with PS_4 tetrahedra. a-3) Conduction pathways of Li ions. Zigzag conduction pathways along the c axis are indicated. Li ions in the LiS_4 tetrahedra (16*h* site) and LiS_4 tetrahedra (8*f* site) participate in ionic conduction. Thermal ellipsoids are drawn with a 30% probability. The anisotropic character of the thermal vibration of Li ions in three tetrahedral sites gives rise to 1D conduction pathways. a) Reproduced with permission.[16] Copyright 2011, Springer Nature Publishing AG. b) Crystal structure of tetragonal LGPS as obtained from single crystal X-ray diffraction and X-ray powder diffraction and Rietveld refinement of $Li_{11}Si_2PS_{12}$ and LSnPS in comparison to previously reported LGPS and Li_7GePS_8. The side phase is marked by a green asterisk. Reproduced under the terms of the CC-BY Creative Commons Attribution 3.0 Unported license (https://creativecommons.org/licenses/by/3.0/).[88] Copyright 2014, Royal Society of Chemistry. c) Crystal structure of $Li_{9.54}Si_{1.74}P_{1.44}S_{11.7}Cl_{0.3}$. Reproduced with permission.[10] Copyright 2016, Springer Nature Publishing AG.

very stable in air with an ionic conductivity of 7.1×10^{-5} S cm^{-1} at 25 °C. The substitution by As creates interstitials and/or vacancies that improve ionic conductivity compared to the pristine material. The highest conductivity achieved with this substitution was for the $Li_{3.833}Sn_{0.833}As_{0.166}S_4$ showing an ionic conductivity of 1.39×10^{-3} S cm^{-1} (Figure 5e).[78]

2.2.4. $Li_{11-x}M_{2-x}P_{1+x}S_{12}$ (M = Ge, Sn, and Si) Structures

Tetragonal $Li_{10}GeP_2S_{12}$ (LGPS) with a space group $P4_2/nmc$ was discovered by Kamaya et al. in 2011. Derived from the $(1 - x)Li_4GeS_4$–xLi_3PS_4 binary system, LGPS can be found at the solid solution range of $0.5 \leq x \leq 0.67$. The structure of the thio-LISICONs $Li_{4-x}Ge_{1-x}P_xS_{4-x}$ (space group $P2_1/m$) can be used to understand the structure of LGPS. The two phases differ in the arrangement of MS_4 (M = Ge, P) tetrahedra. In monoclinic thio-LISICONs, MS_4 runs along the *b* axis, while in $Li_{10}GeP_2S_{12}$, MS_4 runs along the *a* and *b* axes, resulting in shorter M–M distances.[24,82] The edge-sharing $(Ge_{0.5}P_{0.5})S_4$ tetrahedra and LiS_6 octahedra in LGPS form 1D chains. The chains are interconnected by LiS_4 tetrahedra which form a 1D Li conduction pathway along the *c* axis. Tetrahedrally coordinated Li sites 16*h* and 8*f* sites give rise to Li conduction channels, while octahedrally coordinated Li site 4*d* in the framework chains are inactive for conduction (**Figure 6**a).[16] Adams et al. identified a fourth low energy Li site 4*c* using molecular dynamics calculations, and suggested the involvement of 4*c* Li in the conduction perpendicular to the 1D chains.[82] Kuhn et al. used single crystal diffraction to reveal a fourth Li site, which connects the 1D diffusion channels formed by the two active Li sites, and proposed active diffusion at this site.[83] Using first principle calculations, Mo et al. predicted that LGPS is a 3D conductor rather than a 1D conductor, because of the significant Li hopping in the *ab* plane and empty space between $(Ge_{0.5}P_{0.5})S_4$ tetrahedra and LiS_4 tetrahedra. However, the Li diffusion along *ab* plane is much slower and the predicted ionic conductivity in the *ab* plane at room temperature is 9.0×10^{-4} S cm^{-1}.[84] With an ionic conductivity of 1.2×10^{-2} S cm^{-1} at room temperature,

LGPS is the first solid electrolyte to demonstrate comparable or even higher ionic conductivity than liquid electrolytes. In addition to its superior conductivity at room temperature, LGPS shows very high conductivity at lower temperatures (1.0×10^{-3} S cm^{-1} at -30 °C and 4.0×10^{-4} S cm^{-1} at -45 °C).[16] The high ionic conductivity could be attributed to the nearly isotropic Li hopping in the bulk lattice with $E_a \approx 0.22$ eV.[85]

However, a major drawback for LGPS material is the high cost due to the usage of Ge metal. This led to studies on partial or complete substitution of Ge in LGPS material. Ong et al. showed that iso-valent cation substitutions of Ge^{4+} minimally impact Li ion diffusivity in the LGPS tetragonal structure.[31] $Li_{10}SnP_2S_{12}$ (LSnPS), which is isostructural to LGPS with a slightly different Li ion disorder, is an affordable alternative. LSnPS exhibits a slightly higher grain boundary resistance than LGPS, resulting in a lower total ionic conductivity of 4×10^{-3} S cm^{-1} at room temperature. Fortunately, this is still comparable to liquid electrolytes.[17] By replacing 30% Sn with Si and forming $Li_{10}Sn_{0.7}Si_{0.3}P_2S_{12}$, Bron et al. greatly reduced grain boundary resistance and improved the ionic conductivity to 8×10^{-3} S cm^{-1} at room temperature.[86] Another cost-effective option is $Li_{10}SiP_2S_{12}$ (LSiPS), which also crystallizes in LGPS structure with smaller lattice parameter than LGPS (a = 8.65 Å and c = 12.51 Å for LSiPS and a = 8.71 Å and c = 12.63 Å for LGPS). It was suggested by Ong et al. that LSiPS has higher ionic conductivity 2.3×10^{-2} S cm^{-1} than LGPS.[31] However, LSiPS demonstrates a lower ionic conductivity of 2.3×10^{-3} S cm^{-1} at room temperature. This is likely due to the formation of orthorhombic by-phase which contributes additional Maxwell-Wagner type impedance.[87] Kuhn et al. used ^{7}Li NMR to illustrate that the Li ion diffusivity of LSnPS is slightly lower than that of LGPS, while that of LSiPS is even higher than LGPS. These latter results are in good agreement with Ong's reports (Figure 6b).[87,88] In order to stabilize the tetragonal modification, the 4*d* site has to be occupied by Si to a higher extent as compared to Ge or Sn, which is why the Si analogue is obtained for the stoichiometry $Li_{11}Si_2PS_{12}$ rather than $Li_{10}SiP_2S_{12}$.[88]

In the $Li_{11-x}M_{2-x}P_{1+x}S_{12}$ family, $Li_{9.54}Si_{1.74}P_{1.44}S_{11.7}Cl_{0.3}$ has an exceptional Li ion conductivity of 2.5×10^{-2} S cm^{-1} at room temperature. This is the highest reported Li ionic conductivity so far, featured in the Arrhenius plots in Figure 6c.[10] In this LGPS-type structure, the 1D framework consists of edge-sharing MX_4 (M = P or Si; X = S or Cl) tetrahedra connected by PX_4 (X = S or Cl) tetrahedra (Figure 6c). In which, the active Li is located on the interstitial 16*h*, 8*f*, and 4*c* sites, and the superior ionic conductivity is attributed to the 3D conduction in the structure.[10]

2.3. Composite and Hybrid Materials

Besides ionic conductivity, other factors that influence the SSE cells are: chemical compatibility with other components, interfacial contact and resistance, and processability. Based on these requirements, it would be extremely difficult to find a single SSE that meets all the requirements. Because of that, sulfide SSEs have been combined with other electrolyte materials to enhance the properties of parent electrolytes.

2.3.1. Composite of Sulfide and Organic Polymers

Composite and hybrid electrolytes containing inorganic and organic electrolytes are developed to combine the advantages of high ionic conductivity of the inorganic part and great mechanical properties of the organic component. While composite electrolytes were formed by physically mixing inorganic with organic solid electrolytes, hybrid electrolytes usually contain gel or liquid electrolyte which forms chemical bonds with the inorganic compounds. The gel or liquid mixtures lead to a higher ionic conductivity reported for hybrid electrolytes.[89–91] The main challenge of combining inorganic and organic materials is to maintain the high ionic conductivity of the inorganic part when an ion-insulating polymer is added to the mixture.[92]

Hayashi et al. combined $70Li_2S \cdot 30P_2S_5$ glass with several types of oligomers, diethylene glycol, poly(ethylene glycol)s, polyethylene glycol dimethyl ether, and 1,4-butanediol. The addition of small amount of polymer enhanced the ionic conductivity. Specifically, the hybrid with 1,4-butanediol exhibits a higher ionic conductivity, 9.7×10^{-5} S cm^{-1} at room temperature, than the pure glass, 6.3×10^{-5} S cm^{-1} at room temperature. They confirmed the formation of P—O—C bonds between the glass and —OH terminated oligomers, which is the key to achieving a higher conductivity because of the insulating nature of oligomers. It is also of note that the addition of small amounts of polymers (3 wt%) into the glass enhanced ion conduction by lowering the glass transition temperature (T_g).[90] Hayashi et al. also investigated the effect of proportion and chain length on the ionic conductivity of hybrid electrolyte, and found that using ethylene glycol (alkanediol with shorter chain length) led to a high conductivity of 1.1×10^{-4} S cm^{-1} at room temperature.[91] Villaluenga et al. prepared hybrid electrolyte with $75Li_2S \cdot 25P_2S_5$, —OH-terminated perfluoropolyether (PFPE) and lithium bis (trifluoromethane) sulfonimide (LiTFSI). They found that the resulting hybrid containing 23 wt% polymer exhibited ionic conductivity of 10^{-4} S cm^{-1} at 30 °C. This hybrid electrolyte improved adhesion and compliance, while maintaining the ionic conductivity of glass.[93]

Cold pressed solid electrolyte pellets have considerable porosity (25–28%), and reports have shown that porosity positively affects bulk ionic conductivity.[94] Filling the empty voids of solid electrolyte particles with organic polymers can provide mechanical flexibility and robustness to the composite electrolyte. Whiteley et al. employed various polyimines (20 wt%) to pair them with $77.5Li_2S \cdot 22.5P_2S_5$ glass ceramic. His group synthesized what they called a malleable solid electrolyte-in-polymer matrix (SEPM) membrane (**Figure 7**a). After hot pressing the composite relative density was 97% compared to 75% for the pure $77.5Li_2S \cdot 22.5P_2S_5$ pellet, which means the voids of the glass-ceramic were properly filled. The bulk ion conductivity of the composite was 1×10^{-4} S cm^{-1} at 25 °C, showing a clear inverse proportionality between conductivity and membrane thickness. They showed that a membrane 63.7 µm thick made from methyl-imine composite had a higher conductivity of 9.2×10^{-5} S cm^{-1} at 25 °C.[95] Nam et al. developed a thin composite SSE film based on mechanically compliant poly-(paraphenylene terephthalamide) (PPTA) nonwoven (NW) scaffold. Sulfide SSEs such as Li_3PS_4 and LGPS were

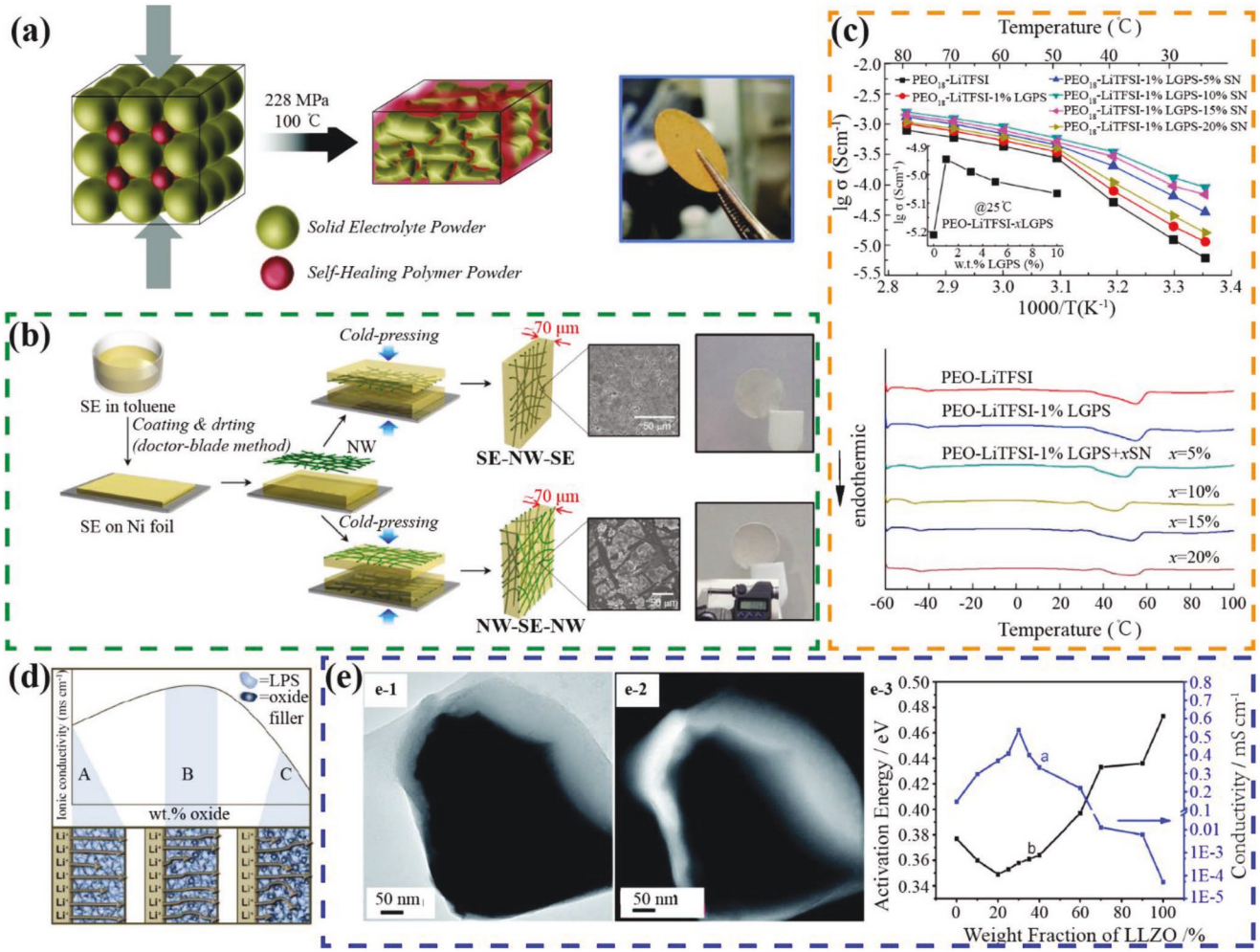

Figure 7. a) Schematic for forming the solid electrolyte in polymer matrix membrane. Through the application of heat and pressure, malleability is achieved in the polyimine forming a continuous network without sacrificing solid electrolyte particle contact. Reproduced with permission.[95] Copyright 2015, Wiley-VCH. b) Schematic diagram showing the fabrication of bendable sulfide NW-SSE films with two different structures (SSE-NW-SSE and NW-SSE-NW). SEM and photoimages are also provided. Reproduced with permission.[96] Copyright 2015, American Chemical Society. c) Arrhenius plots for the ionic conductivities of the membranes with various LGPS and SN contents and DSC curves of various samples. Reproduced with permission.[20] Copyright 2016, Elsevier. d) Model for the oxide filler's effect on the parent LPS electrolyte. "A" represents the addition of no oxide filler, "B" represents the space-charge effect, and "C" shows the blocking effect of the oxide filler. Reproduced with permission.[98] Copyright 2015, Elsevier. e-1) TEM image of the LLZO–L_3PS_4 (nanocrystalline) composite electrolyte clearly illustrates the core–shell structure; e-2) an EELS map shows a higher Li concentration across the LLZO–L_3PS_4 interface (the bright part has a high concentration of Li); e-3) Plot of ionic conductivity (right *y*-axis) and activation energy (left *y*-axis) as a function of the weight fractions of LLZO in the composite. e) Reproduced with permission.[99] Copyright 2014, Royal Society of Chemistry.

employed to make a sandwich structure film SSE–NW–SSE and NW–SSE–NW. Both of which were freestanding with a thickness of 70 µm (Figure 7b). Despite marginal decrease in conductivity values, the conductivity of Li_3PS_4–NW–Li_3PS_4 (2.0×10^{-4} S cm^{-1}) and NW–Li_3PS_4–NW (1.6×10^{-4} S cm^{-1}) were higher than the SSE film (7.3×10^{-4} S cm^{-1}), indicating that good ionic conducting pathways were formed between the SSE and polymer scaffold. The bendability of the composite films is attributed to the high flexibility of the polymer which ensures the mechanical integrity of the composite and prevents breakage due to structural defects or pores.[96] Zhao et al. incorporated LGPS at 1 wt% into the polyethylene oxide (PEO) matrix. The composite membrane exhibited an ionic conductivity of 1.2×10^{-3} S cm^{-1} at 80 °C and 1.2×10^{-5} S cm^{-1} at 25 °C, while the conductivity of PEO-only membrane is 8.0×10^{-4} S cm^{-1} at 80 °C and 6.2×10^{-6} S cm^{-1} at 25 °C. In this case, LGPS acted as a filler. This lowered T_g and the melting temperature (T_m) of PEO, and increased Li ion conduction. As indicated by the Arrhenius plots, Li transport at higher temperature (>50 °C) is much faster than that at lower temperature (<50 °C) (Figure 7c).[97] A similar study was carried out by the same group using a PEO/LGPS composite electrolyte, and succinonitrile (SN), a solid plasticizer was added to further increase the amorphous phase in the composite. The addition of SN further dropped T_g and T_m, as shown in Figure 7c. This addition promoted Li ion transfer by reducing the interaction of Li ions and PEO chains as well. It was found that a composite electrolyte made with 1 wt% LGPS and 10 wt% SN had the highest conductivities, 1.6×10^{-3} S cm^{-1} at 80 °C and 9.1×10^{-5} S cm^{-1} at 25 °C.[20]

2.3.2. Sulfide and Inorganic Metal Oxide Composites

Besides combining with organic polymers, sulfide SSEs can also be mixed with inorganic metal oxides to improve their performance. Hood et al. examined the "filler effect" of three metal oxides, $Li_6ZnNb_4O_{14}$ (LZNO), Al_2O_3 and SiO_2, in β-Li_3PS_4 electrolyte (ionic conductivity of β-Li_3PS_4 was 1.6×10^{-4} S cm^{-1} in this study). Among these oxides, LZNO was an ionic conductor (3×10^{-5} S cm^{-1} at 21.5 °C), while the other two were not. The addition of small amounts of oxides enhanced the ionic conductivity of the composite. For instance, 10 wt% LZNO, 2 wt% Al_2O_3, and 2 wt% SiO_2 increased the ionic conductivity of β-Li_3PS_4 to 2.4×10^{-4}, 2.3×10^{-4}, and 1.8×10^{-4} S cm^{-1}, respectively. Conversely, conductivity values decreased after adding more than 30 wt% LZNO, 8 wt% Al_2O_3, and 5 wt% SiO_2. It was also demonstrated that the addition of low amount of oxides did not jeopardize the electrochemical stability of the electrolyte. Hood et al. established a model to explain the ion conduction in a solid sulfide-oxide composite. Li ion conduction is influenced by two contradicting mechanisms in heterogeneous composites. At lower concentration of oxides, the ionic conductivity is increased by the change of charge carrier distribution in the composite caused by the surface acidity of oxides. With a high concentration of oxides in the system, the oxides particles block the motion of Li ions (Figure 7d).[98] Similarly, Rangasamy et al. studied the composite of $Li_7La_3Zr_2O_{12}$ (LLZO, conductivity 4×10^{-4} S cm^{-1} at room temperature) and β-Li_3PS_4. Interestingly, a core–shell structure was obtained by mechanical mixing of these two materials, where β-Li_3PS_4 formed a soft shell as a result of the soft nature of sulfides and LLZO was the core (Figure 7e). The maximum conductivity of the composite, 70 wt% β-Li_3PS_4 + 30 wt%LLZO, reached 5.36×10^{-4} S cm^{-1} at room temperature, which is higher than either individual component (Figure 7e). The conductivity started to decrease at over 60 wt% of LLZO. The authors attributed the improved conductivity to the formation of space-charge layer at the interface between the LLZO and the β-Li_3PS_4. They believed the space-charge layer led to a redistribution of ionic and electronic point defects, enhancing the ionic conductivity as a result.[99]

3. Preparation Approaches of Sulfides Solid-State Electrolyte

Because of the high reactivity in humid air, sulfides are prepared under inert atmosphere. The most common preparation methods to make sulfide SSEs are melt-quenching and ball-milling, which involve high-temperature treatment or overlong mechanical mixing. Wet chemical processes have been developed and show obvious advantages for scaling up over conventional methods.

3.1. Melt Quenching

Melt quenching is a widely used method to produce glass sulfide materials. The starting materials such as Li_2S and P_2S_5 are sealed in a quartz tube and melted at temperatures between 900 and 1100 °C.The materials are then rapidly quenched in ice water or a twin roller quenching machine.[38,100] The melting reaction has to be carried out in sealed tubes because of the high vapor pressure of P_2S_5.[101] A common way to improve Li ion conductivity is to increase the concentration of Li ions, which has been found to be effective in all the sulfide systems. Another approach is to mix oxide powder with sulfide glass, which is known as the "mixed anion effect." It has been found that in some systems this mixing can improve both conductivity and stability of the final mixture.[44,102]

3.2. Ball-Milling and Solid-State Reactions

While melt-quenching is a harsh and troublesome process, high-energy ball-milling has been the most popular approach to produce well-mixed fine powders. Ball-milling works on the principle of impact and attrition, where materials can be effectively pulverized, amorphized, and mixed. In contrast to melt-quenching, the ball-milling process is conducted at room temperature. Without the formation of local melt, amorphization process is through solid-state inter-diffusion reaction where the kinetics are governed by the point and lattice defects brought by plastic deformation.[28,103] As shown in **Figure 8**a, Yamamoto et al. reported that in the $Li_2S \cdot P_2S_5 \cdot GeS_2$ ternary system, the region of amorphous sample formed by ball-milling is much wider than conventional melt-quenching.[104] Thus ball-milling provides more possibilities to prepare new amorphous glassy materials. Most sulfide glass conductors can be produced by ball-milling, and crystalline phases can be achieved by mixing and consecutive annealing step.[16,32,59,71,105] Ball-milling has also been employed to mix sulfide SSEs with organic polymers, which produces a mixture of well-dispersed polymers without breaking their organic chains.[90,93]

Speed and time are two important factors affecting the phases and crystallinities of the resulting materials. In the case of ball-milling Li_6PS_5Cl, Yu et al. found that lower milling speed of 110 rpm was not energetic enough to amorphize the compound. When the milling speed was increased to 550 rpm, the peak intensity of starting material Li_2S and LiCl gradually increased with milling time in XRD data (Figure 8b). Crystalline Li_6PS_5Cl precipitated after 4 h of milling, but the ionic conductivity did not improve until at least 8 h of milling (Figure 8c).[106]

3.3. Wet Chemical Reactions

While solid electrolytes prepared from melt-quenching and ball-milling exhibit excellent ionic conductivity, these conventional methods are time-intensive, energy-consuming, and difficult to scale up. Preparation of solid electrolytes in liquids is an effective method to shorten reaction time and produce homogeneous materials. Wet chemical reaction is a simple method to form an intimate electrode–electrolyte interface.[107,108] However, due to the high reactivity of sulfide SSE precursors, the wet-chemical reactions are restricted to nonpolar solvents and less polar aprotic solvents.[109,110]

As introduced before, Li_3PS_4 exists as γ phase at room temperature and transitions to ionically conductive β phase at ≈200 °C. β-Li_3PS_4 is metastable and conventionally prepared through solid-state reaction of Li_2S and P_2S_5 at high temperatures.

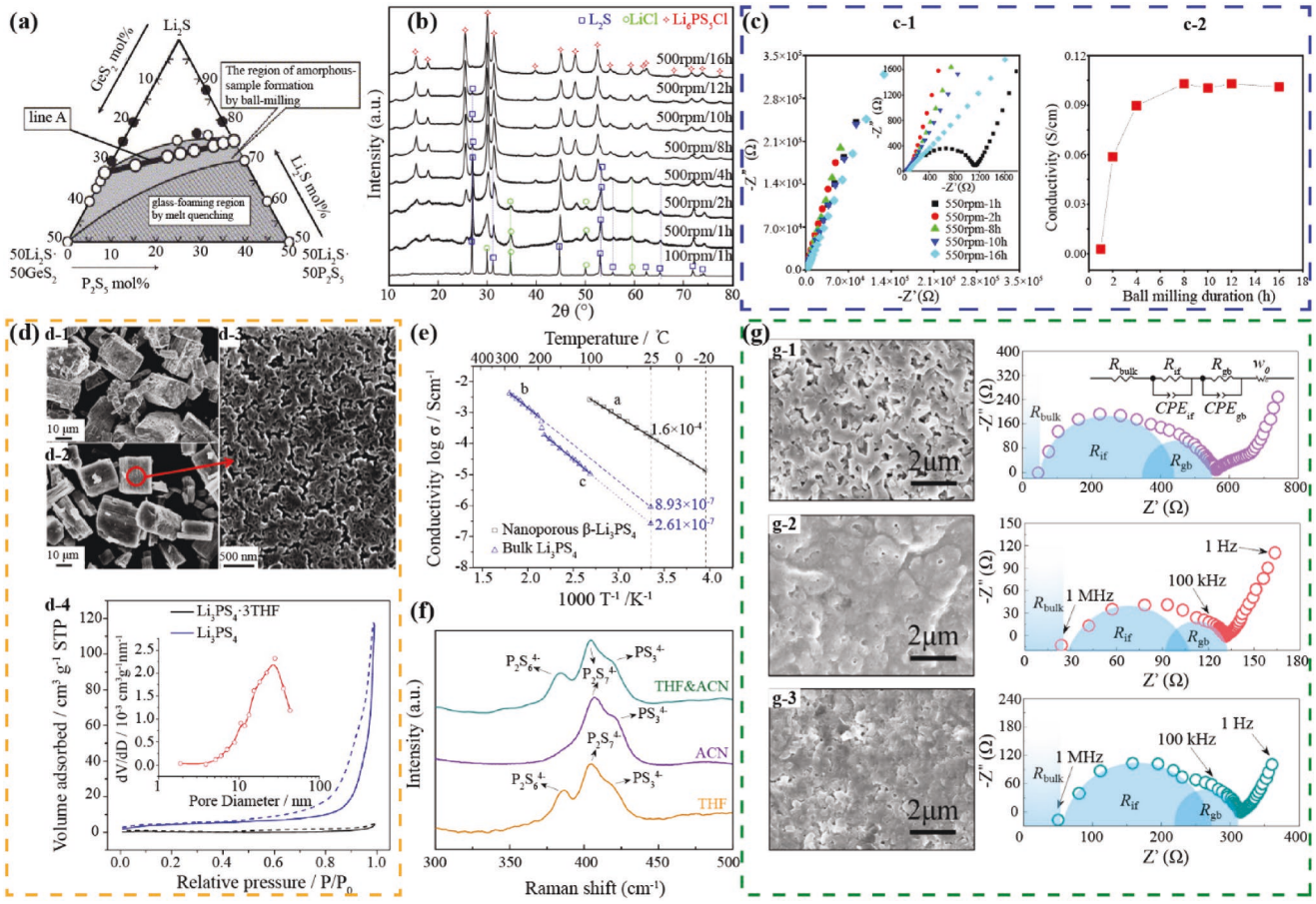

Figure 8. a) The composition range in which amorphous samples were obtained by the high-energy ball-milling process in the system $Li_2S{\cdot}GeS_2{\cdot}P_2S_5$: hollow circles indicate amorphous samples and solid circles indicate partially crystalline samples. The hatched area is the glass-forming region by conventional melt-quenching methods. Reproduced with permission.[104] Copyright 2004, Elsevier. b) XRD patterns of the mixture of Li_2S, P_2S_5, and LiCl powders ball-milled with different milling times. c-1) Complex impedance plots for the sample ball-milled for different durations. c-2) The conductivity of the ball-milled samples versus the milling time. b,c) Reproduced with permission.[106] Copyright 2016, Elsevier. d) Characterization of the porous β-Li_3PS_4 structure. d-1) Morphology of as-synthesized $Li_3PS_4{\cdot}3THF$ particles. d-2) Morphology of nanoporous β-Li_3PS_4 particles. d-3) Surface of the nanoporous β-Li_3PS_4. d-4) N_2 adsorption/desorption isotherms at 77 K. The inset shows the pore size distribution of β-Li_3PS_4 calculated using the adsorption branch of the isotherm. d) Reproduced with permission.[22] Copyright 2013, American Chemical Society. e) Arrhenius plots for nanoporous β-Li_3PS_4 (line a), bulk β-Li_3PS_4 (line b), and bulk γ-β-Li_3PS_4 (line c). Reproduced with permission.[22] Copyright 2013, American Chemical Society. Data for line (a) are from ref. [22]. Data for line (b) and line (c) were originally presented in ref. [58]. f) Raman spectra of $Li_7P_3S_{11}$ synthesized by THF, ACN, and THF&ACN. Reproduced with permission.[32] Copyright 2016, Elsevier. g) SEM images of $Li_7P_3S_{11}$ pellets prepared by THF (g-1), ACN (g-2), and THF&ACN (g-3) and the matching impedance figures at 298 K. The equivalent circuit is inserted in the impedance spectrum. g) Reproduced with permission.[32] Copyright 2016, Elsevier.

Teragawa et al. demonstrated that P_2S_5 can be dissolved in N-methylformamide (NMF), and Li_2S can be dissolved in the NMF solution of P_2S_5. Through a liquid reaction of Li_2S and P_2S_5 in NMF and n-hexane followed by a heat-treatment at 180 °C, Teragawa et al. obtained β-Li_3PS_4, which has an ionic conductivity of 2.3×10^{-6} S cm^{-1} at 25 °C. Liu et al. used a wet chemical method to synthesize nanostructured β-Li_3PS_4 at room temperature. They found that the reaction of Li_2S and P_2S_5 can be mediated using tetrahydrofuran (THF). The as-synthesized $Li_3PS_4{\cdot}THF$ powder developed into a nanoporous structure after THF was removed at 140 °C. The resulting material has a high surface area of 15.6 m^2 g^{-1} with an average pore size of 28 nm (Figure 8d). The high surface energy of this nanoporous structure induced a chemical lattice distortion that shifts down the γ-β phase transition temperature, thus the metastable β phase is stabilized over a wider temperature range.[22] Moreover, the formation of the nanoporous structure during the dissociation of THF generates lattice defects on the surface, which results in a space-charge region and significantly enhances the ionic conductivity to 1.6×10^{-4} S cm^{-1} at 25 °C. A comparison of ionic conductivity of bulk γ- and β-Li_3PS_4 and nanoporous β-Li_3PS_4 can be seen in Figure 8e.[22] Phuc et al. used ethyl acetate as a reaction medium, and the precursor formed crystalline β-Li_3PS_4 at 160 °C with a high conductivity of 3.3×10^{-4} S cm^{-1} at room temperature.[111] This group also synthesized Li_3PS_4 by shaking the starting materials in ethyl propionate. The product had a thio-LISICON III structure, rather than β- or γ-Li_3PS_4. This material had a conductivity of 2.0×10^{-4} S cm^{-1} at room temperature.[112]

Regarding the wet synthesis of metastable glass ceramic $Li_7P_3S_{11}$, Xu et al. investigated the effects of solvents on

electrochemical behavior of $Li_7P_3S_{11}$. Their results using THF, acetonitrile (ACN), and a mixed solution of THF and ACN. ACN produces pure phase $Li_7P_3S_{11}$, while THF promotes the nucleation of side phase $Li_4P_2S_6$, as witnessed by Raman spectra of the $P_2S_6^{4-}$ peak (Figure 8f). And THF molecules were harder to remove during the evaporation process and tended to stay at the grain boundaries, which hindered Li ion migration. The sample produced with THF showed more cracks and holes, reducing the energy barrier for the nucleation of the side phase (Figure 8g). The pure material obtained from ACN exhibited the highest ionic conductivity of 9.7×10^{-4} S cm^{-1} at 25 °C.[32] Yao et al. also used ACN to make $Li_7P_3S_{11}$, which had a room temperature conductivity of 1.5×10^{-3} S cm^{-1}.[108] Moreover, $Li_7P_3S_{11}$ can also be obtained in a single solvent 1,2-dimethyoxyethane (DME) reaction, obtaining an ionic conductivity of 2.5×10^{-4} S cm^{-1} after heat treatment.[113] The discrepancy in ionic conductivity between the materials prepared by different methods could be attributed to the differences in crystallinity and presence of amorphous impurities.[113]

It is worth noting that Choi et al. prepared a phosphorous-free SSE Li_4SnS_4 in aqueous solution using preannealed Li_2S, Sn, and S as the precursor. They obtained a dry-air-stable product with a high conductivity of 1.4×10^{-4} S cm^{-1} (at room temperature). With the difficulties of processing sulfides in avoidance of moisture, this is a pioneering proof-of-concept for the scalability of coating sulfide SSEs onto active materials.[114] This group also prepared a dry air stable 0.6LiI· 0.4 Li_4SnS_4 glass in MeOH solution, and the ionic conductivity of this material was enhanced to 4.1×10^{-4} S cm^{-1} at room temperature with the addition of LiI.[115] The 0.6LiI· 0.4 Li_4SnS_4 glass can also be prepared in aqueous solution, however, water results in segregation of LiI and Li_4SnS_4 and the segregated LiI decomposes at high voltage.[114]

4. Stabilities and Interfaces

Electrolyte stability is a key factor affecting the overall performance and durability of a battery. In this section, we reviewed both computational and experimental results of the electrochemical window of sulfides and chemical stability of sulfides against Li metal and cathode oxide materials, as well as the chemical stability of sulfides in humid air. At the end of this section, we discussed possible approaches to improve stabilities.

4.1. Electrochemical Stabilities

Aside from a high Li ion conductivity, a key requirement to enable high energy density solid-state batteries is to have a solid electrolyte with a broad electrochemical stability window. Electrolyte decomposition could give rise to a high interfacial resistance and restrict the performance of the battery. As mentioned in prior sections, early experiments have shown that most sulfide electrolytes (including glass and crystals) have a high potential stability, with some electrolytes being stable upwards of 10 V versus Li/Li$^+$.[16,116] However, according to the work of Han et al., the electrochemical stability of solid electrolyte materials is often overestimated because of the limitations of the testing procedures. The testing cell configuration of a Li/solid electrolyte/blocking electrode (Pt or stainless steel) limits reaction kinetics, and Li mobility could also be hindered by the thin interfacial layer formed at the electrode surface.[117] The intrinsic electrochemical stability of most solid electrolytes is often lower than reported. For some sulfide materials, the electrochemical stability window is intrinsically limited by the reduction of P or Ge and the oxidation of S.

By calculating the Li chemical potential $\mu_{Li}(\phi)$ and energy of phase equilibria $E_d(\phi)$ at applied potential ϕ using density functional theory (DFT) computations, Zhu et al. investigated the intrinsic electrochemical window of common solid electrolytes and determined the thermodynamically favorable decomposition products (**Table 2**).[118] Generally, the sulfide materials are not thermodynamically stable against Li, whereas the decomposition reaction against Li is highly favorable. The reduction of LGPS starts at 1.71 V versus Li, and similar to LGPS, other sulfides such as $Li_{3.25}Ge_{0.25}P_{0.75}S_4$, Li_3PS_4, Li_4GeS_4, and Li_6PS_5Cl are also reduced at 1.6–1.7 V (**Figure 9**a). Compounds containing Ge, Cl, and I will be reduced into Li–Ge, LiCl, and LiI, respectively. $Li_7P_3S_{11}$ is reduced at a higher voltage of 2.28 V into Li_3PS_4 and then it is further reduced at 1.71 V.[118] The decomposition products, which are often binary compounds such as Li_2S, Li_3P, and LiI, are more stable against Li. The electron insulation of these unwanted products can stabilize the interphase and prohibit further decomposition of the electrolyte. Additionally, oxidation reaction of sulfides is highly favorable and sulfides can be oxidized at beyond 2 V (Figure 9b).

Through a combined theoretical and experimental study, Han et al. calculated that the true electrochemical window of LGPS is 1.7–2.1 V. The reduction of LGPS occurs at 1.71 V

Table 2. Thermodynamic electrochemical window of solid electrolyte materials.[118]

Material	Reduction potential [V]	Phase equilibria at reduction potential	Oxidation potential [V]	Phase equilibria at oxidation potential
Li_2S	N/A	Li_2S (stable at 0 V)	2.01	S
LGPS	1.71	P, Li_4GeS_4, Li_2S	2.14	Li_3PS_4, GeS_2, S
$Li_{3.25}Ge_{0.25}P_{0.75}S_4$	1.71	P, Li_4GeS_4, Li_2S	2.14	Li_3PS_4, GeS_2, S
Li_3PS_4	1.71	P, Li_2S	2.31	S, P_2S_5
Li_4GeS_4	1.62	Li_2S, Ge	2.14	GeS_2, S
$Li_7P_3S_{11}$	2.28	Li_3PS_4, P_4S_9	2.31	S, P_2S_5
Li_6PS_5Cl	1.71	P, Li_2S, LiCl	2.01	Li_3PS_4, LiCl, S
$Li_7P_2S_8I$	1.71	P, Li_2S, LiI	2.31	LiI, S, P_2S_5

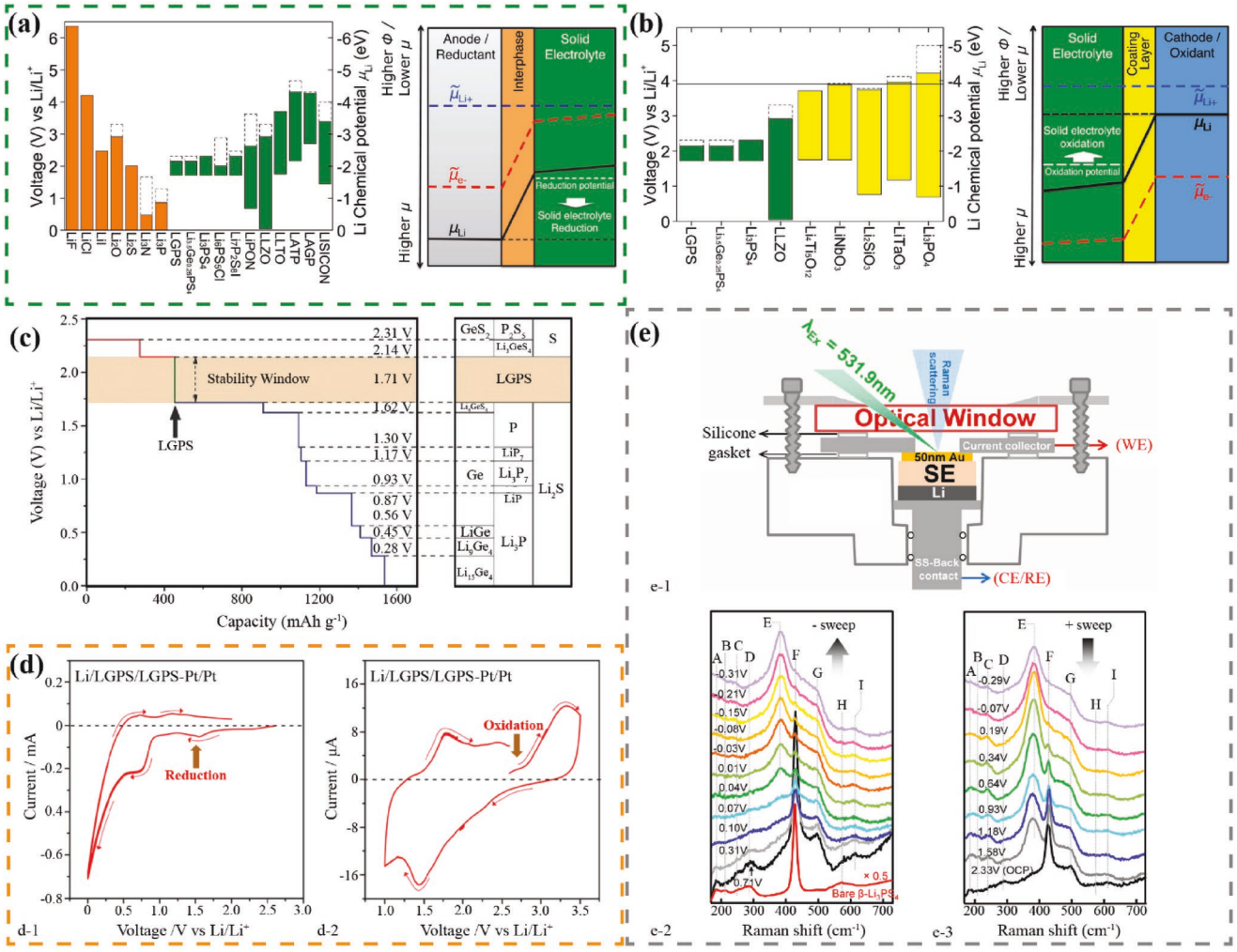

Figure 9. a) Electrochemical window (solid color bar) of solid electrolyte and other materials. The oxidation potential to fully delithiate the material is marked by the dashed line. And schematic diagram about the change of Li chemical potentials μL_i (black line), the electrochemical potential $\tilde{\mu}_{Li+}$ (blue dashed line), and $\tilde{\mu}_{e-}$ (red dashed line) across the interface between the anode and the solid electrolyte. Since the actual profile of $\tilde{\mu}_{e-}$ determined by the charge carrier distribution may be complicated, the profiles of chemical and electrochemical potential shown here are schematic and may not be linear. The vertical scale is for the electrostatic potential or the voltage referenced to Li metal and is reversed for the chemical potential or electrochemical potential. Reproduced with permission.[118] Copyright 2015, American Chemical Society. b) Electrochemical stability window (solid color bars) of commonly used coating layer materials. The oxidation potential to fully delithiate the material is marked by the dashed line. The line at 3.9 V represents the equilibrium voltage of the $LiCoO_2$ cathode material. And schematic diagram about the change of Li chemical potentials μL_i (black line) and the electrochemical potential $\tilde{\mu}_{Li+}$ (blue dashed line) and $\tilde{\mu}_{e-}$ (red dashed line) across the interface between the solid electrolyte and the cathode material. Reproduced with permission.[118] Copyright 2015, American Chemical Society. c) The first principles calculation results of the voltage profile and phase equilibria of LGPS solid electrolyte upon lithiation and delithiation. d) Cyclic voltammetry of Li/LGPS/LGPS-Pt/Pt semiblocking electrode at a scan rate of 0.1 mV s^{-1} in the voltage range of 0–2.0 V and 1.0–3.5 V. c,d) Reproduced with permission.[117] Copyright 2016, Wiley-VCH. e-1) Spectro-electrochemistry cell designed for operando Raman spectroscopic measurement at solid electrolyte and thin film metal electrode interface. e-2,e-3) Operando Raman spectra at β-Li_3PS_4 solid electrolyte and 50 nm Au interface during negative (e-2) and positive (e-3) potential sweeps. e) Reproduced with permission.[119] Copyright 2017, American Chemical Society.

where LGPS is lithiated into Li_4GeS_4, P, and Li_2S. And the oxidation of LGPS occurs at 2.14 V where LGPS is delithiated into Li_3PS_4, S, and GeS_2 (Figure 9c). The Li/SSE/blocking electrode (i.e., Pt) cell cannot depict reduction/oxidation peaks due to the low reaction kinetics. The authors applied a Li/SSE/SSE-carbon (C)/Pt cell to mimic the true microstructural environment in a solid-state battery and observed the decomposition reactions predicted by thermodynamics. Carbon mixed with SSE can increase the electronic conductivity of SSE and thus facilitate the theorized decomposition reaction.[117] According to the cyclic voltammetry of the Li/LGPS/LGPS-C/Pt cell, LGPS was reduced at 1.7 V and oxidized at 2.1 V, agreeing well with theoretical calculations. To rule out the possible reaction between LGPS and carbon, carbon was replaced with Pt powder, and the same results were demonstrated (Figure 9d).[117]

Operando Raman spectroscopy of Li/SSE/Au cell was used by Sang et al. to study the potential-dependent decomposition of β-Li_3PS_4 and LGPS, respectively, at the SSE/Au interface, where the Li^+ redox and transport require destruction and re-construction of the framework of SSE. The experimental setup is shown

in Figure 9e, and the Raman spectra during negative and positive potential sweep of Li/β-Li_3PS_4/Au is shown in Figure 9f. The couple behavior of peak E (assigned to $P_2S_6^{4-}$) and peak F (assigned to PS_4^{3-}) suggested PS_4^{3-} units degrade during Li^+ removal from the electrolyte, forming $P_2S_6^{4-}$ units with S-containing species such as Li_2S. $P_2S_6^{4-}$ can convert back to PS_4^{3-} during Li^+ insertion from the electrolyte. Similarly, Raman spectra collected on the Li/LGPS/Au cell suggested a smaller electrochemical window of LGPS, and more irreversible degradations.[119]

By controlling synthesis parameters and the consequent microstructural compositions of $Li_{9.54}Si_{1.74}P_{1.44}S_{11.7}Cl_{0.3}$ electrolyte, Wu et al. recently showed that the voltage stability window can be improved.[120] A core–shell structure was made, where a single crystalline $Li_{9.54}Si_{1.74}P_{1.44}S_{11.7}Cl_{0.3}$ core was enclosed by an amorphous shell. With the protection of the shell, the voltage window of these materials can be expanded to 0.7–3.1 V, much larger than the reported 1.7–2.1 V.[117] As the annealing temperature is increased (from 450 to 500 °C), the content of Si in the shell decreased from ≈40 to 10%, while that of S increased from ≈40 to ≈80%. And the materials treated at lower temperature (higher Si content) showed less decomposition beyond 3.1 V. Theoretical calculations of the passivation effects were carried out from the view point of mechanical compressibility of the structure. Because the decomposed products of the core are larger than the pristine material and a rigid shell inhibits expansion, the decomposition reaction cannot occur if the energy needed is less than the energy to compress the surroundings to make room for the reaction products. Within the group of the materials being studied, the mechanical modulus tended to increase with increasing Si content and decrease with increasing S content. This study emphasized the opportunity of mechanical passivation of the sulfide materials by microstructural design. The authors suggested that if the passivation layer is ionically conductive and rigid with a modulus of 20–30 GPa, passivation via mechanical compression could be realized. However, other factors such as lattice disordering due to compression must be considered.[120]

4.2. Interfaces—Chemical Stabilities and Formation of Interphases

In contrast to batteries built with liquid electrolytes, in ASSBs the electrochemical reactions take place through the solid–solid interface between the electrolyte and the electrode. Therefore, it is critical to form favorable interfaces for effective ion and electron transport. The high interfacial resistance usually originates from several factors including the poor physical interfacial contact between solids, the formation of space-charge and interphase layers due to chemical and electrochemical reactions.[121,122]

4.2.1. Interface of SSE and Li Metal Anode

Lithium metal has been considered the ideal anode for LIBs, due to its high theoretical capacity (3840 mAh g^{-1}), low electrochemical potential (–3.04 V vs standard hydrogen electrode) and light weight (0.534 g cm^{-3}).[6,123] However, in a conventional battery (with liquid electrolyte) the usage of Li metal carries many safety issues. The uneven plating and stripping of Li metal resulted from the inhomogeneous distribution of current lead to dendrite formation and rapid cell degradation. Dendrites render severe safety risks leading to short circuits, which can cause fires and explosions.[124] The failure of using Li metal as an anode prompted the transition from using "Li metal" to "Li ion," where host materials were used as anodes. Currently, LIBs' anodes are primarily graphite (Gr), which can intercalate/deintercalate Li^+ reversibly. However, the Li^+ storage capacity of Gr (372 mAh g^{-1}) is only one tenth of that of Li metal.[125] As a result of replacing Li metal with Gr, a loss in energy density is exchanged for an upgrade in safety.

Because of the solid nature and potential stability against Li metal, SSEs can act as a physical barrier to suppress Li dendrite and ensure a safer battery. According to Wenzel et al., three types of Li metal/SSE interfaces can be identified. In Type I, SSE is thermodynamically stable against Li where SSE and Li are in thermodynamic equilibrium. For Type II, SSE is thermodynamically unstable against Li. The reaction products are mixed ionic and electronic conductors, which cannot form a stable SEI. In this case, the interphase behaves like an active material, which can be lithiated/delithiated and deteriorate the battery performance rapidly. Last, Type III is SSE is thermodynamically unstable against Li. Reaction products are electronically insulating but ionically conducting. In this case a stable SEI can form and the growth rate of the SEI is limited (**Figure 10**a).[126] Wenzel et al. used in situ X-ray photoelectron spectroscopy (XPS) to observe the reaction products of LGPS, $Li_7P_3S_{11}$, and Li_6PS_5X (X = Cl, Br, or I) as Li metal was deposited onto the sulfide materials (Figure 10b).[63,127,128] Consistent with theoretical predictions, Li_2S, Li_3P, and LiX (X = Cl, Br, or I) were formed at the interphase and the growth of the interphase gradually slowed down as more Li metal was deposited. Witnessed by time-resolved electrochemical impedance spectroscopy (EIS), the interfacial resistance grows larger as the interphase grows thicker (Figure 10c,d). Using similar techniques, this group confirmed that $Li_7P_3S_{11}$ decomposed into Li_2S, Li_3P, and LGPS decomposed into Li_2S, Li_3P and Ge metal or Li–Ge alloy when in contact with Li metal.[63,128]

Based on time-dependent electrochemical impedance spectroscopy of Li/SSE/Li cell data, Wenzel et al. quantified the evolution of SEI resistance as a function of time for LGPS, $Li_7P_3S_{11}$, and Li_6PS_5X as shown in **Figure 11**a–c. Based on the results, they developed a model based on diffusion-controlled solid-state reaction to quantify the growth of the interphase. The model considered the thickness, growth time, density, and electronic and ionic conductivity of the SEI layer. The parabolic rate constant k used to describe the evolution of the interphase resistance was derived from the model. The results predicted that in order to have a stable SEI a low electronic conductivity and a high ionic conductivity are desirable. Among Li_6PS_5X, $Li_7P_3S_{11}$, and LGPS, $Li_7P_3S_{11}$ showed the lowest parabolic rate constant and, therefore, the lowest interphase growth rate. LGPS showed the highest parabolic rate constant likely due to the formation of the electronically conducting Li–Ge alloy. Among Li_6PS_5Cl, Li_6PS_5Br, and Li_6PS_5I, Li_6PS_5I showed an exceptionally high rate of interphase growth compared to the other two without a definite reason (Figure 11d and **Table 3**).[127]

Similar instability against Li metal was also found in Li_3PS_4 material. Lepley et al. modeled the Li_3PS_4/Li interface and

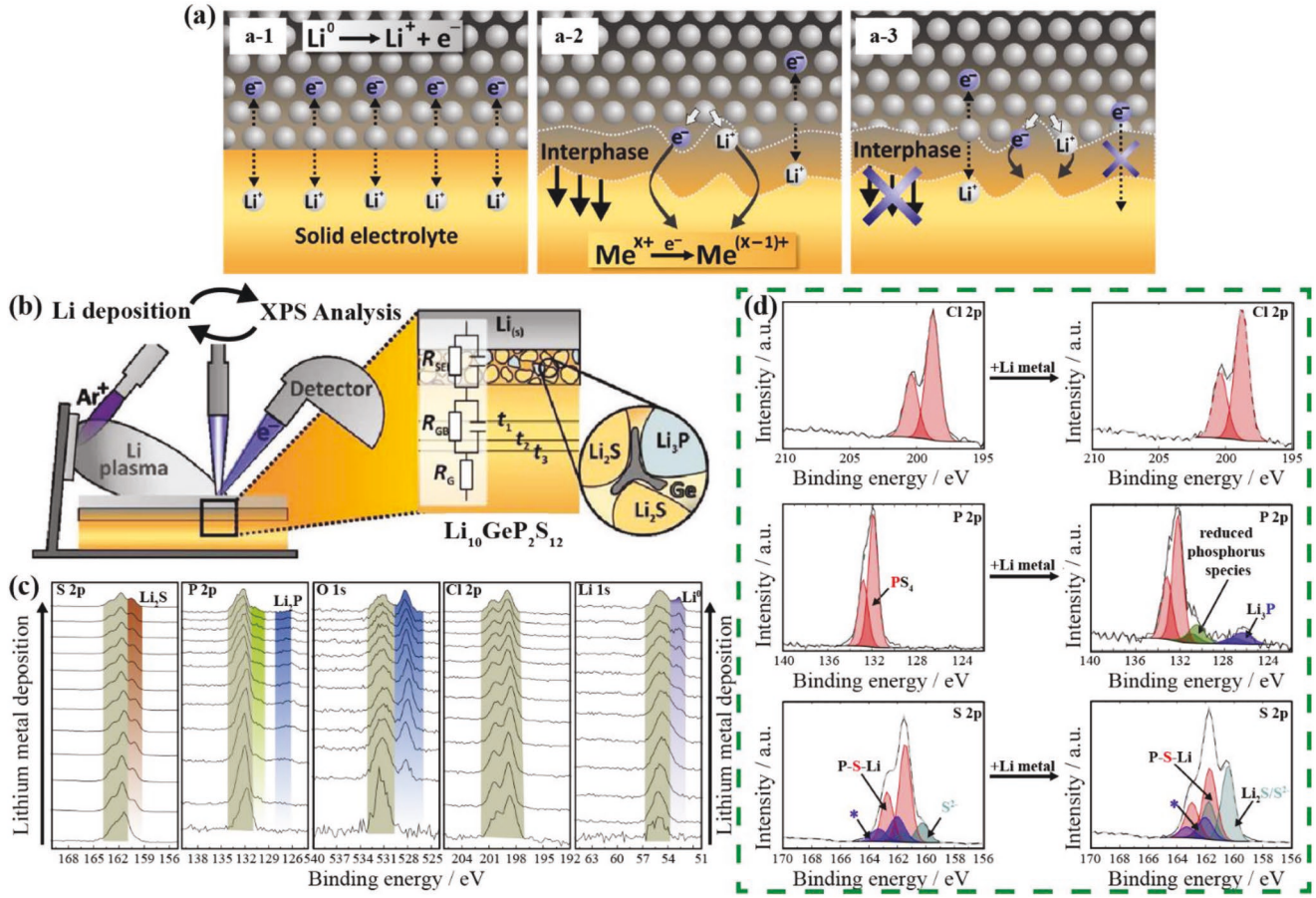

Figure 10. a) Types of interfaces between Li metal and SSE. a-1) Non-reactive and thermodynamically stable interface. a-2) Reactive and mixed conducting interphase. a-3) Reactive and metastable SEI. Reproduced with permission.[126] Copyright 2015, Elsevier. b) Experimental setup of the in situ XPS experiment to monitor the reaction between sulfide and Li. Reproduced with permission.[128] Copyright 2016, American Chemical Society. c) S 2p, P 2p, O 1s, and Cl 2p XPS spectra of a Li_6PS_5Cl sample as a function of increasing amount of Li metal being deposited (from bottom to top). The formation of new species is colored and labelled, showing the decomposition of the original SSE phase into Li_2S, Li_3P, and Li_2O. The Cl 2p spectrum and with it the binding state of Cl^- does not change significantly. d) XPS detail spectra and peak fits for the pristine (left) and the reacted (right) sample are shown for Cl 2p, P 2p, and S 2p. c,d) Reproduced with permission.[127] Copyright 2018, Elsevier.

found that the crystal structure of Li_3PS_4 surface can be altered in the presence of Li metal.[130] However, experimentally, compounds such as Li_3PS_4 and $Li_7P_2S_8I$ are found to be compatible with Li metal anodes, as the decomposition products such as Li_3P, Li_2S and LiI are electronically insulate and stable against Li metal. The decomposition products can form an interphase layer, which can passivate the reaction between Li and solid electrolyte (Type I interphase).[22,130] Yamada et al. monitored the stability of Li_3PS_4 with Li and found the cell impedance increased in the first 2 d and then became constant, indicating the formation of a passivating film. However, the interphase formed between Li and Li_3PS_4 can be destroyed under stripping/plating of Li, which reduced the resistance to ion conduction. And a chemically unstable interface could deteriorate the uneven stripping/plating of Li.[131] As modeled by Lepley et al., when there was a thin film of Li_2S imposed on the surface of Li_3PS_4, the structure was found to be very stable.[130]

To eliminate the direct exposure of Li metal to sulfide SSE, Gao et al. introduced a nanocomposite layer formed by in situ electrochemical reduction of liquid electrolytes on the Li metal using a constant current (Figure 11e). Several liquid electrolytes were selected and the nanocomposite layers formed from these electrolytes all stabilized the interphase between LGPS and Li. Furthermore, they all prevented the decomposition of LGPS. In the cycling test of Li/LGPS/Li symmetric cells, the optimal liquid electrolyte was 1 M LiTFSI in dioxolane (DOL)/dimethoxyethane (DME) (Figure 11e). The thickness of the interphase formed in 1 M LiTFSI in DOL/DME was estimated to be 90 nm. And in respect of composition of the interphase, organic species $LiO–(CH_2O)_n–Li$ and inorganic species such as LiF, C—F bonds and —N—SO bonds were both observed (Figure 11e). These bonds are different because only inorganic species were observed in the nanocomposite layers formed in other liquid electrolytes investigated in this study.[129] Sang et al. evaluated two interlayer materials, Si and Al_2O_3, at the interface of $Li_7P_3S_{11}$ and Li metal. Si (20 nm) was sputtered onto $Li_7P_3S_{11}$ pellet with the protection of Au, and Al_2O_3 (10 nm) was deposited onto Li metal using atomic layer deposition (ALD). Li/ $Li_7P_3S_{11}$/Li symmetric cells with and without the interlayers were tested by CV and EIS, and the interfaces were characterized by XPS

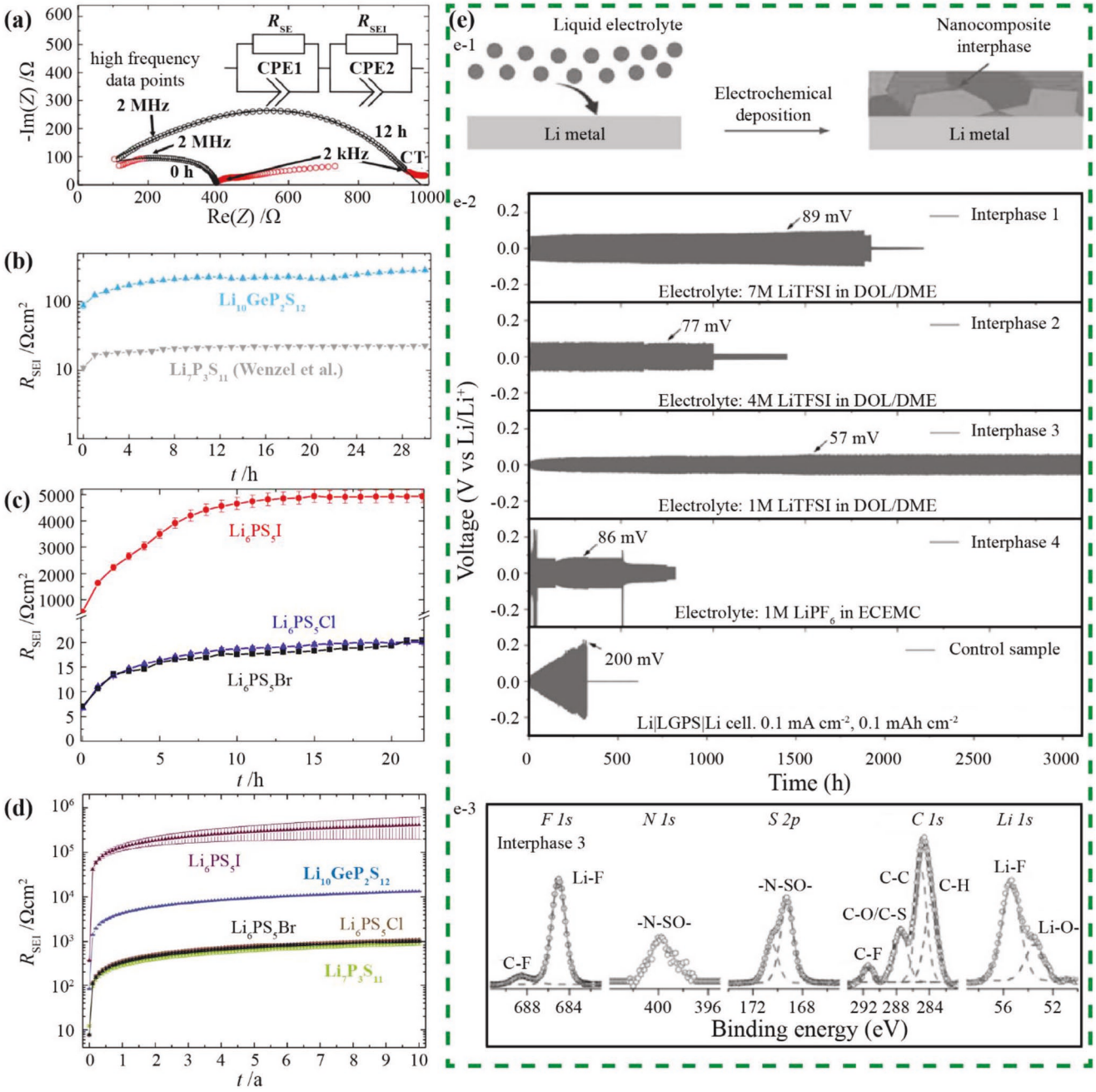

Figure 11. a) Impedance of a Li/LGPS/Li cell directly after assembly (0 h) and after 12 h. The equivalent circuit used as fit model is shown in the inset. Red data points were removed for the fitting process. Reproduced with permission.[128] Copyright 2016, American Chemical Society. b) Increase of the LGPS/Li interphase resistance, in comparison to $Li_7P_3S_{11}$/Li. The uncertainty of the fit is drawn as error bars, which are generally significantly smaller than 5 Ω cm^2. Reproduced with permission.[128] Copyright 2016, American Chemical Society. The data for LGPS/Li were presented in ref. [128]. The data for $Li_7P_3S_{11}$/Li were originally presented in ref. [63]. c) Impedance of a Li/ Li_6PS_5X/Li cell directly after assembly (0 h) and after 20 h. The increasing resistance appears to show asymptotic behavior after initial growth. d) Simulation of the SEI resistance over 10 years for $Li_7P_3S_{11}$, LGPS, Li_6PS_5Cl, Li_6PS_5Br, and Li_6PS_5I using the parabolic rate constants in Table 3. Error bars were derived from the fit errors. c,d) Reproduced with permission.[127] Copyright 2018, Elsevier. e) Design of the nanocomposite interphase. e-1) Illustration of the formation of the nanocomposite on Li via the electrochemical decomposition of a liquid electrolyte. e-2) The voltage profiles of Li deposition in Li/LGPS/ Li cells. Interphase 3 enabled the optimal interfacial stability. e-3) High-resolution XPS spectra of interphase 3, composed of organic and inorganic salts. e) Reproduced with permission.[129] Copyright 2018, Wiley-VCH.

and Raman. Both Si and Al_2O_3 can dramatically improve the cycle life, although at the cost of increased interfacial resistance. In all cases, Li_2S was found as a decomposition product at the interface after the cells were shorted. The $Li_xAl_{(2-x/3)}O_3$ interlayer can drop the potential between $Li_7P_3S_{11}$ and Li and thus suppress the decomposition of $Li_7P_3S_{11}$, while Si lithiates

Table 3. Parabolic rate constants of sulfide SSEs.[127]

Material	Parabolic rate constant [k Ω^{-1} cm^{-2} $h^{-0.5}$]	Intercept [Ω cm^2]
$Li_7P_3S_{11}$	2.9 ± 0.3	12.3 ± 0.6
LGPS	45.1 ± 1.0	83.9 ± 2.3
Li_6PS_5Cl	3.8 ± 0.2	7.4 ± 0.4
Li_6PS_5Br	3.4 ± 0.2	7.8 ± 0.5
Li_6PS_5I	1394.3 ± 43	361 ± 96

and maintains reducing potentials which facilitate the decomposition of $Li_7P_3S_{11}$. This work proved that the interlayer material has an impact on the electrochemical potential at the Li/SSE interface, and therefore impact the chemical reactions occurring at the interface.[132]

Another approach to stabilize the interface is to use multiple electrolytes. Yao et al. adopted a bilayer SSE, where a Li-compatible SSE layer of $75Li_2S \cdot 24P_2S_5 \cdot 1P_2O_5$ electrolyte was inserted between LGPS and Li metal.[133] Furthermore, to avoid the chemical instability of sulfides against Li metal, Li–In alloy is commonly used in sulfide SSE in all-solid-state batteries. It was found that an indium thin film deposited on the surface of Li metal can spontaneously alloy with Li, stabilizing the interface while maintaining fast ion conduction.[134] The potential of Li–In is constant at 0.6 V versus Li/Li^+ when the molar ratio of Li to In is less than 1.[135] Thus the use of Li–In sacrifices the energy density of the battery compared to sole Li metal batteries. Additionally, to ensure sufficient physical contact between SSE and Li metal, Nagao et al. inserted a Li thin film between the $80Li_2S \cdot 20P_2S_5$ glass and Li metal anode by evaporation Li on the SSE. The contact area between Li and SSE was increased, which contributed to the reversible Li stripping/plating.[136]

4.2.2. Interface of SSE and Cathode Materials

To increase energy of ASSBs, the ideal cathode should have a large voltage window and/or high capacity. In most cases, high voltage cathodes (up to 5 V) have medium to low capacity (i.e., $LiMn_2O_4$), while high capacity Li metal oxides (i.e., $LiNi_{(1-x-y)}Co_xMn_yO_2$) have high capacities (>200 mAh g^{-1}) but lower voltage (4.4–4.8 V). Therefore, there is a need to carefully study the interface of these active materials when combined with solid electrolytes.

Richards et al. predicted the stability of the interface of sulfide electrolytes and oxide cathode materials by calculating the reaction energy. Sulfides materials generally have large reaction energy when paired with layered $LiCoO_2$(LCO) and $LiNiO_2$ cathode materials, due to their high voltage and high oxygen chemical potential. As an example, PS_4 groups in sulfides can react with cathode oxides to form PO_4 groups and metal sulfides. Generally, sulfide electrolytes are more unstable than oxide electrolytes (**Figure 12**a).[137] Auvergniot et al. investigated the chemical stability of argyrodite Li_6PS_5Cl against LCO, $LiNi_{1/3}Co_{1/3}Mn_{1/3}O_2$ (NCM111), and $LiMn_2O_4$ (LMO) cathode materials. They used Auger electron spectroscopy (AES) and XPS to characterize electrolyte-containing electrode at different depths before and after cycling. They confirmed that at the interface with the active materials (within the electrode), Li_6PS_5Cl was oxidized into elemental sulfur, lithium polysulfides, P_2S_x ($x \geq 5$), phosphates, and LiCl (Figure 12b). Confirmed by XPS data, the LMO/ Li_6PS_5Cl composite electrode was unstable even before the beginning of the electrochemical process. In addition to XPS data, AES mapping data in Figure 12c,d provided more lateral resolution. After cycling, there were clear distinctions between sulfur-rich particles and chlorine-rich particles, meaning that Li_6PS_5Cl was oxidized. In the case of NCM111/ Li_6PS_5Cl, the oxidation process was partially reversible. It did not hinder the cyclability of the battery, revealed by the good capacity retention after 300 cycles (NCM111/ Li_6PS_5Cl/Li-In half cell).[138] Sakuda et al. observed the formation of an interfacial layer between LCO and $Li_2S \cdot P_2S_5$ electrolyte using transmission electron microscopy (TEM). The interface layer was comprised of Co and S, and mutual diffusion of Co, S, and P between the electrode and electrolyte was confirmed.[139] Additionally, Chen et al. investigated the interfacial stability between sulfide SSEs (Li_3PS_4, $90Li_3PS_4 \cdot 10LiI$, and $90Li_3PS_4 \cdot 10LiCl$) and cathode active material $LiNi_{0.8}Co_{0.1}Mn_{0.1}O_2$ (NCM811), $LiNi_{0.6}Co_{0.2}Mn_{0.2}O_2$ (NCM622), and $LiNiCoAlO_2$ (NCA) by monitoring the ionic conductivity of composite materials which consist of sulfide SSE and active material in a weight ratio of 1:1. The ionic conductivity dropped drastically with respect to time, which implies the instability of these sulfides with their respective active materials.[140] Koerver et al. recently applied in situ EIS and XPS to monitor the behavior of the interface between NCM811 cathode and Li_3PS_4 SSE with respect to voltage. Most of this interphase formed irreversibly in the first cycle and was caused by oxidation of the electrolyte. The formation of interphase was detrimental to capacity retention. The amount of oxidized SSE (oxidized sulfur and phosphorus species) increased with increasing cycle number. Quantification of the P–O species, which was an indication of reaction between active material and SSE, suggested 1% of the total SSE reacted with active material. Another factor that contributed to the capacity fade was mechanical deflation of cathode due to volume expansion of NCM materials.[141]

A major factor contributing to the large interfacial resistance between sulfide SSEs and oxide cathode materials is the space-charge layer. This is created by Li ion transfer from the electrolyte to the cathode as a result of the significantly different chemical potential between Li^+ in the cathode and that in the sulfide electrolyte, leaving a highly resistive Li^+ deficient layer on the electrolyte side of the interface.[121,143] When the oxide cathode containing mixed ion and electron conducting, the concentration gradient of Li^+ can be balanced by electronic conduction and the space-charge layer should disappear on the oxide side of the interface. As a result, more Li^+ will transfer from the electrolyte to the cathode to reach equilibrium, developing a thicker space-charge layer and thus a higher interfacial resistance.[144] Cathode coatings can improve the stability of the interface by physically isolating the electrolyte and electrode. The coatings can act as a buffer layer to suppress the formation of the space-charge layer. Materials commonly used such as $Li_4Ti_5O_{12}$ (LTO),[144,145] $LiTaO_3$,[146] $LiNbO_3$ (LNO),[143,147] Li_2SiO_3,[139,148] Li_3PO_4,[149] ZrO_2,[150] and Al_2O_3[151] usually demonstrate a wide

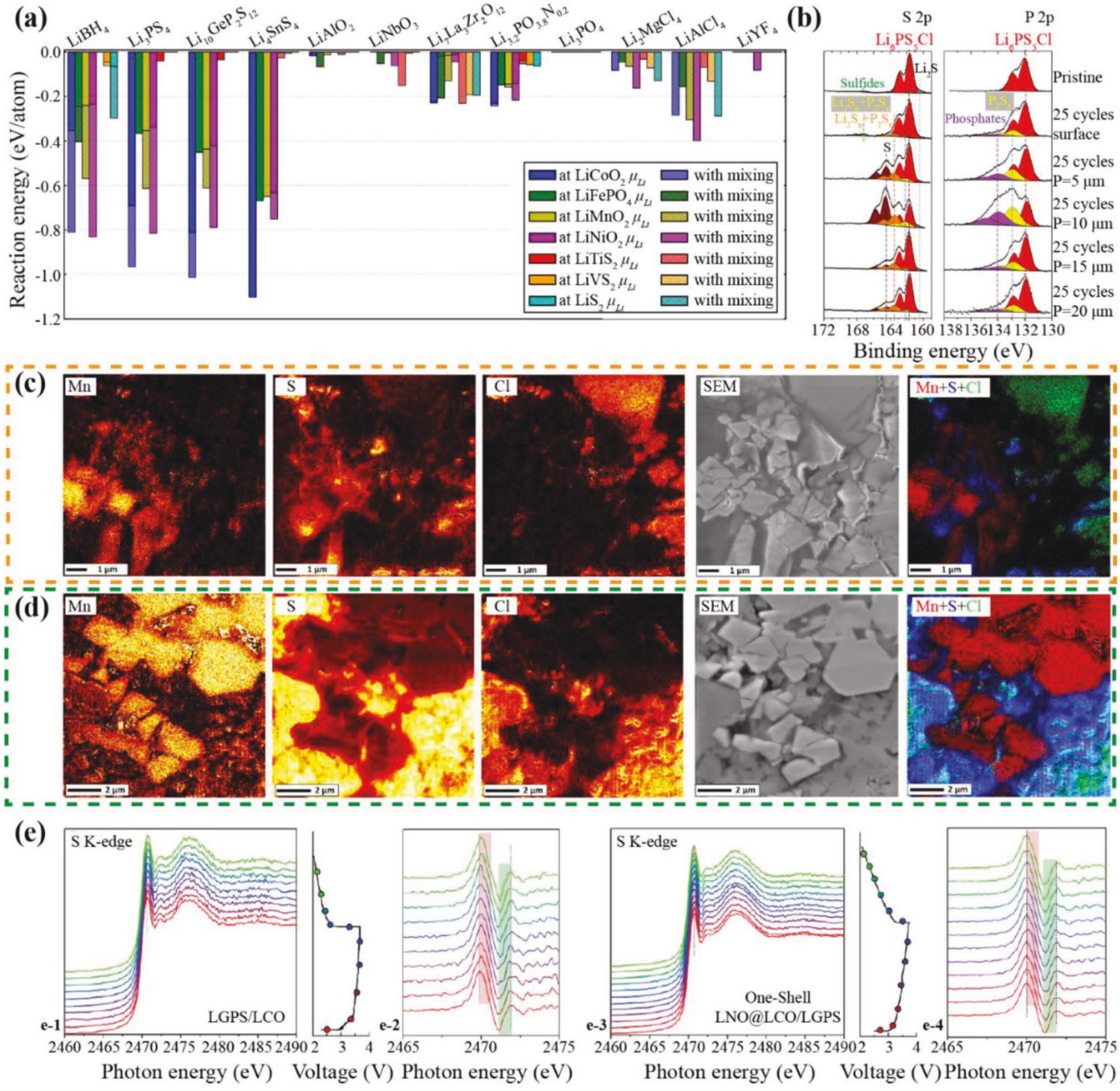

Figure 12. a) Reaction energies for the interfaces of a selection of cathode/electrolyte combination at Li chemical potential μL_i corresponding to the average cathode voltage. Energies are given both for the energy of the lithium extraction only (no mixing) and for energy of cathode/electrolyte mixing open to lithium. Combinations with decomposition energies close to zero are expected to form stable interfaces. Reproduced with permission.[137] Copyright 2016, American Chemical Society. b) S 2p and P 2p XPS spectra of the composite LCO electrode of LCO/Li_6PS_5Cl/Li–In half-cells: before cycling (pristine), after 25 cycles, and after 25 cycles with increasing etching depths of the electrode from 5 to 20 μm. c) SEM image and scanning Auger microscopy (SAM) mapping of Mn, S, and Cl elements from a cross section of the composite LMO electrode of the LMO/Li_6PS_5Cl/ Li–In half-cell before cycling (pristine) (bar = 2 μm). d) SEM image and SAM mapping of Mn, S, and Cl elements from a cross section of the composite LMO electrode of the LMO/ Li_6PS_5Cl/Li–In half-cell after 22 cycles (bar = 1 μm). b–d) Reproduced with permission.[138] Copyright 2017, American Chemical Society. e) In situ XANES of ASSBs during the initial charge–discharge process. e-1) S K-edge of the bare LCO/LGPS cathode. e-2) The first deviation of the S K-edge spectra of the bare LCO/LGPS electrode. e-3) S K-edge of the one-shell LNO–LCO/LGPS electrode. e-4) The first deviation of S K-edge spectra of one-shell LNO–LCO/LGPS electrodes. e) Reproduced with permission.[142] Copyright 2019, Wiley-VCH.

electrochemical stability window and good chemical compatibility with both the cathode materials and electrolyte. The most studied coating material is LNO, which has a conductivity of 10^{-6} S cm^{-1} at room temperature.[10,115,143,152] Wang et al. performed operando X-ray near edge spectroscopy (XANES) on a LGPS/LNO/LCO core–shell material to unveil the suppression of interfacial reactions between LCO and LGPS by LNO. Sulfur K-edge XANES of LCO and LNO-coated LCO with

respect to discharge/charge are presented in Figure 12e-1,e-2, and the subtracted first-order derivation spectra in Figure 12e-3, e-4. It is apparent that, without LNO, LGPS/LCO presented more shoulder peaks at 2470 and 2472 eV, indicating that LNO can suppress the reactions between LCO and LGPS. More recently, Jung and co-workers reported a $Li_{3-x}B_{1-x}C_xO_3$ (LBCO) coating on LCO particles prepared in aqueous solution, where the process can convert the Li_2CO_3 as a surface impurity of LCO into ionically conducting LBCO.[153] Although pure-phase Li_3BO_3 has a low ionic conductivity in the range of 10^{-9} S cm^{-1} at room temperature,[154] the addition of isostructural Li_2CO_3 can improve the ionic conductivity to 6×10^{-7} S cm^{-1} at $x = 0.8$. Additionally, this coating can prevent the formation of interfacial phase, Co_3S_4, formed between LCO and sulfide SSE. Alternatively, phosphate-based interphase was formed between LBCO and sulfide.

The oxidation potential of these coating materials is higher than that of the solid electrolyte, which makes them more stable against the cathode active oxide materials. Moreover, the interposition of a coating induces two interfaces: one between the electrode and the coating and the other between the coating and electrolyte. The coating-SSE interface is more stable than the cathode-SSE interface, since both coating and electrolyte are electronically insulating, a thick interphase formation is constrained, giving rise to a stable electrode–electrolyte interface.[121]

In the case of Li–S batteries, the large charge transfer resistance between the sulfide SSE and sulfur cathodes arises from the large volume expansion during cycling of sulfur and therefore a loss of physical contact between the SSE and electrode. The key challenge is to reduce the stress and strain on the interface and ensure an ionic and electronic transfer pathway.[155,156] Regarding the electrolyte, the usage of composite electrolytes (crystalline sulfides and polymers and/or liquid electrolyte) has been proven to be effective at mitigating interfacial resistance. This approach has mainly been applied to oxide electrolyte.[157] Regarding the electrode, composition optimization and nanosizing active materials have been proved to be effective at reducing large interfacial issues. Eom et al. used vapor grown carbon fiber (VGCF). The VGCF film controlled and contained the formation of nanocrystal Li_2S optimizing the contact area between $Li_2S \cdot P_2S_5$ solid electrolyte and conductive carbon inside the electrode. The composite electrode employs both 1D VGCF and 0D carbon powder to realize a conductive framework to achieve both simple electron conduction and effective contact with Li_2S active material.[158] Yao et al. deposited nanoamorphous sulfur on reduced graphene oxide (rGO). Then, the nanocomposite was mixed with LGPS solid electrolyte along with carbon to form a mixed ion electrode. The nanosized sulfur increased the contact area with the electrolyte and carbon and the electronically conductive network supported by rGO buffered the volume expansion to reduce the stress and strain.[133]

4.3. Air Stabilities

Most sulfide electrolytes need to be handled under inert gas because of their instability with moisture. Sulfides are hydrolyzed in the presence of water, generating H_2S gas, Equation (2). With accompanying structural changes, the ionic conductivity of the electrolyte is compromised. For instance, clear impurity peaks in the XRD pattern were observed after Li_6PS_5Cl electrolyte were exposed to air for 10 min. And the ionic conductivity degraded from 1.8×10^{-3} S cm^{-1} for the pristine material to 1.56, 1.43, and 0.87×10^{-3} S cm^{-1} after the material was exposed to air for 10 min, 1 h, and 24 h, respectively.[105]

$$M_xS_y + H_2O \rightarrow M_xO_y + H_2S \quad (2)$$

Monitoring the amounts of H_2S generated can help track the structural changes that the electrolytes have undergone.[159] Muramatsu et al. monitored the H_2S of $Li_2S \cdot P_2S_5$ glasses containing 57, 60, 75, and 80 mol% of Li_2S using a H_2S sensor. Raman spectroscopy results have shown that H_2S was generated immediately after exposure to air. It was found that the amount of H_2S is dependent on the glass composition. The glass with 75 mol% Li_2S (as well as its crystallized form) generated the smallest amount of H_2S. Muramatsu et al. proposed that the $Li_2S \cdot P_2S_5$ electrolytes which consist of PS_4^{3+} units are more stable than those which consists of $P_2S_7^{4+}$ units, because PS_4^{3+} units are harder to hydrolyze while $P_2S_7^{4+}$ units can easily decompose to form OH groups and H_2S.[159] Using the same approach, Chen et al. investigated the mount of H_2S generated by LiI, LiCl, and P_2O_5 doped Li_3PS_4 (glass ceramic of $75Li_2S \cdot 25P_2S_5$). The pristine Li_3PS_4 and P_2O_5 doped sample showed better stability than the LiI and LiCl doped samples.

Doping sulfides with oxygen is a common way of absorbing H_2S and suppressing the formation of H_2S, illustrated in Equation (3).[160] In order to absorb H_2S effectively, oxides should have a large negative Gibbs energy change (ΔG) for the reaction with H_2S.[161]

$$N_xO_y + H_2S \rightarrow N_xS_y + H_2O \quad (3)$$

Hayashi et al. found that H_2S generation could be suppressed by partial substitution of 10 mol% P_2O_5 for P_2S_5 in the $75Li_2S \cdot 25P_2S_5$ glass system. The structure of the glass is modified with the formation of oxysulfide units and PO_4^{3-} units where the nonbridging oxygens hindered Li ion migration, and correspondingly, the ionic conductivity decreased from 5×10^{-4} S cm^{-1} at 25 °C (pristine glass) to 3×10^{-4} S cm^{-1} for the $75Li_2S \cdot 15P_2S_5 \cdot 10P_2O_5$ final product. Next, 10 mol% ZnO nanoparticles (which strongly absorb H_2S) was added to obtain $90(75Li_2S \cdot 15P_2S_5 \cdot 10P_2O_5) \cdot 10ZnO$. This addition reduced half the detected H_2S gas compared to that of the glass without ZnO. Surprisingly, the addition of ion-insulating ZnO did not jeopardize ionic conductivity and the $90(75Li_2S \cdot 15P_2S_5 \cdot 10P_2O_5) \cdot 10ZnO$ showed a conductivity of 4×10^{-4} S cm^{-1} at 25 °C.[160] Hayashi et al. investigated metal oxides (Fe_2O_3, ZnO, and Bi_2O_3) which have very negative Gibbs-free energies (ΔG) for the reaction with H_2S. ΔG of Fe_2O_3, ZnO and Bi_2O_3 are –43.9, –78.0, and –232.0 kJ mol^{-1}, respectively. The $90Li_3PS_4 \cdot 10N_xO_y$ (N_xO_y is Fe_2O_3, ZnO, or Bi_2O_3) composites all have ionic conductivities in the order of 10^{-4} S cm^{-1} at 25 °C. Among Fe_2O_3, ZnO, and Bi_2O_3, all three composites showed production of metal sulfides in XRD after the composites were exposed to air, but ZnO and Bi_2O_3 were more effective in absorbing H_2S. However, Bi_2O_3 was

not a favorable choice because of the limited electrochemical stability. Preliminary experiments on particle size of ZnO showed that it is more favorable to use metal oxides of smaller particle size to remove H_2S, but there is not a clear relationship between surface area and amount of H_2S absorbed.[162]

5. All-Solid-State Li Secondary Batteries Using Sulfide Electrolyte

This section begins reviewing approaches to fabricate electrodes and electrolytes for a sulfide-based ASSB. To avoid confusion, ASSLB denotes ASSBs with transition metal oxide cathode materials and ASSLS denotes ASSBs with sulfur cathode materials. The progress gained in recent years on ASSLBs and ASSLSs using sulfide solid electrolytes is summarized. We also introduced recent findings on ASSBs using organic cathodes and the concept of single-material ASSBs.

5.1. Preparation of Electrodes

In all-solid-state batteries, the addition of solid electrolyte in the electrodes is necessary to ensure good ionic conduction within the electrode and effective electrode/SSE interface. Solid electrolyte is physically mixed with active material and conductive carbon in either dry or wet processes.

5.1.1. Dry Methods

Mechanical milling is the most common way to reduce the particle size and form intimate contact among different solid-state electrode components. Nagao et al. found that, in contrast to the mixtures prepared by hand-grinding, ball-milling a mixture of Li_2S, acetylene black and SSE ($80Li_2S \cdot 20P_2S_5$) reduced the particles sizes from > 100 µm (large particles and agglomerates to much finer particles with sizes >10 µm.[163] In consequence, the all-solid-state cells made with the hand-grinded mixture were difficult to manipulate and showed extremely low capacity. Conversely, the cells made with the ball-milled composite had much higher reversible capacity and better performance. The intimate contact among well-dispersed Li_2S, acetylene black and SSE particles was the main reason for the large utilization of active material.[163] In addition, mechanical milling can also be carried out in multiple steps to homogeneously disperse each component and further reduce particle size. For instance, in the composite sulfur electrode, sulfur and active carbon could be milled first creating a homogeneous mixture, and then SSE could be added to the mixture to create the final cathode composite (**Figure 13**a).[56]

Physical vapor deposition (PVD) methods such as a pulse laser vapor deposition haven been used extensively to make thin electrodes. Sakuda et al. made electrode–electrolyte composite materials by coating SSE ($80Li_2S \cdot 20P_2S_5$) onto LCO particles with pulse laser deposition method, a schematic of the ASSB is shown in Figure 13b. The coating onto the SSE was 50–70 nm thick and 1% of the total weight. The coating formed an ion conductive path within the electrode and the coated-LCO showed advantageous cyclability compared to non-coated LCO.[164]

Additional treatments (generally mechanical and thermal) for the coating and SSE are also considered a crucial step in fabricating ASSB electrodes when utilizing dry methods. Kitaura et al. pressed the SSE ($80Li_2S \cdot 20P_2S_5$) and LCO at high temperature of 210 °C. They found that the grain boundary between SSE and LCO was blurrier than when it was pressed at room temperature, which proves that hot pressing increases adhesion and contact area between active materials and SSEs.[165]

A recent study conducted by Noh et al. showed that the location of carbon in the composite electrode, determined by mixing protocols, is particularly important for the performance of the electrode. The authors examined five different mixing protocols of a composite LCO/96($78Li_2S \cdot 28P_2S_5$)$\cdot 4Li_2SO_4$/Super P carbon electrode, as shown in Figure 13c. It was expected that mixing the first two components will promote interfacial contact between them. Then, the addition of a third component subsequently will have a bigger effect on interstitial regions than on interfacial contact. EIS data of In/SSE/(LCO/96($78Li_2S \cdot 28P_2S_5$)$\cdot 4Li_2SO_4$/Super P) full cell (not shown here) suggested that Samples M3, M4, and M5, which have carbon at the LCO particle's surface, showed a lower interfacial resistance. From the initial discharge data and rate performance in Figure 13d,e, it is evident that electron transport is a limiting factor at high discharge rates. To obtain high rate performance, it is crucial to ensure effective charge transfer pathways both at the interface and through the interstitial regions.[166]

5.1.2. Wet Methods

Wet methods to prepare the composite electrode include coprecipitation, dip coating, and tape-casting. Tape-casting is the process to fabricate conventional LIB electrode, where the active material, conductive, binder, and solid electrolyte are mixed as a slurry. Choi et al. coated Li_4SnS_4 electrolyte onto the surface of LCO using an aqueous solution, as illustrated in **Figure 14**a. The H_2S generation was negligible for the phosphorus-free Li_4SnS_4. Electron microscopy data in Figure 14b highlighted the good adhesion of Li_4SnS_4 to LCO particles. Considering that LCO was subject to surface degradation in aqueous solution, a high basicity of the aqueous solution (pH 11.89) was effective in minimizing surface contamination.[114] Han et al. proposed a "bottom-up" approach to prepare Li_2S composite cathode by dissolving Li_2S as the active material, poly(vinylpyrrolidone) (PVP) as the carbon precursor, and argyrodite Li_6PS_5Cl as the SSE all in ethanol solution. This mixture then went through coprecipitation and high-temperature carbonization. The nanoscale distribution of Li_2S, Li_6PS_5Cl, and carbon enabled an excellently mixed conducting electrode. However, it should be pointed out that argyrodite Li_6PS_5Cl is the only sulfide electrolyte that is compatible with ethanol.[117] Kim et al. reported a scalable fabrication protocol for ASSB electrodes by simply infiltrating conventional LIB electrodes with homogeneous SSE solutions, Li_6PS_5Cl/EtOH or 0.4LiI–0.6Li_4SnS_4/MeOH (Figure 14c). Using the conventional wet (tape-casting) processing method, polymer binder was dispersed in to

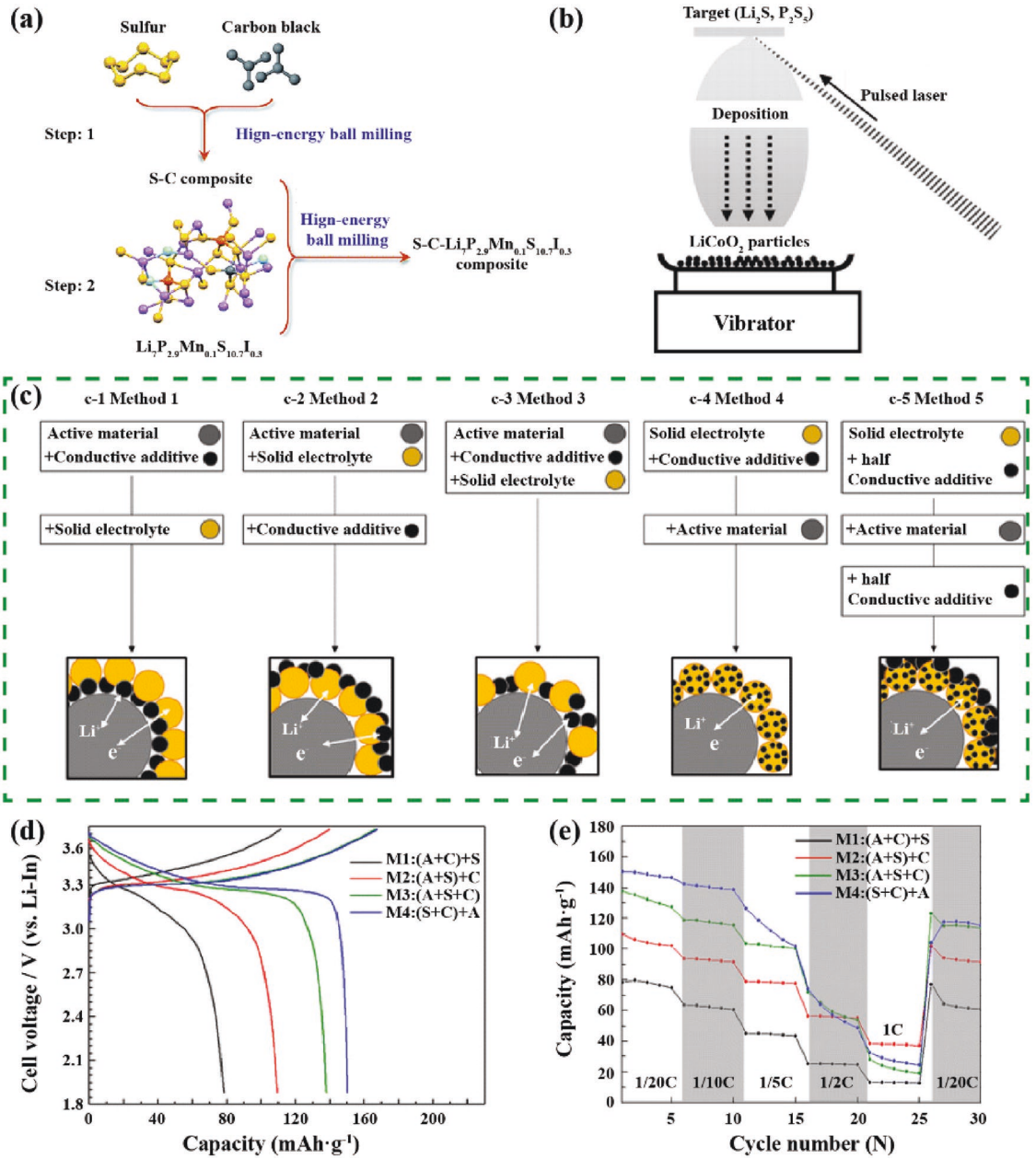

Figure 13. a) Schematic of the preparation process of S–C–$Li_7P_{2.9}Mn_{0.1}S_{10.7}I_{0.3}$ composite cathode. Reproduced with permission.[56] Copyright 2017, Royal Society of Chemistry. b) Schematic of a coating apparatus in a vacuum chamber. Reproduced with permission.[164] Copyright 2010, Elsevier. c) Protocols for the five different mixing methods along with the anticipated microstructures of the resulting composite cathodes. d) Charge–discharge curves of all-solid-state cells made from mixing methods M1–M4. Measurements were made at room temperature at 0.05C charge and discharge rate with cutoff voltages of 1.9–3.68 V (vs Li–In). (A: cathode material, S: solid electrolyte, C: conductive carbon). e) Rate capability of all-solid-state cells made with methods M2, M4, and M5. Measurements were made at room temperature at 0.05 to 1 C discharge rate with cutoff voltages of 1.9–3.68 V (vs Li–In). (A: cathode material, S: solid electrolyte, C: conductive carbon). c–e) Reproduced with permission.[166] Copyright 2018, Springer Nature Switzerland AG, part of Springer Nature.

the electrode. This step is essential for large scale roll-to-roll production of electrodes. Taking advantage of the liquid phase SSE solution, the LCO and Gr electrodes were dip-coated in SSE solution. Due to the thermal stability of polyvinylidene fluoride (PVDF) in the electrodes, the subsequent crystallization of SSE was carried out at 180 °C. Because of its limited crystallinity, the Li_6PS_5Cl heat-treated at 180 °C has lower ionic conductivity than the material treated at 550 °C (1.9×10^{-4} S cm^{-1} compared to 1.0×10^{-3} S cm^{-1} at 30 °C). The infiltration of SSE reduced porosity of the electrodes. For example, the porosity of the LCO electrode (LCO/PVDF/Super P = 96/2/2) infiltrated with 12 wt% of SSE went from 54% to 29% porosity after infiltration and then to 7.3% after cold pressing. The decrease in porosity can be attributed to

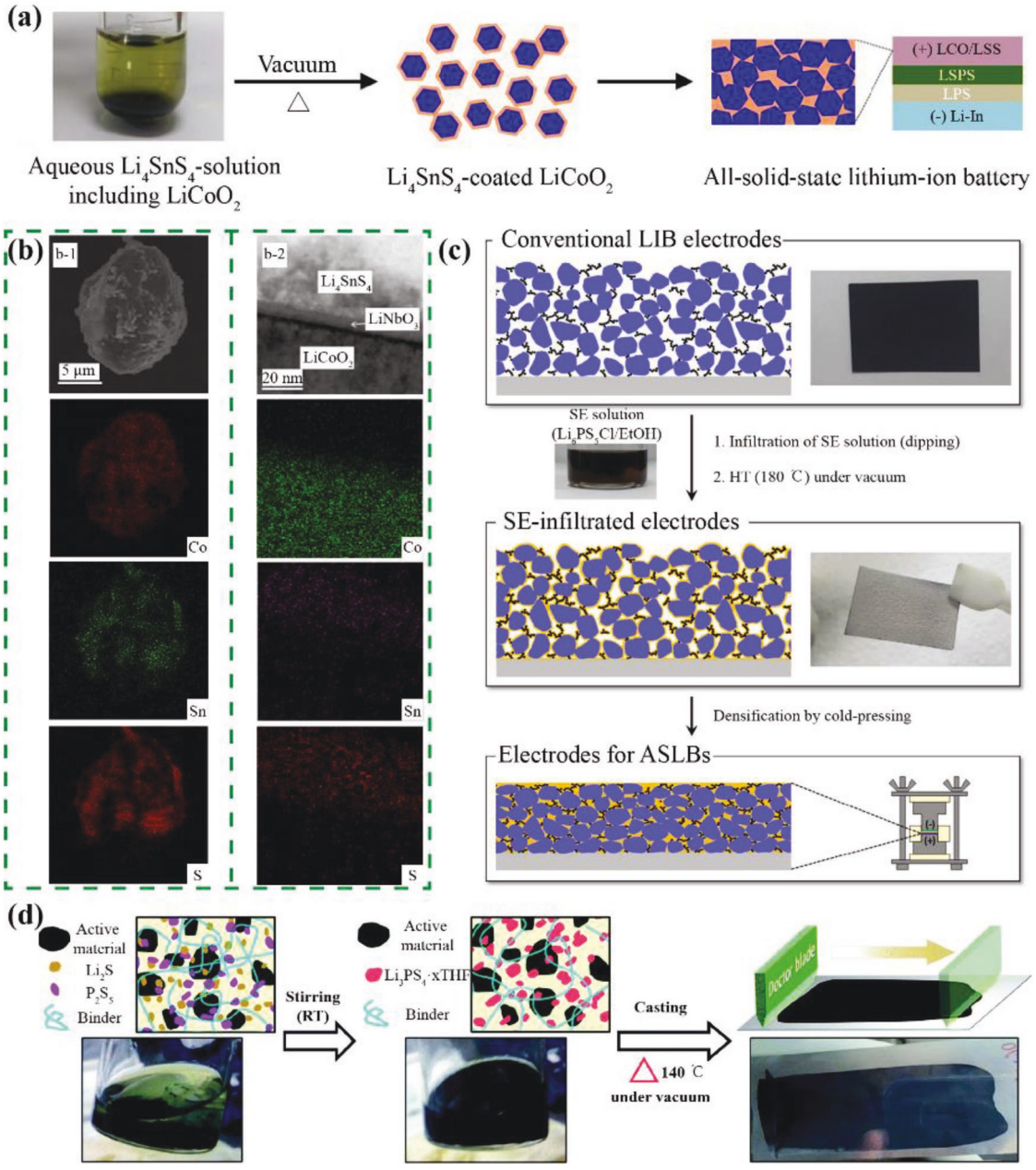

Figure 14. a) Schematic illustration of the aqueous-solution process for Li_4SnS_4-coated LCO for ASSBs. b) Electron microscopy images of Li_4SnS_4-coated LCO particles obtained by the aqueous-solution process. b-1) FESEM image of a Li_4SnS_4-coated LCO particle and its corresponding EDX elemental maps. b-2) HRTEM image of an FIB-cross-sectioned Li_4SnS_4-coated LCO particle and its corresponding EDX elemental maps. a,b) Reproduced with permission.[114] Copyright 2017, Wiley-VCH. c) Schematic diagram illustrating the infiltration of conventional LIB composite electrodes with solution-processable SSEs. The photographs in the panels show the LCO electrodes before and after the infiltration of EtOH-solution processed Li_6PS_5Cl. A photograph of Li_6PS_5Cl-dissolved EtOH solution is also shown. Polymeric binders (PVDF) are not shown in the diagram for simplicity. Reproduced with permission.[109] Copyright 2017, American Chemical Society. d) Schematic diagram illustrating the single-step wet-fabrication of sheet-type composite electrodes. Photographs of the one-pot slurry and the as-fabricated electrode in each step are shown. Conductive additives (super C65) are not shown in the scheme. Reproduced with permission.[167] Copyright 2017, Royal Society of Chemistry.

the formation of intimate ionic contacts in the electrodes. The SSE infiltrated in LCO and Gr electrodes have shown higher reversible capacities than their dry-mixed counterparts.[109]

Inspired by Liu et al.'s study, Oh et al. investigated a tape-casting method to prepare thin-film electrodes using NCM622 and β-Li_3PS_4 solid electrolyte using Li_2S and P_2S_5 as starting materials.[22,167] THF was used as solvent, while nitrile-butadiene rubber (NBR) and polyvinyl chloride (PVC) were tested as polymeric binder. The tape-casting process is illustrated in Figure 14d. While PVC is usually thermally

stable up to 240 °C, the PVC processed using THF started to decompose above 80 °C. The decomposition generated HCl, witnessed by the color change of the β-Li_3PS_4/PVC powder after heat-treatment at 140 °C. The pristine β-Li_3PS_4 solid electrolyte had a conductivity of 2.0×10^{-4} S cm^{-1} at room temperature. However, due to the ionic insulating nature of NBR (5.5 wt%), the β-Li_3PS_4/NBR had a reduced ionic conductivity of 1.0×10^{-4} S cm^{-1}, which was still feasible for the ASSBs to operate.[167] Other polymeric binders such as poly(ethylene-*co*-propylene-*co*-5-methylene-2-norbornene) (PEP-MNB), styrene-ebutadiene-based polymer (SEBS), NBR, and silicone were also used in scalable tape-casting method of sulfide-containing composite electrode, the results of which will be discussed further in Section 6.[168–172]

5.2. Preparation of Electrolytes

Most of the current research on ASSBs use pellet-like solid electrolytes with a thickness of 500–1000 µm and a mass loading of 70–150 mg. These thick SSE layers have high cell resistance cell mass, which leads to low energy density. Because of these issues and the fact that pelletizing SSEs is not a scalable process, alternative methods and configurations have been investigated.

As discussed earlier, Zhao et al. fabricated flexible PEO–LiTFSI–LGPS and PEO–LiTFSI–SN–LGPS composite membranes by dissolving the components in ACN and casting onto Teflon substrate. The resulting membrane had a thickness between 150 and 200 µm, which is much thinner than dry-pressed pellet SSEs. However, as the membrane was composed mostly of polymer, the room temperature ion conduction (10^{-4}–10^{-5} S cm^{-1}) was worse than most of the sulfide materials introduced in this paper.[20,97]

Nam et al. reported a thin and bendable sulfide SSE (Li_3PS_4 and LGPS) film reinforced by a mechanically flexible PPTA NW scaffold (Figure 7b). The SSE thin film, Li_3PS_4–NW–Li_3PS_4 (≈70 µm in thickness), exhibited an ionic conductivity of 2×10^{-4} S cm^{-1} at 30 °C. Comparably, the LGPS–NW–LGPS thin film (≈90 µm in thickness) exhibited an ionic conductivity of 3.4×10^{-3} S cm^{-1}. The NW-reinforced thin films enabled the fabrication of free-standing and stackable ASSBs using heat-treated LCO and Ni-coated NW (as a flexible current collector). Using these strategies, the authors reported a cell energy density increase by a factor of three (to 44 Wh kg_{cell}^{-1}) compared to the conventional ASSBs without the NW scaffold (15 Wh kg_{cell}^{-1}).[96]

5.3. Performance of All-Solid-State Li-Ion Batteries (ASSLBs) Using Lithium-Rich Oxides Cathodes

A laboratory-scale bulk type ASSLB typically contains a triple-layer pellet formed by pressing a cathode composite layer, a SSE layer, and an anode (metal or composite) layer. A schematic description of a lab-scale ASSLB is shown in **Figure 15**a. Usually the cathode and anode composite contain some of the sulfide SSEs to enhance ionic conductivity. Particularly, we want to point out that the SSE layer is highly densified to achieve good ion conduction and the whole ASSLB needs to be compressed to maintain intimate contact, which remains a challenge for scaling up. **Table 4** summarizes the research progress made on sulfide-based ASSLBs with lithium-rich oxide cathode materials.

Ohto et al. reported bulk type ASSLBs using LCO as cathode and Gr as anode. $75Li_2S{\cdot}25P_2S_5$ glass and $70Li_2S{\cdot}30P_2S_5$ glass ceramic ($Li_7P_3S_{11}$) were used as a solid electrolyte. Prior to mixing the cathode composite, LCO particles were coated with LNO to reduce interfacial resistance between the LCO and SSE particles.[143] Rate capability experiments showed that the cell using $70Li_2S{\cdot}30P_2S_5$ glass ceramic was superior to that using $75Li_2S{\cdot}25P_2S_5$ glass. The latter correlates well with ionic conductivity values as the $70Li_2S{\cdot}30P_2S_5$ glass ceramic has higher ionic conductivity at room temperature than $75Li_2S{\cdot}25P_2S_5$ glass (1.5×10^{-3} vs 5.0×10^{-4} S cm^{-1}). However, due to structural degradation at the interface between the $70Li_2S{\cdot}30P_2S_5$ and LCO, the cell cycling performance (after 100 cycles, 42% capacity retention) was not as good as the cell made with $75Li_2S{\cdot}25P_2S_5$ glass (capacity retention after 100 cycles 65%).[39] Kim et al. assembled LCO–Gr ASSLB using conventional tape-cast electrodes infiltrated with Li_6PS_5Cl solid electrolyte. As shown in Figure 15b, this cell exhibited a reversible capacity of 117 mAh g_{LCO}^{-1} at 0.1 C at 30 °C; and good rate capability up to 1 C. For both LCO and Gr electrodes, decreasing the amount of PVDF in the electrodes enhanced the rate capabilities. It is worth noting that the authors deposited Al_2O_3 using atomic layer deposition (ALD) onto the electrodes before SSE infiltration to avoid the reactivity between LCO and SSE. The authors also assembled LCO-Gr ASSLB with SSE-NW (≈70 µm) composite film, and the ASSLB exhibited 94 mAh g_{LCO}^{-1} at 0.1 C at 30 °C.[96,109]

Chen and Zhao et al. used a PEO–LGPS composite electrolyte in combination with $LiFePO_4$(LFP) cathode and Li metal anode. These groups added 10% SN as a plasticizer to the PEO–LiTFSI- 1%LGPS composite, which increased the amorphous content. This lowered the T_g and led to higher ionic conductivity at room temperature. The LFP/PEO–LiTFSI–1%LGPS–10%SN/Li ASSLBs demonstrated high specific capacity of 158 mAh g^{-1} at 0.1 C at 40 °C. After 60 cycles, the capacity was 152 mAh g^{-1}, which equals 94.7% capacity retention. Additionally, at 40 °C, the ASSLB demonstrated good rate capability, with a 1 C discharge capacity of 86 mAh g^{-1} (Figure 15c).[20,97]

Recently, Li_3PS_4 electrolyte with NCM cathode materials has been investigated.[112,141,173] Indium metal was used as anode in most of these reports to avoid the reactivity of Li_3PS_4 with lithium metal. Strauss et al. used NCM622 as a model material and studied the effect of cathode particle size on the capacity of ASSLBs using β-Li_3PS_4. Three samples were compared, NCM-L (mean particle size 15.6 µm), NCM-M (mean particle size 8.3 µm), and NCM-S (mean particle size 4.0 µm). While there was negligible difference in the specific charge capacity in the liquid electrolyte cells, significant changes in specific charge capacity associated with particle size were observed in ASSLBs. Specifically, at C/10 rate, the first charge capacity was 162, 95, and 84 mAh g^{-1} for NCM-L, NCM-M, and NCM-S, respectively (Figure 15d). The ionic conductivity of the cathode was not affected

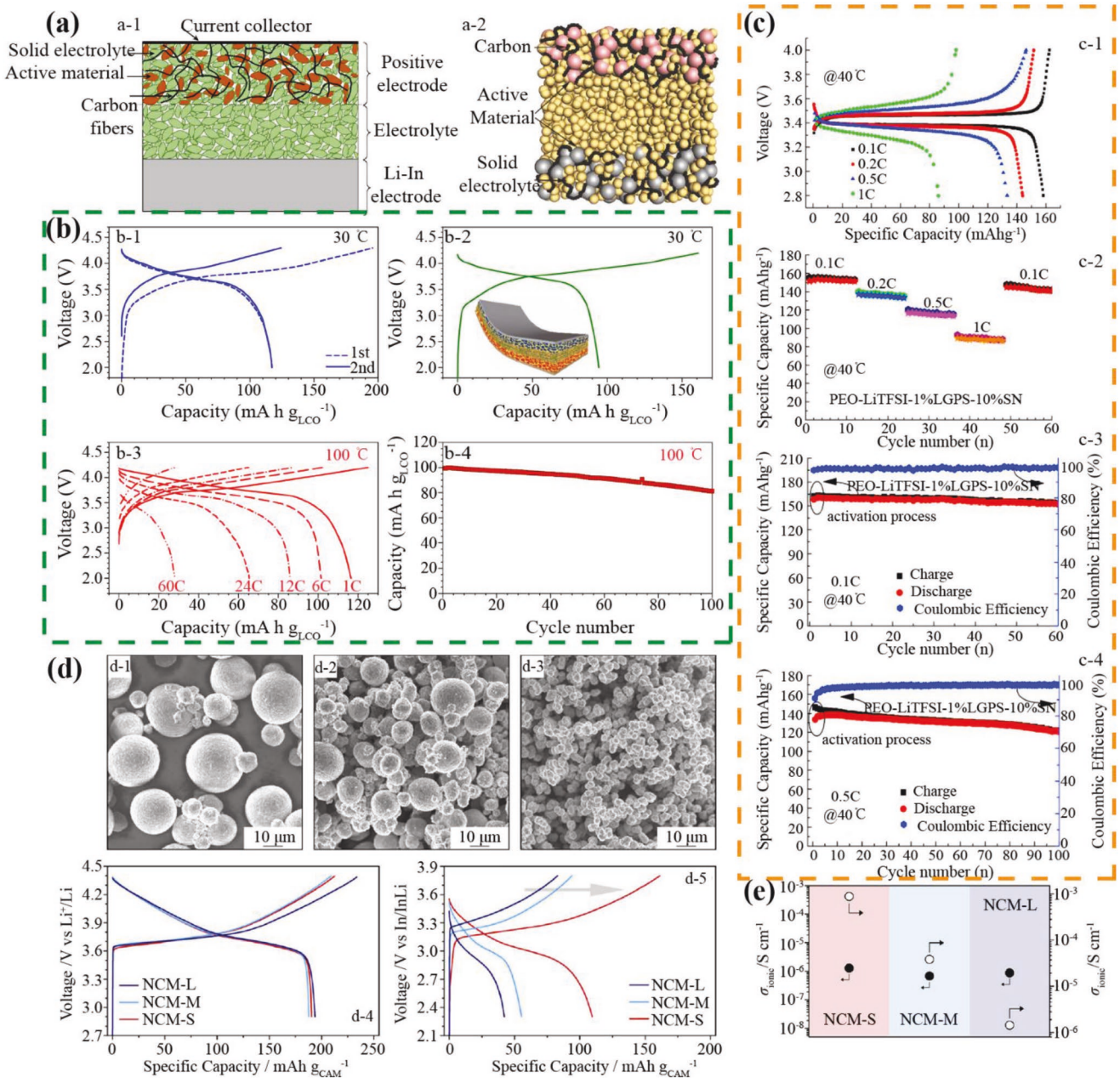

Figure 15. a) Schematic view of a cross section of the all-solid-state half cells (a-1) and full cells (a-2). a-1) Reproduced with permission.[138] Copyright 2017, American Chemical Society. a-2) Reproduced with permission.[174] Copyright 2015, Wiley-VCH. b) Electrochemical performances of LCO/Gr ASSLBs employing L_6PS_5Cl-infiltrated electrodes at 30 and 100 °C. Initial charge–discharge voltage profiles of LCO/Gr ASSLB at 0.1 C (0.14 mA cm^{-2}) and 30 °C using a conventional thick (≈600 µm) SSE layer (2.0–4.3 V) (b-1) and a thin (≈70 µm) SSE–NW composite film (2.0–4.2 V) (b-2). b-3) Charge–discharge voltage profiles at different C rates and b-4) cycling performance at 6 C for LCO/Gr ASSLB at 100 °C (2.0–4.2 V). b) Reproduced with permission.[109] Copyright 2017, American Chemical Society. c) The cycling and rate performance under 40 °C for ASSLB Li/PEO_{18}–LiTFSI–1%LGPS–10%SN/LFP; c-1) the initial charge and discharge curves under different rates (0.1, 0.2, 0.5, 1 C); c-2) the rate cycling performance of the ASSLB; c-3) cycling performance at 0.1 C; c-4) cycling performance at 0.5 C. c) Reproduced with permission.[20] Copyright 2016, Elsevier. d) Top-view SEM images of NCM622 powders of different average particle size. NCM-L, NCM-M, and NCM-S are shown in parts (d-1), (d-2), and (d-3), respectively. Initial charge–discharge curves at C/10 for liquid-electrolyte-based LIB half-cells (d-4) and ASSLB cells (d-5) using the large, medium, and small NCM622. The arrow indicates the increase in specific capacity with decreasing particle size. e) Mean ionic and electronic partial conductivities of ASSB cathode composites using NCM-L, NCM-M, and NCM-S. d,e) Reproduced with permission.[173] Copyright 2018, American Chemical Society.

by the particle size of NCM622. However, the electronic conductivity was greatly dependent on the particle size of active material and it decreased from 10^{-3} to 10^{-6} S cm^{-1} as particle size increased from small to large (Figure 15e). Thus the sluggish electron transport throughout the cathode was the reason for the low usage of active material.[173]

Table 4. Summarizations of performances of sulfide-based ASSLBs.

Cathode formula	Anode formula	SSE	Cell performance	Test conditions	Refs.
LNO-coated LCO/SSE = 70/30	Gr/SSE = 50/50	$70Li_2S{\cdot}30P_2S_5$ glass ceramic	110 mAh g^{-1} at first discharge, with 65% capacity retention after 100 cycles	0.1 C, 60 °C	[39]
LNO-coated LCO/SSE = 70/30	Gr/SSE = 50/50	$75Li_2S{\cdot}25P_2S_5$ glass	90 mAh g^{-1} at first discharge, with 42% capacity retention after 100 cycles	0.1 C, 60 °C	[39]
LNO-coated LCO/LGPS	Li–In	$Li_7Ge_3PS_{12}$	80 mAh g^{-1} at first discharge, with about 55 mAh g^{-1} capacity retention after 10 cycles	7.25 mA g^{-2} at 25 °C	[73]
LCO/SSE/VGCF = 36/54/10	In	Li_6PS_5Cl	30 mAh g^{-1} at first cycle (reversible capacity was 100 mAh g^{-1})	0.05 C at room temperature	[175]
Li_6PS_5Cl -infiltrated LNO-coated LCO (LCO/PVDF/Super P = 97/1/2)	Li_6PS_5Cl -infiltrated Gr (Gr/PVDF = 95/5)	LGPS–Li_3PS_4	117 mAh g^{-1} at first discharge, with 51.4% capacity retention after 80 cycles	0.1 C at 30 °C	[109]
LCO/LGPS = 70/30	LTO/ Li_3PS_4/Super P = 49.8/49.8/0.5	Li_3PS_4–PPTA NW- Li_3PS_4	121 mAh g_{LCO}^{-1} at first discharge	0.1 C at 30 °C	[96]
LFP/Super P/PEO–$LiClO_4$ = 70/20/10)	Li	PEO_{18}–LiTFSI–1% LGPS-10%SN	158 mAh g^{-1} at first discharge with 152 mAh g^{-1} maintained after 60 cycles	0.1 C at 40 °C	[20]
LTO/SSE/VGCF = 40/60/4	Li–In	$70Li_2S{\cdot}29P_2S_5{\cdot}1P_2S_3$	140 mAh g^{-1} at first discharge, with no capacity degradation over 700 cycles	12.7 mA cm^{-2} at 100 °C	[176]
LTO/SSE/carbon fiber = 5/4/1	Li	Li_6PS_5Cl	180 mAh g^{-1} at first discharge, with 154 mAh g^{-1} capacity retention after 250 cycles	0.05 C at 80 °C	[177]
NCM111/SSE/carbon fiber = 38/57/5	Li–In	Li_6PS_5Cl	80 mAh g^{-1} at first cycle, capacity faded to 60mAh g^{-1} after 20 cycles and remained constant for 300 cycles	0.1 C, limited voltage window 2.8–3.4 V vs Li–In	[138]
ZrO_2-coated NCM111/SSE/ acetylene black = 59/39/2	$Li_{4.4}Si$	$75Li_2S{\cdot}25P_2S_5$	120 mAh g^{-1} at first discharge with 115 mAh g^{-1} retained after 50 cycles	0.1 C at room temperature	[150]
NCM622/SSE = 70/30	In	β-Li_3PS_4	162 mAh g^{-1} at first discharge at 0.1 C; 190 mAh g^{-1} at first discharge at 0.03 C	0.1 C or 0.03 C at room temperature	[173]
NCM622/SSE = 70/30	LTO/SSE = 50/50	$Li_{6.6}P_{0.4}Ge_{0.6}S_5I$	89 mAh g^{-1} at first discharge, and stabilized to 99 mAh g^{-1} (no fade after 50 cycles)	0.25 C at 60 °C	[72]
NCM622/SSE/binder/ Super P = 70/25/2.5/2.5	Li	LiI–Li_3PS_4	First discharge capacity was 170 mAh g^{-1} and 126 mAh g^{-1} capacity was maintained after 40 cycles	0.1 C at 55 °C	[169]
NCM811/SSE = 70/30	In	β-Li_3PS_4	124 mAh g^{-1} at first discharge, with 81 mAh g^{-1} maintained after 50 cycles (including higher rate test)	0.1 C at 25 °C	[141]

5.4. Performance of All-Solid-State Batteries Li–S Batteries (ASSLSs) Using Sulfur Cathodes

A laboratory scale ASSLS with S cathodes is usually assembled in the same way as an ASSLB. S or metal sulfides composites are prepared by mixing S or metal sulfides with SSE and conductive additives. **Table 5** summarizes recent progress on the electrochemical performance of ASSLSs using sulfide-based SSEs.

SSEs have been widely used in Li–S batteries to prevent the shuttle effect of lithium polysulfides that occur with liquid electrolytes. There have been a variety of sulfide solid electrolyte materials to be paired with sulfur composite cathode and Li metal anode. In Li–S batteries, cell performance is usually

Table 5. Summarization of electrochemical performances of sulfide-based ASSLSs.

Cathode formula	Anode formula	SSE	Cell performance	Test conditions	Ref
S/graphite/Super P = 40/40/20	Li	$80Li_2S{\cdot}20P_2S_5$ glass	Stable capacity of 400 mAh g^{-1} for over 20 cycles	0.05 C at 80 °C	[155b]
S/carbon fiber/SSE/ionic liquids = 29.9/9.9/60/0.2	$Li_{4.4}Si$	$75Li_2S{\cdot}25P_2S_5$ glass	1270 mAh g^{-1} at initial discharge with 1230 mAh g^{-1} retained after 50 cycles	0.1 mA cm^{-2} at 25 °C	[180]
S/carbon fiber/ SSE = 30/10/60	Li	$75Li_2S{\cdot}25P_2S_5$ glass	1600 mAh g^{-1} at initial discharge with ≈1400 mAh g^{-1} retained after 10 cycles	0.05 C (0.025 mA cm^{-2}) at 25 °C	[131]
S/acetylene black/ SSE = 35/35/30	Li	$80Li_2S{\cdot}20P_2S_5$ glass ceramic	1350 mAh g^{-1} at initial discharge with ≈920 mAh g^{-1} retained after 20 cycles	0.006 C at first and second cycle, and 0.03 C at the third to 20th cycle at 25 °C	[136]
S/acetylene black/ SSE = 25/25/50	Li	$80Li_2S{\cdot}20P_2S_5$ glass ceramic	850 mAh g^{-1} reversible capacity for 200 cycles at 0.2 C and 996 mAh g^{-1} reversible capacity for 200 cycles at 0.1 C	0.2 C (1.3 mA cm^{-2}) or 0.1 C (0.64 mA cm^{-2}) at 25 °C	[188]
S/mesoporous carbon/ SSE = 15/35/50	Li–Al	$Li_{3.25}Ge_{0.25}P_{0.75}S_4$	1864 mAh g^{-1} at initial discharge (with mesoporous carbon participating in discharge) with 500 mAh g^{-1} reversible capacity after 20 cycles	0.013 mA cm^{-2} at 25 °C	[156,181]
S/carbon black/ SSE = 45/15/40	Li	$Li_7P_{2.9}Mn_{0.1}S_{10.7}I_{0.3}$	791 mAh g^{-1} was achieved at first discharge and 800 mAh g^{-1} was maintained after 60 cycles	0.05 C at room temperature	[56]
S/acetylene black/ SSE = 30/10/60	Li	$Li_7P_{2.9}Mn_{10.85}Mo_{0.01}$	1020 mAh g^{-1} was achieved at first discharge and about 500 mAh g^{-1} was maintained after 30 cycles	0.05 C at room temperature	[18]
S/Super P/SSE = 20/10/70	Li–In	Li_6PS_5Br	1355 mAh g^{-1} was achieved at first cycle and about 1080 mAh g^{-1} was maintained after 50 cycles	0.38 mA cm^{-2} (0.1 C) at room temperature	[182]
S-rGO/carbon black/ SSE = 45/15/40	Li	$Li_{9.54}Si_{1.74}P_{1.44}S_{11.7}Cl_{0.3}$	969 mAh g^{-1} was achieved at first cycle and about 827 mAh g^{-1} was maintained after 60 cycles	0.05 C at room temperature	[183]
S/Ketjenblack/ P_2S_5 = 50/10/40	Li–In	Li_3PS_4	1288 mAh g^{-1} at first discharge	0.1 C (0.64 mA cm^{-2}) at room temperature	[184]
CoS_2/Super P/ $Li_7P_3S_{11}$ = 40/10/50	Li	LGPS and $70Li_2S{\cdot}29P_2S_5{\cdot}1P_2O_5$ glass	501 mAh g^{-1} was achieved at first cycle and 427mAh g^{-1} was maintained at 1000th cycle	1.27 mA cm^{-2} at 25 °C	[108]
Li_2S/SSE/Super P = 40/40/20	In	Li_6PS_5Br	628 mAh g^{-1} was achieved at first cycle and about 500 mAh g^{-1} was maintained after 30 cycles	0.064 mA cm^{-2}	[19]
S/Super P/ SSE = 20/40/40	Li–In	Li_6PS_5Cl	1388 mAh g^{-1} was achieved at first cycle and about 389 mAh g^{-1} was maintained after 20 cycles	0.064 mA cm^{-2}	[106]
TiS_2/Super P/LGPS = 48.8/0.4/48.8	Li–In	LGPS and Li_3PS_4	277 mAh g^{-1} reversible capacity	0.2 C at 25 °C	[185]
Li_2S/carbon/ PVC = 65/25/10	Li	β-Li_3PS_4	848 mAh g^{-1} at first discharge with stabilized capacity of 594 mAh g^{-1} after 30 cycles	0.1 C (0.02 mA cm^{-2}) at 60 °C	[187]
MoS_2/acetylene black/ SSE/ = 24/10/66	Li	$Li_7P_3S_{11}$	868 mAh g^{-1} at first discharge with 574 mAh g^{-1} maintained after 60 cycles	0.1 C (0.102 mA cm^{-2}) at room temperature	[186]
SSE coated-MoS_2/acetylene black/SSE/ = 42/5/23	Li–In	Li_6PS_5Cl	520 mAh g^{-1} at first discharge and 374 mAh g^{-1} at second discharge	0.13 mA cm^{-2}	[105]

influenced by the crystallinity of sulfur and particle size of the electrode components (active, conductive, and binder materials). Thus mechanical milling is often employed to achieve intimate contact within the electrode components.[136] Nagao et al. used ball-milling to successfully create amorphized sulfur and reduce the particle size. The cathode composite is typically made with sulfur, carbon, and $80Li_2S{\cdot}20P_2S_5$ glass ceramic electrolyte. ASSLS retained a high capacity of 850 mAh g^{-1} for 200 cycles at 1.3 mA cm^{-2} and 25 °C. The authors also demonstrated that an ASSLS with sulfur electrode can operate over a wide temperature window from –20 to 80 °C.[136] This group has also shown that mechanical milling at 155 °C is more effective at producing amorphized sulfur and reducing the particle size (of sulfur/carbon composite) than milling at room temperature.[178] Yamada et al. fabricated Li–S batteries with ≈1600 mAh g^{-1} capacity (at 25 °C and 80 °C) using a $75Li_2S{\cdot}25P_2S_5$ glass electrolyte. A high Columbic efficiency of 99% over 10 cycles is proof that the polysulfide shuttling effect did not occur. The discharge plateaus typically seen in liquid cells are not observed in solid-state cells and higher temperature operation can accelerate the reactions between Li and S.[131]

Nagata et al. noticed that there is a positive correlation between the phosphorous/sulfur ratio and the reactivity of sulfur in the composite electrode. An electrode using $60Li_2S{\cdot}40P_2S_5$ glass electrolyte demonstrated higher capacity and discharge potential than an electrode using $80Li_2S{\cdot}20P_2S_5$ glass, which is attributed to the higher sulfur activation enabled by phosphorus.[179] Using amorphous Li_3PS_4 electrolyte, Kinoshita et al. studied the additive effect of ionic liquids on the electrochemical performance of the sulfur electrode. They found that the addition of small amounts of ionic liquids can improve the compatibility of the components in the electrode. This increases contact area and, thus, utilization efficiency of sulfur. Among the five imidazolium salts studied, 1-ethyl-3-methyl-imidazolium bis(trifluoromethane-sulfonyl)imide ([EMI][TFSI]), which has the lowest viscosity, demonstrate the best electrochemical property.[180] In order to improve capacity, Nagao et al. deposited a thin Li film (≈1 µm) between the Li anode and $80Li_2S{\cdot}20P_2S_5$ glass ceramic by vacuum-evaporation. This film ensured good contact between the electrode and electrolyte and improve Li platting/stripping. The final bulk-type ASSLSs showed a high initial capacity of 1350 mAh g^{-1} at 0.013 mA cm^{-2} and a third reversible capacity of 945 mAh g^{-1} at 0.064 mA cm^{-2}.[136]

Nagao et al. developed an all-solid-state battery with sulfur-mesoporous (CMK-3) carbon electrode, thio-LISICON ($Li_{3.25}Ge_{0.25}P_{0.75}S_4$), and Li–Al anode. Sulfur was introduced into mesoporous carbon rods and the extra sulfur attached to the surface of the carbon rods were removed through annealing. The sulfur/CMK-3 heat treated at 230 °C demonstrated a first discharge capacity of 3239 mAh g^{-1} at 0.013 mA cm^{-2} with a highly reversible capacity of 1300 mAh g^{-1} after 200 cycles. The extremely high initial capacity, exceeding theoretical capacity of sulfur, is due to the carbon matrix participating in the charge–discharge process.[156] In later experiments, Nagao et al. discovered that smaller carbon matrix pore size is more effective in maximizing the discharge capacity. The structure of the carbon matrix is crucial as the smaller pore size reduces the vacant space in the composite and thicker carbon walls provide a robust framework. They found the optimized pore size and carbon wall thickness in the sulfur/carbon replica mixture were 9 and 5 nm, respectively.[181]

Xu et al. used the $Li_7P_{2.9}Mn_{0.1}S_{10.7}I_{0.3}$ glass ceramic material (room temperature conductivity of 5.6×10^{-3} S cm^{-1}) as electrolyte for bulk type ASSLSs with composite sulfur cathode. They used a conventional liquid Li–S cell with the same anode and cathode for comparison. The ASSLSs and liquid batteries demonstrated initial capacities of 792 and 850 mAh g^{-1}, respectively, at 0.05 C. However, the retained capacity after 60 cycles were 800 mAh g^{-1} for ASSLSs and 627 mAh g^{-1} for the liquid cell. Solid batteries demonstrated better cycling stabilities because of the inhibition of polysulfide shuttling. The ASSLSs also showed good rate performance, 227 mAh g^{-1} at 0.5 C.[56] The same research group also made ASSLS cells with Mo-doped $Li_7P_3S_{11}$ type glass ceramic material, $Li_7P_{2.9}S_{10.86}Mn_{0.1}$ (4.8×10^{-3} S cm^{-1} at room temperature) showing an initial capacity of 1020 mAh g^{-1} 0.05 C. The high capacity was attributed to the high ionic conductivity of the material and the good contact between sulfur, carbon, and SSE obtained after a two-step ball milling process.[18]

Other crystalline thiophosphate materials such as argyrodite Li_6PS_5Br and Cl-doped LGPS material, $Li_{9.54}Si_{1.74}P_{1.44}S_{11.7}Cl_{0.3}$ have also been studied for ASSLSs.[182] Xu et al. constructed an ASSLS with sulfur-reduced graphene oxide (rGO) composite cathode and $Li_{9.54}Si_{1.74}P_{1.44}S_{11.7}Cl_{0.3}$ solid electrolyte. The porous layered rGO (**Figure 16**a) increased the electrode's electron conduction and provided a buffer to accommodate volume change. Sulfur adhered uniformly on the rGO and sulfur, carbon, and SSE distributed uniformly in the composite electrode (Figure 16a). In the S/rGO composite, Figure 16b demonstrates the cycling results of the ASSLSs for the S/rGO. Cycling at 80 mA g^{-1}, the ASSLS with S-rGO/C/SSE electrode showed an initial capacity of 969 mAh g^{-1} with a capacity retention of 85.3% after 60 cycles. By comparison, the S/carbon/SSE electrode without rGO showed an initial discharge capacity of 801 mAh g^{-1} with a capacity retention of only 60.1% after 60 cycles. In addition, the S-rGO/C/SSE electrode demonstrated high rate performance. The cell was able to deliver a capacity of 300 mAh g^{-1} at a current density of 640 mA g^{-1}, which was attributed to the high electronic conductivity of the electrode and high ionic conductivity of the SSE.[183]

A novel electrode containing elemental sulfur, P_2S_5, and carbon black was recently developed by Tanibata et al. Amorphous species P_2S_{5+x} was formed during mechanical milling, where sulfur chains bridge PS_4 units. During lithiation, bridging sulfur reacted with lithium and turned into non-bridging sulfur to form Li_3PS_4 and Li_2S products. At 0.1 C, the specific energy of the electrode was 471 mAh g^{-1}, higher than previously reported ASSLSs.[184]

Sulfide solid electrolytes are also studied in the all-solid-state batteries with metal sulfides composite cathodes, such as Li_2S, CoS_2, MoS_2, and TiS_2.[19,108,185–187] Using argyrodite Li_6PS_5Br electrolyte, Yu et al. studied the effect of nanosizing Li_2S active material during electrode preparation with the aid of NMR, shown in Figure 16c. Exchange NMR was used to quantify the Li ion sites in the electrode and electrolyte and the timescale of ion transfer over the interface. These results showed that Li ion transport over the electrode–electrolyte interface is the

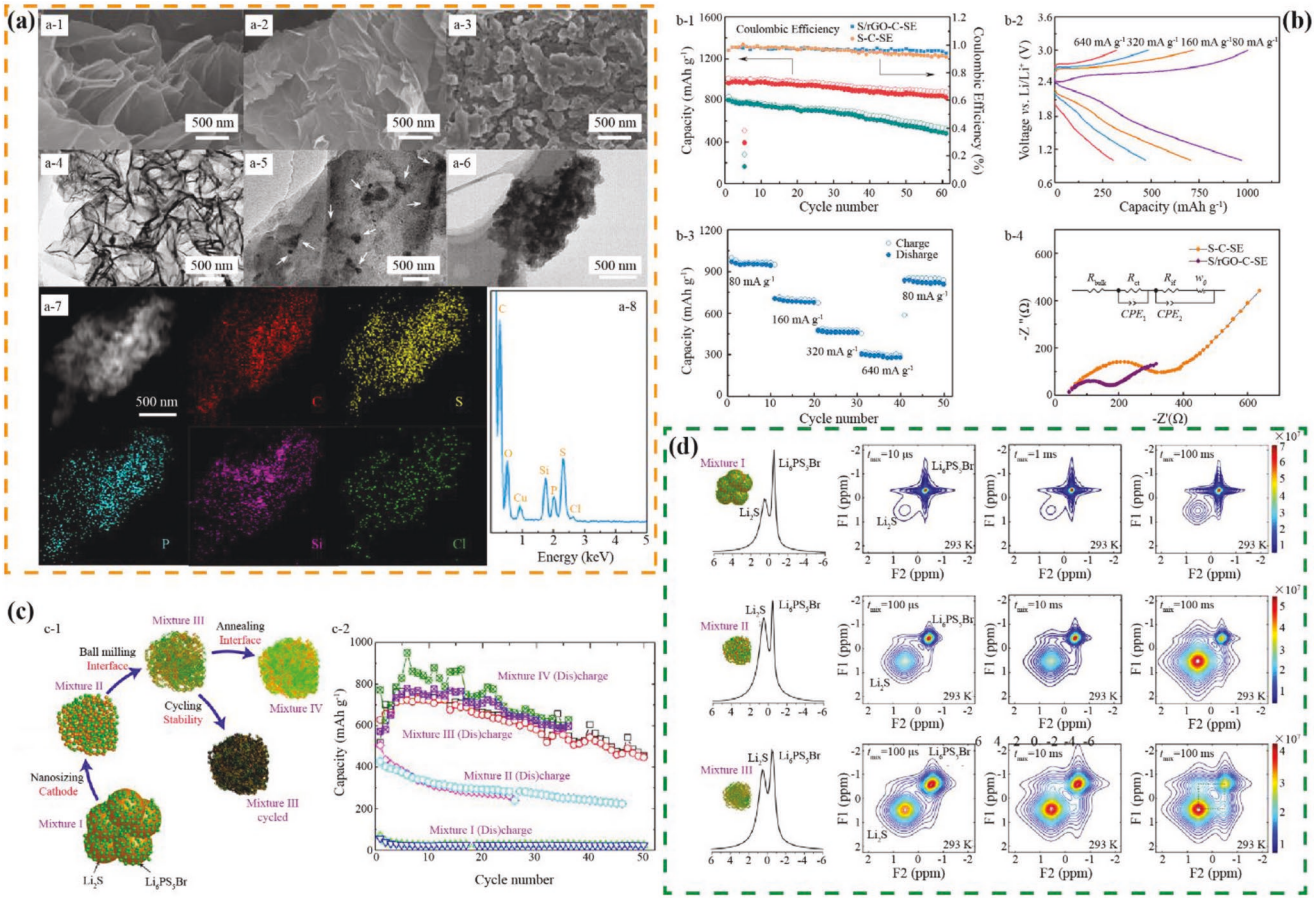

Figure 16. a) SEM images of rGO (a-1), S/rGO (a-2), and S/rGO–C–SSE composite (a-3). TEM images of rGO (a-4), S/rGO (a-5), and S/rGO-C-SSE composite (a-6). a-7) STEM image and elemental mapping of S/rGO–C–SSE composite. a-8) EDS results of the measured area of S/rGO–C–SSE composite. b-1) Cycling performance of S–C–SSE and S/rGO-C-SSE composites at 80 mA g^{-1} and corresponding Coulombic efficiencies at 298 K. b-2) Charge/discharge voltage profiles of S/rGO–C–SSE composite electrode at different current densities. b-3) Rate capabilities of S/rGO–C–SSE composite. b-4) Nyquist plots of ASSLS with S–C–SSE and S/rGO-C–SSE composites at 298 K. The equivalent circuit is inserted. a,b) Reproduced with permission.[183] Copyright 2017, Wiley-VCH. c-1) Schematic representation of the different stages in solid-state battery cathode preparation and the solid-state battery capacity retention. The different stages in cathode preparation and cycling for which the lithium-ion transport over the Li_2S–Li_6PS_5Br interfaces, the charge transfer reaction is measured by ^{7}Li exchange NMR and EIS. c-2) The charge/discharge capacity upon cycling of the solid-state Li–S cell using microsized Li_2S (mixture I), nano-Li_2S (mixture II), mixed nano-Li_2S (mixture III), and annealed mixed nano-Li_2S (mixture IV) as the active material. The charge/discharge current density was set at 0.064 mA cm^{-2} (5.03×10^{-5} A), and the lower and upper voltage cutoff were set to 0 and 3.5 V versus In. d) NMR results of the SSE-active material interfaces. c,d) Reproduced under the terms of the CC-BY Creative Commons Attribution 4.0 International license (http://creativecommons.org/licenses/by/4.0/).[19] Copyright 2017, The Authors, published by Springer Nature Publishing AG.

major resistance for Li ion to transfer through the whole battery (Figure 16d).[19] Nanosizing the active material can increase the contact area between the electrode and electrolyte and reduce the interfacial resistance for ion transfer.[19] Yao et al. coated CoS_2 material with $Li_7P_3S_{11}$ solid electrolyte via an in situ liquid approach. The anchored $Li_7P_3S_{11}$ particle size was ≈10 nm, which is favorable to achieve a good contact between the electrolyte and active materials. The ASSLS made with CoS_2 composite cathode, LGPS/glass solid electrolyte and Li metal anode displayed a reversible capacity of 421 mAh g^{-1} at a current of 1.27 mA cm^{-2} after 1000 cycles.[108] Oh et al. employed TiS_2 nanosheets (TiS_2–NS) as active material, and LGPS electrolyte to make ASSLS cells. The reversible capacity of the latter ASSLS was 277 mAh g^{-1} at 0.2 C, which is higher than the reversible capacity of liquid cells, 240 mAh g^{-1}. The higher capacity is due to the participation of LGPS SSE in the reversible lithiation and delithiation process. Giving the unique 2D morphology and high electronic conductivity of TiS_2–NS, the rate performance of the TiS_2–NS ASSLS is superior—173 mAh g^{-1} at 4 C.[185]

5.5. Performance of All-Solid-State Batteries Using Organic Cathodes

Because of their sustainability and abundancy, organic materials as electrochemically active materials are promising for sustainable battery technology.[189] Inspired by the high solubility of organic electrode materials in liquid electrolytes which results in capacity loss, Luo et al. utilized two azo compounds, azobenzene (AB) and 4-(phenylazo) benzoic acid lithium salt (PBALS), which are soluble in OLEs, in ASSBs with Li_3PS_4 glass as the solid electrolyte. The molecular structures of AB

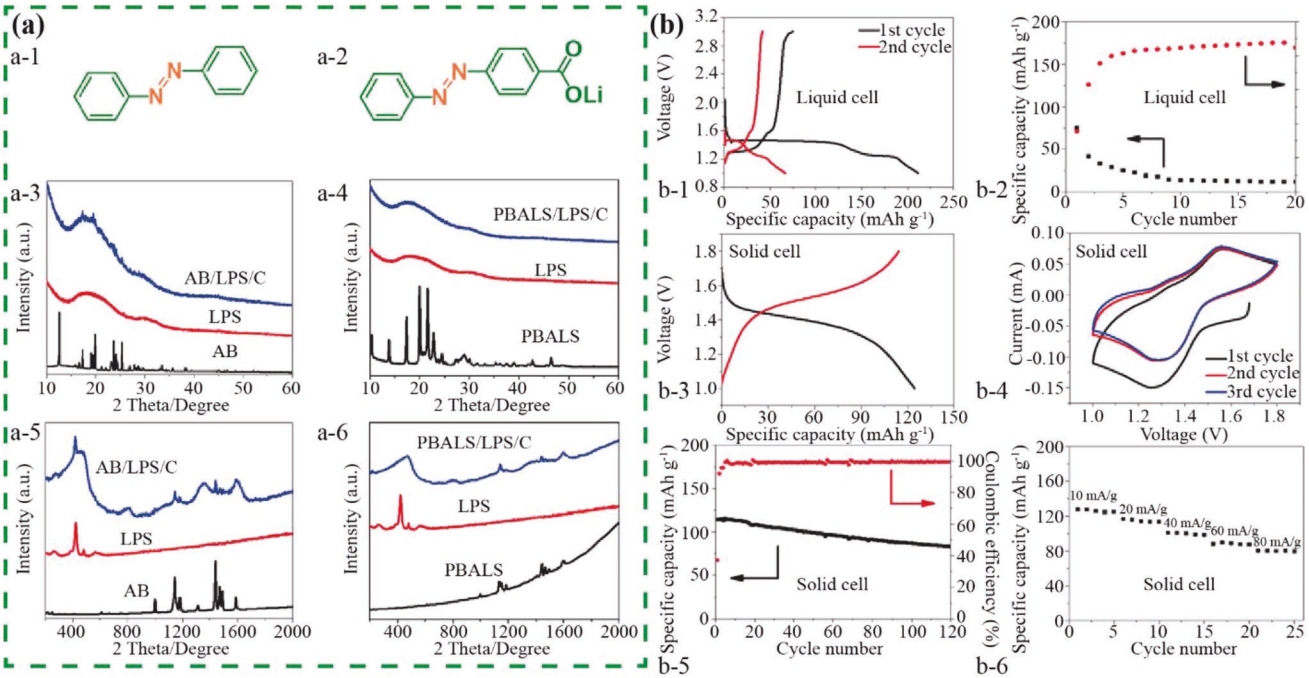

Figure 17. a) Molecular structure of AB (a-1) and PBALS (a-2); a-3) XRD patterns for AB, Li_3PS_4, and AB/Li_3PS_4/C. a-4) XRD patterns for PBALS, Li_3PS_4, PBALS/Li_3PS_4/C. a-5) Raman spectra for AB, Li_3PS_4, and AB/ Li_3PS_4/C. a-6) Raman spectra for PBALS, Li_3PS_4, PBALS/Li_3PS_4/C. b) Electrochemical performance of PBALS in lithium battery. b-1) The galvanostatic charge/discharge curves of PBALS in OLE. b-2) Delithiation capacity and Coulombic efficiency of PBALS during charge/discharge cycles at 20 mA g^{-1} in organic liquid electrolyte. b-3) The galvanostatic charge/discharge curves in SSE. b-4) Cyclic voltammograms of PBALS at 0.1 mV s^{-1} in SSE. b-5) Delithiation capacity and Coulombic efficiency of PBALS during charge/discharge cycles at 20 mA g^{-1} in SSE. b-6) Rate performance of PBALS at various current density in SSE. a,b) Reproduced with permission.[190] Copyright 2018, Wiley-VCH.

and PBALS are shown in **Figure 17**a. Confirmed by XPS, both AN and PBALS were compatible with Li_3PS_4 glass electrolyte. However, PBALS, with a carbonxylate group, can form ionic bonding with lithium ions in the Li_3PS_4, which can accommodate volume change and maintain good interfacial contact between the electrode and electrolyte during cycling. This was witnessed by the XRD and Raman spectra of AB/ Li_3PS_4/C and PBALS/ Li_3PS_4/C composites shown in Figure 17a. In the XRD, the crystalline peaks of AB were maintained after mixing with Li_3PS_4, but the PBALS/ Li_3PS_4/C composite was completely amorphous. In the Raman, the characteristic peaks of the azo groups and Li_3PS_4 were both maintained in AB/ Li_3PS_4/C, but the characteristic peak of Li_3PS_4 disappeared in PBALS/ Li_3PS_4/C composite. Both graphs indicate that strong interactions took place between PBALS and Li_3PS_4 electrolyte. The cycling data of PBALS in liquid and solid cells are shown in Figure 17b. In the liquid cell with PBALS active material, the initial charge capacity was 75 mAh g^{-1} at a current rate of 20 mA g^{-1}, which decreased to 12 mAh g^{-1} after 20 cycles. The fast capacity fading along with the low Coulombic efficiency suggested existence of shuttle reaction. In sharp comparison, the initial capacity of the ASSB made with PBALS active material can reach 120 mAh g^{-1} at the same current rate. The Coulombic efficiency was relatively low at the initial cycle because of the decomposition of Li_3PS_4, but it quickly increased to 99%. Thus, the ASSB with PBALS as the electrode and Li_3PS_4 as the solid electrolyte achieved superior cycling stability compared to the battery with liquid electrolyte.[190] Therefore, by using sulfide SSE the dissolution of organic compound was prevented and the method was more effective than previous approaches to address the dissolution issue of organic compounds.[191]

5.6. Single-Material ASSBs

The concept of single-material ASSBs was introduced by Han et al. using LGPS as a model material, based on the fact that LGPS has a limited electrochemical stability window and can be reduced at 1.7 V and oxidized at 2.1 V.[117,174] As reported previously, the reduction of LGPS can form Li_2S, P and Li–Ge alloy, and the oxidation of LPS can produce S and P_2S_5.[117] When LGPS is mixed with carbon, LGPS can potentially act as both cathode and anode materials. Han et al. used CV and XPS technique to examine LGPS/C cathode and LGPS/C anode and found that the lithiation behavior was due to the Li–S component in LGPS and delithiation was due to the Ge–S component in LGPS. A schematic representation of this type of cell is depicted in **Figure 18**a. When testing against Li, LGPS cathode exhibited reversible capacities of 267, 140, 80 mAh $g_{(LGPS)}^{-1}$ at the current densities of 10, 50, 100 mA g^{-1}, respectively. The LGPS anode achieved 130, 60, and 36 mAh $g_{(LGPS)}^{-1}$ at the current densities of 10, 50, 100 mA g^{-1}, respectively. A single-LGPS battery was able to deliver a reversible capacity of 104 mAh $g_{(LGPS)}^{-1}$ at a current density of 10 mA g^{-1} between 0.0 and 2.5 V. These cycling results are shown in Figure 18b. This work was the first time that a single-material concept was reported for a rechargeable

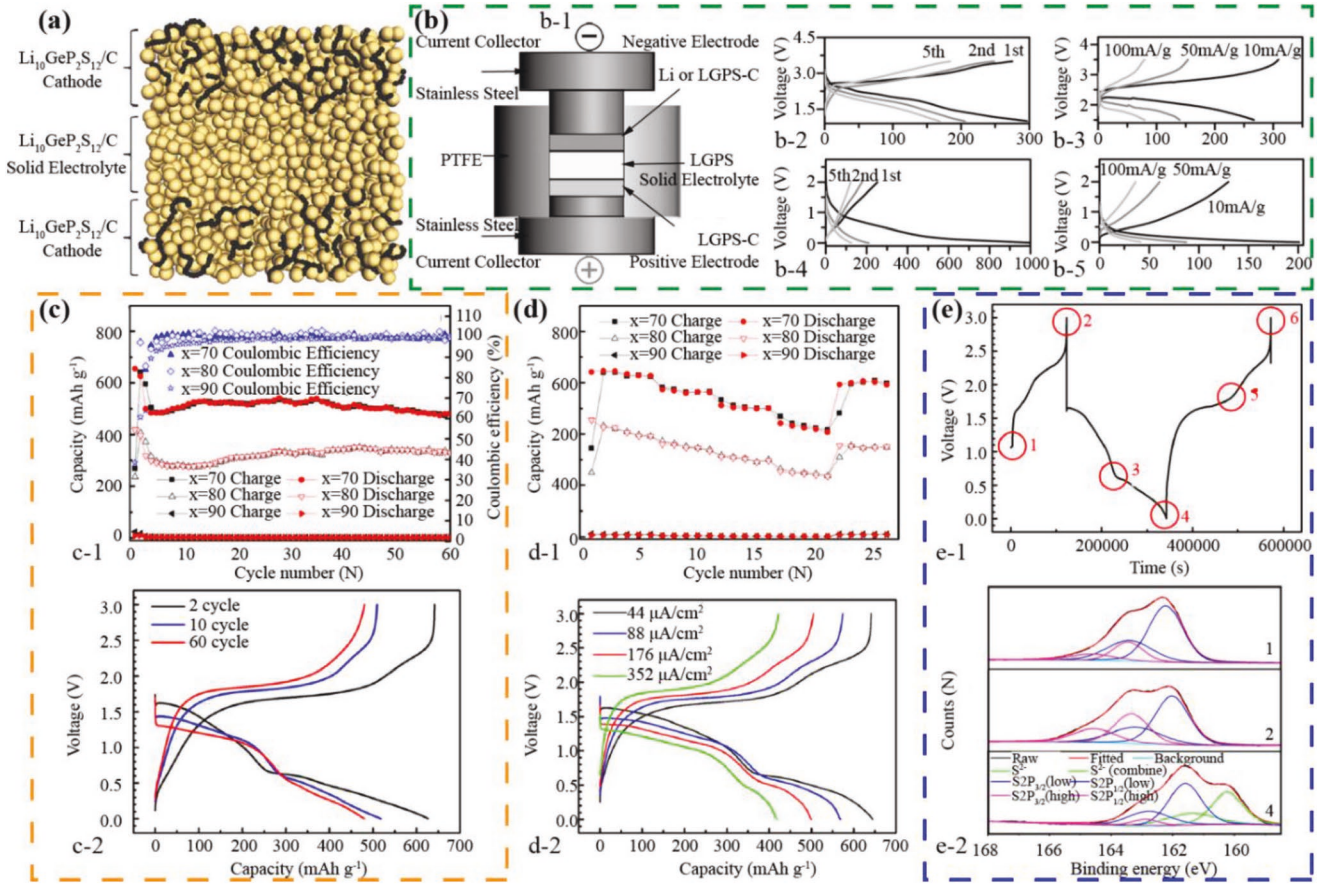

Figure 18. a) Schematic diagrams of a single-LGPS ASSB. b) Electrochemical performance of LGPS cathode and anode with LGPS solid electrolyte. b-1) Schematic representation of the cell configuration for ASSB test. b-2,b-3) Charge/discharge curves of the Li/LGPS/LGPS–C ASSB at a current density of 10 mA g^{-1} in the voltage range of 1.5–3.5 (b-2) and 0.0–2.0 V (b-3). b-4,b-5) Charge/discharge curve of the Li/LGPS/LGPS–C ASSB at different current densities in the voltage range of 1.5–3.5 (b-4) and 0.0–2.0 V (b-5). a,b) Reproduced with permission.[174] Copyright 2015, Wiley-VCH. c) Cycling performance of *x* wt% $78Li_2S{\cdot}22P_2S_5$ glass ceramic–(100 − *x*) wt%MC(conductive additive)|$78Li_2S{\cdot}22P_2S_5$ glass ceramic |Li–In all-solid-state cells. c-1) Charge, discharge capacity, and Coulombic efficiency as a function of the cycle number at the current of 0.176 mA cm^{-2}. c-2) The corresponding discharge–charge voltage profiles of the cells using 70 wt% $78Li_2S{\cdot}22P_2S_5$ glass ceramic –30 wt% MC as the electrodes at 2nd, 10th, and 60th cycles. d) Rate performance of *x* wt% $78Li_2S{\cdot}22P_2S_5$ glass ceramic –(100 − *x*) wt% MC|$78Li_2S{\cdot}22P_2S_5$ glass ceramic |Li–In all-solid-state cells. d-1) Charge and discharge capacity under different cyclic currents (i.e., 0.044, 0.088, 0.176, 0.352, and 0.044 mA cm^{-2} as a function of the cycle number. d-2) The corresponding discharge–charge voltage profiles at different currents of the cells using 70 wt%$78Li_2S{\cdot}22P_2S_5$ glass ceramic–30 wt% MC as the electrodes. e-1) The discharge–charge voltage profiles of the cells using 70 wt% $78Li_2S{\cdot}22P_2S_5$ glass ceramic –30 wt% MC as the electrodes for the first two cycles. The deconvoluted S 2p core XPS spectra of the composite cathodes at the states: e-2) 1 at the fresh state, e-3) 2 first fully charged (to 3.0 V), and e-4) four first fully discharged (to 0.0 V). c–e) Reproduced with permission.[192] Copyright 2018, American Chemical Society.

battery. By making the battery with a single material, the interfacial behavior is improved, as the physical contact between the electrode and electrolyte is more intimate and chemical reactions on the electrode–electrolyte interface are reduced. More importantly, the space-charge layer at the electrode–electrolyte is eliminated, and the transition region at the interface becomes smoother in chemical composition and potential variance.[174]

Similarly, Zhang et al. used $78Li_2S{\cdot}P_2S_5$ glass ceramic as both the active material in the cathode and the solid electrolyte. The $78Li_2S{\cdot}P_2S_5$ based ASSB with 70 wt% $78Li_2S{\cdot}P_2S_5$ in the cathode delivered 655 mAh g^{-1} with a capacity retention of 480 mAh g^{-1} after 60 cycles at a current density of 0.176 mA cm^{-2}. In the high rate cycling test, the capacity fluctuated with a retained capacity of 329 mAh g^{-1} after 60 cycles at a current density of 0.176 mA cm^{-2}, shown in Figure 18c,d. Using XPS analysis (Figure 18e), the authors confirmed that the electrochemical activity of $78Li_2S{\cdot}P_2S_5$ glass ceramic at higher than 0.7 V was attributed to the P—S—P, S—S, and P=S bonds, and reduction and oxidation of Li_2S provides extra capacity below 0.7 V.[192]

6. Challenges and Hurdles—Promising Solutions to Practical Utilization

While most lab-scale ASSBs were tested using binder-free pellets (containing active materials, conductive carbon, and SSEs), pelletized electrodes are difficult to scale up. Scalable processing strategies are necessary for the practical application of sulfide-based ASSBs. There are not many reports on continuous roll-to-roll methods to fabricate ASSBs with sulfide

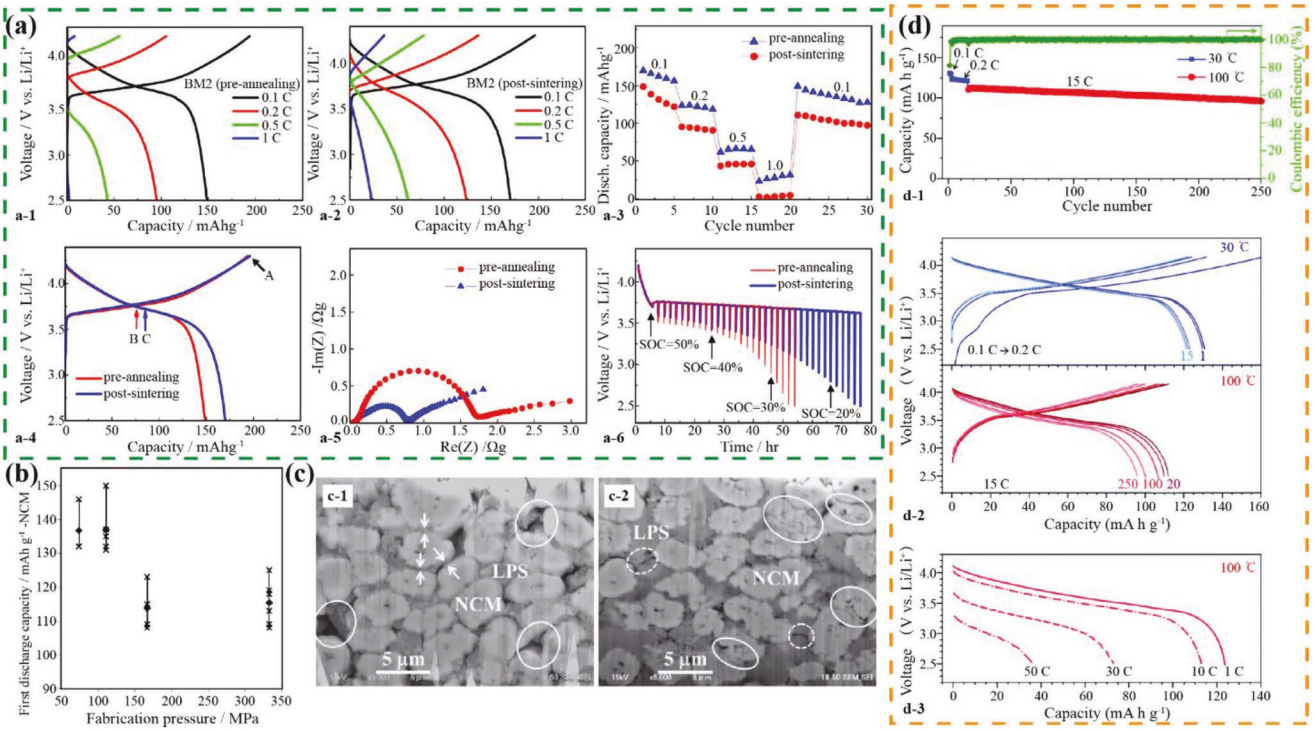

Figure 19. a) Effect of postsintering on the rate performance and impedance characteristic of the slurry-cast NCM622 composite cathode|SSE|Li cells. Comparative plots are presented for rate-dependent charge–discharge profiles for preannealing (a-1) and postsintering (a-2) electrodes; a-3) discharge capacity variations showing the rate capability; a-4) first charge/discharge curves with points of interest for impedance analyses; a-5) EIS spectra at state of charge (SOC) = 100% [point A in (a-4)]; a-6) transient discharge voltage profiles from SOC = 50% [points B and C in (a-4)]. a) Reproduced with permission.[169] Copyright 2018, American Chemical Society. b) Initial discharge capacities of the all-solid-state cells, In/Li_3PS_4/composite electrode sheet (LNO coated-NCM:Li_3PS_4:acetylene black:SEBS = 80:20:2:1 in weight ratio). The composite electrode sheets were pressed at 37 MPa, and the bilayer sheets consisting of the composite electrode sheet and Li_3PS_4 powder were then pressed at 74, 111, 166, and 333 MPa. The cross marks and diamonds indicate the discharge capacity of the individual cell and average discharge capacity, respectively. c) Cross-sectional FIBSEM images of bilayer sheets prepared by pressing the pre-pressed composite electrode sheet (LNO coated- NCM: Li_3PS_4: acetylene black:SEBS = 80:20:2:1 wt%, NCM:Li_3PS_4 = 62:38 vol%) at 37 MPa and Li_3PS_4 powder at 111 MPa (c-1) and 333 MPa (c-2). The circles and arrows in (c-1) indicate voids and Li_3PS_4 sandwiched by NCM, respectively. The circles and dotted circles in (c-2) indicate the noticeable pulverization of NCM and cracking of Li_3PS_4, respectively. b,c) Reproduced with permission.[168] Copyright 2017, The Ceramic Society of Japan. d) Electrochemical performance of a rocking-chair ASSLB at 30°C and 100 °C, employing the NCM622 and graphite electrodes prepared via the single-step wet-chemical route. d-1) Cycle performance with coulombic efficiency, d-2) the corresponding charge–discharge voltage profiles, and d-3) the corresponding discharge voltage profiles at different C-rates for NCM622/Gr ASSLBs. The numbers in indicate the cycle numbers. d) Reproduced with permission.[167] Copyright 2017, Royal Society of Chemistry.

solid electrolytes.[96,109,168,172,193] Wet coating process (i.e., slot-die coating) using small amount of polymeric binders to provide adhesion between particles is a well-established scalable approach in the manufacturing of sheet-type electrodes for LIBs. Different from the slurry process for conventional LIB electrodes, the slurry process for ASSB electrodes involves a homogenization of four components, active material, conductive carbon, polymeric binder, and SSE. The severe reactivity of sulfides with common organic solvents restricts the choices of solvents for the preparation of slurries, and limits the choices for polymeric binders.[110,171] Conventional solvents such as NMP and water are not suitable for sulfides, thus conventional binders such as PVDF and PVA are no longer favorable candidates.

Further, the presence of ion- and electron-insulating polymeric binders can block contact between the active material and SSE, which will lead to poor performances.[170] Because of these reasons, the fabrication of the continuous sheet-type electrodes and sulfide electrolytes for ASSBs present big challenges.

6.1. Fabrication of Sheet-Type Electrodes

Choi et al. studied slurry-cast cathodes consisting of NCM622 active material, LiI-doped Li_3PS_4 SSE, PEP-MNB binder and Super P. Heptane was used as solvent to prepare the slurry. PEP–MNB was chosen as binder because of its high chemical stability against sulfide SSEs, high electrochemical stability against Li metal, and its high thermal stability up to 350 °C. They discovered two main points. First, the SSE powder particle size is important for the utilization of cathode active materials. Reducing the SSE size from ≈5 to ≈1.5 μm led to an increase in initial charge capacity from 159 to 194 mAh g^{-1} at 0.1 C. Second, although the oxidative decomposition of SSEs in contact with active materials is inevitable, the chemomechanical degradation

caused by loss of physical contact between the SSE and the active material can be reduced. This was achieved by annealing the slurry-cast cathodes at 160 °C, enabling a more robust solid–solid interface (**Figure 19**a). At 0.1 C, the initial charge capacity of preannealing and postannealing cathodes were the same. However the discharge capacity and Columbic efficiency of the postannealing cathode were greatly enhanced, indicating a higher usage of active material. In addition, the rate performance of the postannealing cathode was also improved.[169] It is also seen in other reports that sintering can cause closer contact and better ion conduction.[109,172] The improved contact was evidenced by EIS spectra obtained at 100% depth of charge, where the postannealed cell showed lower internal resistance. However, the postannealing approach adapted in this work is restricted to SSEs with relatively low crystallization temperature, considering the thermal stabilities of polymeric binders (Figure 19a).[169]

Yamamoto et al. systematically investigated the fabrication process of sheet-type NCM111 cathodes for ASSLBs with a high ratio of active material (80 wt%). *N*-decane was found to be a suitable solvent to disperse NCM111, Li_3PS_4, acetylene black, and SEBS binder. *N*-decane does not affect ionic conductivity in the cathode. Because of its low vapor pressure, the electrodes showed a dense and smooth surface. Pelletized SSE was used in this study, and it was found that the higher densification of SSE leads to lower resistance. However, the higher densification of the cathode/SSE bilayer sheets leads to lower initial discharge capacities. Figure 19b establishes the relation between cell fabrication pressure and initial discharge capacity. Cells fabricated at 111 and 74 MPa exhibited an average initial discharge capacity of 137 mAh g^{-1} at 64 μA cm^{-2} current density. In contrast, the cells fabricated at 333 and 166 MPa exhibited an average initial discharge capacity of 114 mAh g^{-1} at the same current density. At lower pressure (111 MPa), the particles in the NCM/ Li_3PS_4 composite were loosely packed with void space (Figure 19c). However, when the particles were more densely packed at higher pressure (333 MPa), the NCM111 particles fractured and generated electronically and ionically insulated NCM particles, which lowered the utilization of active material. These results denote the critical optimization of cell processing pressures.[168]

As discussed in Section 5.1.2, Kim et al. infiltrated solution processable argyrodite Li_6PS_5Cl SSE into sheet-type $LiCoO_2$ and graphite electrodes, enabling a favorable contact between SSE and active material with good dispersion of the electrode components. The ASSLBs made using SSE infiltrated in LCO and in graphite electrodes demonstrated a reversible capacity of 117 mAh g_{LCO}^{-1} at 0.1 C (0.14 mA cm^{-2}), which translates to an energy density of 279 Wh kg_{LCO+Gr}^{-1} and 213 Wh $kg_{electrodes}^{-1}$. This work established a new protocol for the scalable fabrication of ASSLBs, however, the approach is only applicable for solution-based SSEs. Due to the low thermal stability of electrode components such as PVDF, the heat-treatment is very limited to low-to-moderate temperature range.[109] The same research group also established a wet chemical process to prepare composite slurries from SSE precursors (Li_2S and P_2S_5), active materials (NCM622 or Gr), and polymeric binders NBR using THF solvent. The NCM622 and graphite electrodes exhibited a high capacity of 140 mAh g^{-1} at 0.1 C and 320 mAh g^{-1} at 0.2 C, respectively. The rate capability of the graphite electrode with solid electrolyte was superior to that of liquid cells, attributed to the good ion percolation. The NCM622/Gr ASSLB showed a reversible capacity of 131 mAh g_{NCM}^{-1} at 0.1 C, translating into an energy density of 241 Wh kg_{NCM+Gr}^{-1} at 30 °C. At 100 °C, the NCM622/Gr ASSLB showed a high capacity of 110 mAh g_{NCM}^{-1} at the high rate of 15 C.[167]

6.2. Fabrication of Flexible Solid Electrolytes and Sheet-Type Batteries

To manufacture prismatic pouch ASSBs, it is crucial to fabricate sheet-type electrolyte and sheet-type electrodes. Nam et al. reported bendable and thin sulfide SSE films reinforced with a mechanically compliant PPTA NW scaffold, allowing the fabrication of freestanding and stackable ASSBs with high energy density. The SSE (Li_3PS_4 or LGPS) were dispersed in toluene, and coated on a Ni foil, and cold pressed onto NW substrate. The freestanding SSE-NW-SSE and NW-SSE-NW films were ≈70 μm thick, and highly bendable (**Figure 20**a) providing opportunities for a roll-to-roll process. As depicted in Figure 20a-1, the freestanding LCO/LTO ASSLB had a total thickness of ≈185 μm. And the composite cathode and anode had 70 wt% LCO and 49.8 wt% LTO, respectively. The cycling performance of the full cells is shown in Figure 20b. The SSE-NW-SSE and NW-SSE-NW cells showed initial discharge capacity of 85 and 75 mAh g_{LCO}^{-1}, respectively. In order to improve capacity, PEO/LiTFSI polymer electrolyte was coated on the NW scaffold. The cell using PEO/LiTFSI coated NW thin film electrolyte showed a first charge capacity of 89 mAh g_{LCO}^{-1} (Figure 20d), translating to an energy density of 44 Wh kg_{cell}^{-1}. As shown in Figure 20a-5, the energy density achieved in this work was still not comparable to that of commercial LIBs and sulfur-based ASSLSs. However, by adopting the bendable thin NW-SSE film, the energy density was approximately three times higher than the pellet type ASSLBs (15 Wh kg_{cell}^{-1}).[96]

Nam et al. comparatively investigated the NCM622 dry-mixed electrodes (without polymeric binders) and sheet-type electrodes fabricated through a tape casting process with polymeric binders. They prepared the electrodes of NCM622/Gr pouch cells by mixing the active materials (NCM622 or Gr), argyrodite Li_6PS_5Cl SSE, NBR binder, and carbon (only for NCM622 electrode) in anhydrous xylene (slurry-mixed electrodes). Dry-mixed electrodes without binders were prepared in parallel. For NCM622/Li–In half cells, higher loading of active material results in poorer solid–solid contact between active material and SSEs. At the same active material loading, the slurry-mixed electrodes underperformed the dry-mixed electrodes due to the disruption of ion percolation by polymeric binders. As shown in Figure 20c, the resistance of the electrode increased directly with the weight fraction of active materials, the mass loading, and the presence of polymeric binders. By analyzing the galvanostatic intermittent titration technique (GITT) measurements, Figure 20d, the polarization data obtained by subtracting closed-circuit voltage (CCV) from quasi-open-circuit voltage (QOCV) agreed with the EIS data. The interfacial coverage of SSE onto active materials was deduced from the GITT. The dry-mixed electrode with the highest content of SSE, D70,

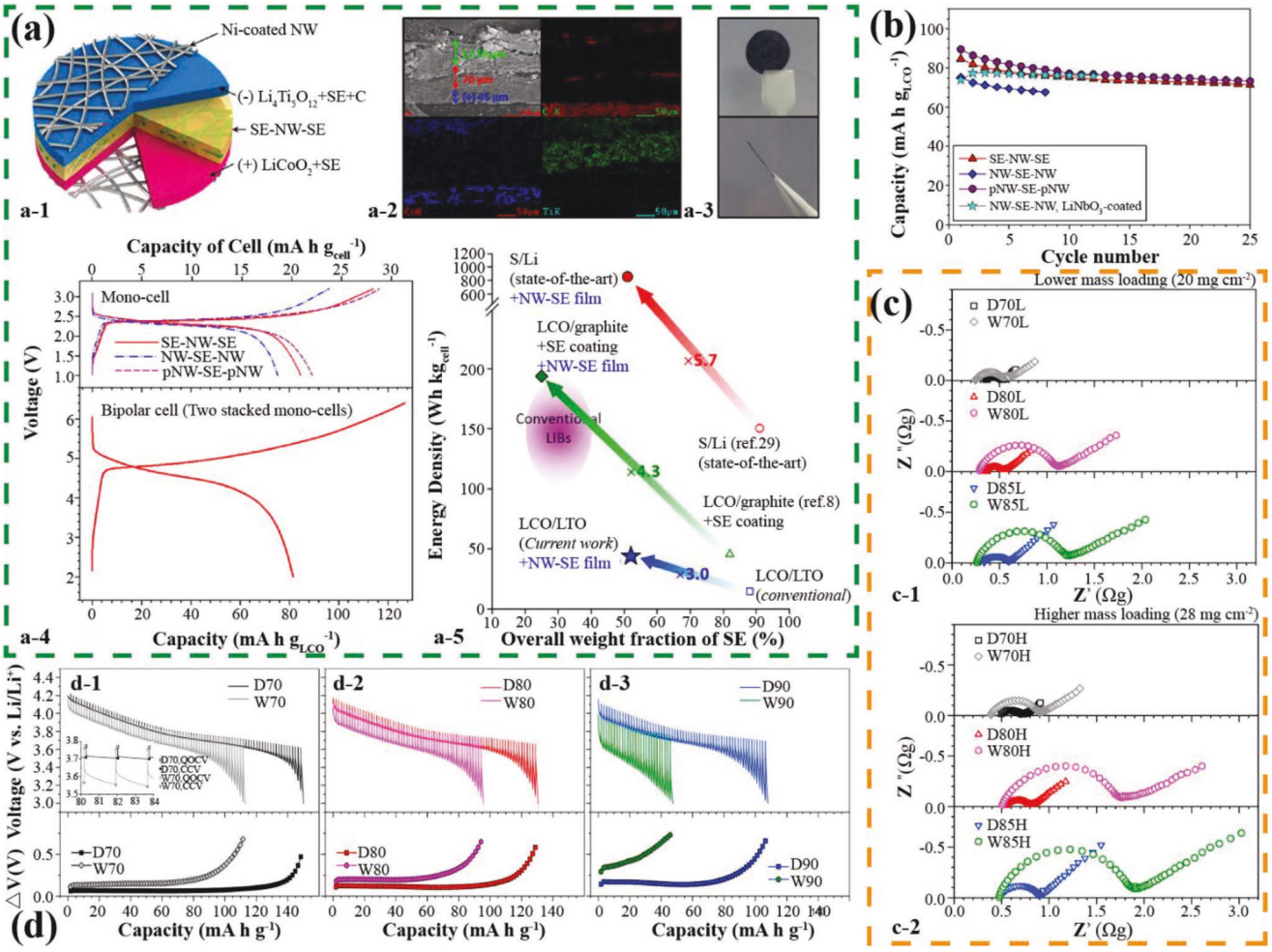

Figure 20. a-1) Schematic diagram, a-2) cross-sectional FESEM image and EDX elemental maps, and a-3) photo images of the free-standing LCO/(SSE-NW-SSE)/LTO all-solid-state cell. a-4) First charge–discharge voltage profiles of the freestanding LCO/LTO all-solid-state monocells with different-structured SE films (SSE–NW–SSE, NW–SSE–NW, pNW–SE–pNW) and the freestanding bipolar cell constructed by stacking two free-standing monocells (LCO/(SSE-NW-SSE)/LTO) at 14 mA g_{LCO}^{-1} (0.11 mA cm^{-2}) at 30 °C. a-5) Comparison of the energy densities of the all-solid-state battery as a function of the overall weight fraction of SSEs varied by electrode chemistry, the presence of SE coating, and the bendable NW-SSE film. b) Cycle performances of the freestanding LCO/LTO all-solid-state cells. The data using 0.35 wt% of LNO-coated LCO with the bendable NW–L_3PS_4–NW film is also represented for comparison. a,b) Reproduced with permission.[96] Copyright 2015, American Chemical Society. c) Nyquist plots at 30 °C for all-solid-state NCM622/Li–In half-cells employing dry-and slurry-mixed electrodes with the lower mass loading (c-1) and the higher mass loading (c-2). d) Transient discharge voltage profiles at 30 °C and their corresponding polarization (ΔV) curves for all-solid-state NCM622/Li–In half-cells employing dry- and slurry-mixed electrodes with ≈70 wt% (d-1), ≈80 wt% (d-2), and ≈85 wt% (d-3) NCM622, obtained by GITT. The enlarged view where QOCV and CCV are indicated is shown in the inset in (d-1). The polarization data were plotted by subtracting CCV from QOCV in the transient voltage profiles in transient discharge voltage profiles. c,d) Reproduced with permission.[170] Copyright 2018, Elsevier.

exhibited the highest coverage of 25.2%, while wet-mixed electrodes exhibited lower coverage. The wet-mixed electrodes with the lowest content of SSE, W85, showed coverage lower than 10%. To achieve a better coverage of SSE onto active material, the SSE and the active material were premixed before the slurry preparation. Negligible reactions occurred between SSE and active material, as shown in the XRD data in **Figure 21**a. In the EDX maps, sulfur signals are more homogeneous in the mixed electrodes compared to the electrodes without mixing. The electrochemical performance was significantly improved due to the favorable ionic contacts limiting polymeric binder blockage (Figure 21a). The first cycle discharge capacity of NCM622/LiIn cell was improved from 92 to 129 mAh g^{-1}. And the cell polarization was reduced through mixing, which was indicated by EIS and GITT data. Further, all-solid-state NCM622/Gr full cells were constructed using slurry-mixed NCM and graphite electrodes. SSE was coated on graphite electrodes directly using a wet slurry process. The pouch cell showed a first discharge capacity of 112 mAh g_{NCM}^{-1} at 0.025 C with stable cycling. This translates to a gravimetric energy density of 182 Wh kg^{-1} based on the total weight of the electrode components (Figure 21b).[170]

More recently, Sakuda et al. demonstrated the fabrication of a sheet-type ASSLB with $LiNi_{1/3}Co_{1/3}Mn_{1/3}$ (NCM111) cathode, graphite anode, and Li_3PS_4 glass electrolyte using a practical slurry coating process.[193] Heptane was used as solvent to

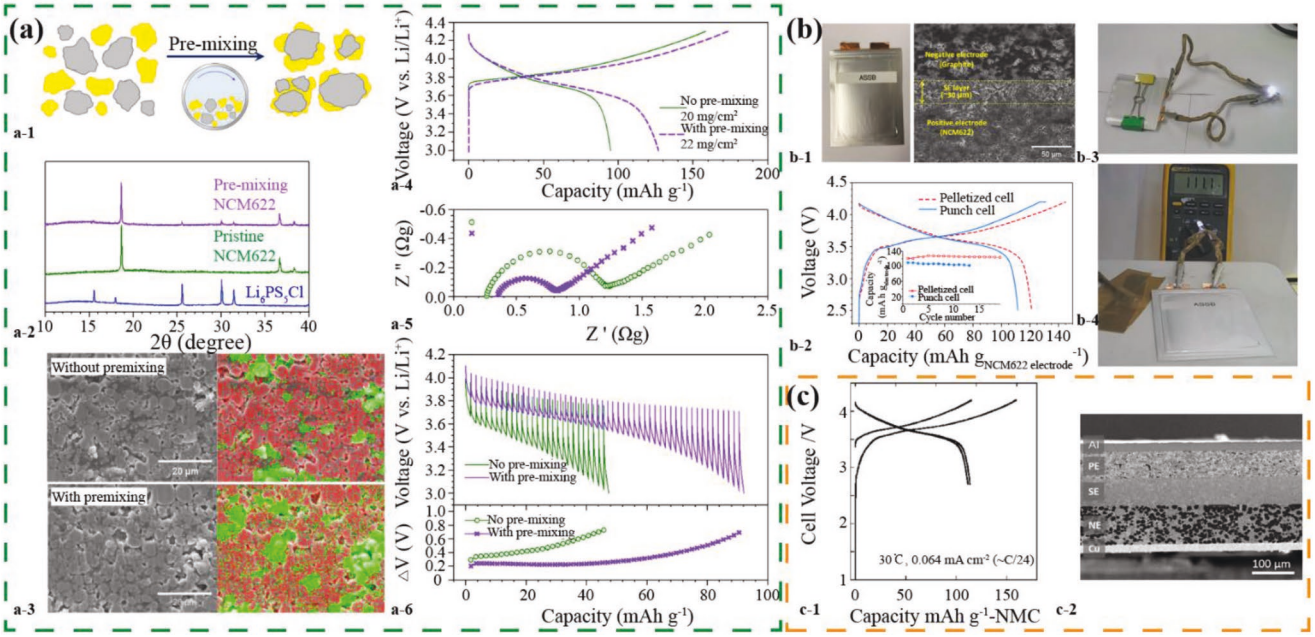

Figure 21. a) Results of NCM622 electrodes fabricated by wet-slurry process using a premixed powder of NCM622 and SSEs. a-1) Schematic diagram of premixing process for NCM622 and SSE powders by mechanical milling. a-2) XRD patterns of Li_6PS_5Cl, pristine NCM622, and NCM622 premixed with Li_6PS_5Cl. a-3) Cross-sectional FESEM images of wet-mixed NCM622 electrodes without and with premixing process and their corresponding EDS elemental maps for Ni (red) and sulfur (green). a-4) First-cycle charge–discharge voltage profiles at 0.1 C, a-5) Nyquist plots, and a-6) transient discharge voltage profiles and their corresponding polarization (ΔV) curves for slurry-mixed NCM622 electrodes without and with premixing process, and their corresponding polarization curves. b) Results of NCM622/Gr ASSBs. b-1) Photograph of 80 × 60 mm^2 pouch-type NCM622/Gr full-cell and its cross-sectional FESEM image. b-2) First-cycle charge–discharge voltage profiles of pelletized and pouch-type full-cells of NCM622/Gr at 0.025 C. The pelletized cell and pouch-cell were tested at 30 °C and 25 °C, respectively. Photographs of 80 × 60 mm^2 pouch-type NCM622/Gr ASSBs after cutting with scissors (b-3) and being placed on the hot plate at 111 °C for >1 h (b-4). a,b) Reproduced with permission.[170] Copyright 2018, Elsevier. c-1) Charge–discharge curves of a sheet-type ASSB. c-2) Cross-sectional SEM image of a sheet-type ASSB cell after 10 cycles. c) Reproduced with permission.[193] Copyright 2017, The Electrochemical Society.

dissolve SEBS binder and anisole was used as dissolve styrene butadiene styrene copolymer (SBS) binder. Based on EIS evaluation, cathode sheets with SEBS in heptane were more ion-resistive than cathodes made with SBS in anisole. However, the mechanical strength of the SEBS cathodes was higher than those made with SBS. Consistent with EIS data, the SEBS and SBS cathodes displayed reversible capacity of 121 and 158 mAh g^{-1} at C/20 rate, respectively. Composite graphite anodes and SSE sheets were made in a similar slurry coating process, with SBS and anisole. The coated SSE sheets containing 3 wt% SBS binder exfoliated from Cu foil after drying and pressing. The sheet-type NCM/Gr ASSB displayed an initial charge and discharge capacity of 159 and 114 mAh g_{NCM}^{-1} respectively (Figure 20c).[193] Excluding the weight of the current collectors and exterior package, the energy density of the sheet-type NCM/Gr ASSLB was estimated to be 155 Wh kg_{cell}^{-1}, which is larger than previously reported energy densities for lab-scale ASSLBs.[96,172,193] Furthermore, SEM images of the battery's cross-section showed heterogeneous distribution of SSE particles and active materials, particularly for the negative Gr electrode. However, due to the limited ionic conductivity of the SSE (4×10^{-4} S cm^{-1} at room temperature) used in this study, the ASSLB had limited rate performance.[193]

We summarized recent processing methods of sulfide-containing thin-film electrodes/electrolytes in **Table 6**. In conclusion, technical challenges in material handling and cell design need to be addressed to advance sulfide-based ASSBs. Regarding scalable roll-to-roll production, the fabrication of layered (sheet-type) batteries will need to be improved to target reducing the thickness of both the electrolyte and the electrode layers. Powder like sulfide SSEs enables the fabrication of slurry-mixed composite electrodes (with the right choice of polymeric binder and organic solvents). It is worth emphasizing that achieving a homogeneous distribution of active materials and SSEs requires careful considerations of the mixing protocols.

7. Summary and Outlook

Herein, the major categories of sulfide SSEs were reviewed in Section 2, including their structures and ion conduction properties. Most sulfide SSEs are derived from the Li–P–S systems. Among these different sulfide materials, the LGPS family has shown the most superior ionic conductivity reported to so far. Being the Si and Cl substituted version of LGPS the ones with ionic conductivities (up to 2.5×10^{-2} S cm^{-1} at room temperature) even higher than conventional liquid electrolytes. Glass ceramics, $Li_7P_3S_{11}$, and argyrodite Li_6PS_5Cl can also reach high ionic conductivities in the 10^{-3} S cm^{-1} range, whereas Li_3PS_4

Table 6. Approaches to prepare sulfide containing thin film electrodes.

SSE	Solvent	Binder	Formulation	Processing	Ref
Li_6PS_5Cl or 0.4LiI–Li_4SnS_4	EtOH or MeOH	PVDF	LCO or Gr (LNO-coated LCO/PVDF/ Super P = 96/2/2)/SSE = 88/12, (Graphite/ PVDF = 95/5)/SSE = 79/21	Dip-coating conventional electrodes in SSE solution and heat treatment	[109]
β-Li_3PS_4	THF	NBR or PVC	NCM622 or graphite (NCM622/SSE/ Super C65/binder = 70/27.5/1/1.5) (Gr/SSE/ Super C65/binder = 50/47.5/0/2.5)	Active materials, SSE precursors (Li2S and P2S5), binders and carbon additives (Super C65) were added to THF. The slurry was cast on current collectors and heat treated	[167]
Li_6PS_5Cl	Xylene	NBR	NCM622 or graphite (NCM622/SSE/ Super P/binder = 68.1/29.2/1.3/1.4) (Gr/SSE/ Super C65/binder = 58.6/39.1/0/2.3)	Active materials, SSE precursors (Li2S and P2S5), binders and carbon additives were mixed in xylene. The slurry was cast on current collectors and heat treated	[170]
Thio-LISICON $Li_{3.25}Ge_{0.25}P_{0.75}S_4$	Heptane	Polysiloxane	Mo_6S_8 (Mo_6S_8/SSE/acetylene black = 70/30/3.5, binder is 5 vol%)	Cathode mixtures were dry mixed and cast on current collectors	[172]
Li_3PS_4 glass	heptane	SEBS or SBS	NCM111 (LNO-coated NCM111/SSE/ acetylene black/binder = 70/30/3/3)	Slurry was prepared by mixing the cathode mixtures in solvent by centrifugal mixer	[193]

and thio-LISICONs are in the order of 10^{-4} S cm^{-1}. The preparation approaches of sulfide-based SSEs were then detailed in Section 3. The most common synthesis method for the glass or crystal sulfides is ball-milling and then annealing when needed. More recently, various wet chemical methods have been developed and gained attention due to the potential advantages toward scale-up fabrication of SSEs. Section 4 featured an analysis of the electrochemical, chemical, and interfacial stabilities of sulfide SSEs when paired with Li metal anode and cathode materials. The discussion included both theoretical calculations and experimental observations. As most sulfides are highly reactive with Li metal and transition metal oxide cathode materials, recent reports on improving the interfacial stabilities of sulfides were discussed. In Section 5, there was an investigation into the different methods used to prepare composite electrodes and electrolytes in ASSBs. The section also included summarized electrochemical performances data. Results of ASSBs with transition metal and sulfur-based cathodes using sulfide SSEs were reviewed using work published in the last 10 years. Lastly, recent reports were reviewed regarding electrode/electrolyte synthesis and cell fabrication methods and its potential for scalable mass production of sulfide-based all solid lithium batteries.

7.1. Advanced Experimental and Computational Approaches

Although the poor air sensitivity of sulfides induces difficulties in sample preparation and transfer, most advanced characterization methods can be applied to obtain structural, morphological, and compositional information of sulfide-based SSEs, interfaces and ASSBs experimentally. It is worth noting that in situ and operando techniques have been employed more recently to investigate the sulfide containing interfaces. Particularly, in Section 4.2, we reviewed in situ and operando XPS,[126] Raman,[119] and XANES[142] techniques used to study the structural and elemental composition of the reaction products with respect to time or potential. A delicate design of experimental setup was essential. In situ XPS coupled with time-resolved EIS offered detailed composition of the products from the chemical reactions at the Li/SSE interface as Li metal was deposited.[126] Operando Raman, in combination with ex situ XPS and SEM, evaluated the potential-dependent changes in the reaction products at the SSE/Cu interface.[119] In situ XANES during initial charge/discharge process, assisted by ex situ XPS, characterized the interfacial reactions between LGPS and LCO cathode materials, and proved the necessity of using a LNO coating layer to suppress the interfacial reactions.[142]

Computational work based on first-principle calculations was used to thermodynamically determine the origin of the instabilities of sulfide SSEs. Electrochemical window and phase equilibria at the reduction and oxidation potentials of the sulfide SSEs were calculated. Most sulfide SSEs have intrinsic narrow windows, and decomposition reactions are thermodynamically favorable. However, the sluggish kinetics of the decomposition reactions results in high overpotential, which is the reason of the wider window observed in experiments.[118] Theoretical work on a core–shell structure electrolyte explained the improved voltage window by volume restriction, and highlighted the advanced structural design of new SSEs.[120] SSE/electrode interfaces were also evaluated and it was shown that stable window of sulfide SSEs have a significant gap with those of oxide electrode materials such as LCO, which is the main reason of the interfacial decomposition.[121] Thermodynamically, the formation of the interfacial phases were predicted, and the theoretical results related well with experimental results.[137] Coating materials such as LNO plays an important role by passivation and stabilization because it can bridge the electrochemical stability gap between LCO and sulfide SSEs.[121]

7.2. Summary of Grand Challenges

Solid-state electrolytes with high ionic conductivities are crucial to enable safer lithium-based batteries coupled with high energy

density cathodes. It remains a grand challenge to an electrolyte with a high ion conduction and long-term chemical and electrochemical stabilities. Understanding the basic mechanisms of ion conductions and reactivities is of great importance for the design of new ion conductors and development of new battery fabrication processes. Herein, we outline the main academic and commercial challenges to produce sulfide based ASSBs.

i) Inert atmosphere for processing and handling—The processing of sulfide compounds requires special consideration because of their high reactivity against moisture. And air exposure deteriorates the ion conduction performance. Strictly controlled inert atmosphere is not only necessary (i.e., high-quality dry room) for maintaining the quality of the product, but also necessary for avoiding the release of toxic H_2S gas.
ii) Electrochemical stability and interface chemical compatibility—Both theoretical and experimental results have shown the narrow intrinsic thermodynamic electrochemical window of sulfide SSEs. Within the critical voltage range of SSEs, interlayers are formed as a result of the chemical reactions between SSE and electrode materials. A stable interface is ion-conductive and electron-insulative, and without further degradation of SSE or electrode material. Forming a desirable interface and controlling the chemical reactions between the electrolyte and the electrode is a critical step for the design of an ASSB.
iii) Fabrication of thin electrolyte and electrode—Although sulfide SSEs are relatively easy to synthesize at room temperature, compared to their oxide counterparts, it remains a challenge to produce the SSE into a thinner form. Bulk-type ASSBs are not practical for large-scale productions and applications as they require high-pressure to function. Tape-casting is a practical technique from the viewpoint of mass production of both for electrolyte and electrode. However, it is still difficult to use this technique to produce sulfide-based SSE and electrodes, considering the high reactivity of sulfide compounds, both selection of solvent and binder and compositional control require great efforts. To date reports on such topics are rare. The main challenge is the selection of solvent and the difficulty of achieving good ion/electron contact during mixing.
iv) Large-scale production—Conventional solid-state reactions such as melt-quenching and ball-milling demand much more time and efforts than wet chemical reactions and arguably not scalable. More SSE-solvent combinations and wet chemistries (leveraging tape casting/slot die coating) have been studied in recent years and are proved to be more controllable and scalable compared to solid-state methods. Unravelling the mechanisms of the wet reaction routes is important for the performance of the materials.

7.3. Outlook on Future Research

Overall, this review provided comprehensive and insightful information on sulfide-based SSEs and sulfide-based ASSB systems, with the hope that our review will be instructive for future battery research. The summary of results presented in this paper should be useful to researchers in improving SSE electrolyte properties and scaling-up its fabrication and find the best methods to produce large format ASSBs towards batteries with higher energy density and increased safety. Further research on the material, electrode, and cell design is necessary to enable simultaneous science and engineering to implement production processes. The next steps are SSE thicknesses reduction (to compete with current LIB separators) and experiments on the fabrication, processing, and handling of electrode and solid electrolyte layers for ASSBs.

Conflict of Interest

The authors declare no conflict of interest.

Keywords

characterization, interfaces, metal sulfides, solid-state batteries, stability, synthesis

Received: February 18, 2019
Revised: June 14, 2019
Published online: August 22, 2019

[1] a) T. Nagaura, K. Tazawa, *Prog. Batt. Sol. Cells* **1990**, *9*, 20; b) M. Armand, J. M. Tarascon, *Nature* **2008**, *451*, 652.
[2] T. Placke, R. Kloepsch, S. Dühnen, M. Winter, *J. Solid State Electrochem.* **2017**, *21*, 1939.
[3] USABC Goals for Advanced High-Performance Batteries for Electric Vehicle (EV) Applications, https://www.uscar.org/guest/article_view.php?articles_id=85, (accessed: July 2019).
[4] a) R. Schmuch, R. Wagner, G. Hörpel, T. Placke, M. Winter, *Nat. Energy* **2018**, *3*, 267; b) D. Andre, S.-J. Kim, P. Lamp, S. F. Lux, F. Maglia, O. Paschos, B. Stiaszny, *J. Mater. Chem. A* **2015**, *3*, 6709.
[5] Q. Li, J. Chen, L. Fan, X. Kong, Y. Lu, *Green Energy Environ.* **2016**, *1*, 18.
[6] K. Xu, *Chem. Rev.* **2004**, *104*, 4303.
[7] T. Inoue, K. Mukai, *ACS Appl. Mater. Interfaces* **2017**, *9*, 1507.
[8] Y. Kato, K. Kawamoto, R. Kanno, M. Hirayama, *Electrochemistry* **2012**, *80*, 749.
[9] C. Li, H. Zhang, L. Otaegui, G. Singh, M. Armand, L. M. Rodriguez-Martinez, *J. Power Sources* **2016**, *326*, 1.
[10] Y. Kato, S. Hori, T. Saito, K. Suzuki, M. Hirayama, A. Mitsui, M. Yonemura, H. Iba, R. Kanno, *Nat. Energy* **2016**, *1*, 16030.
[11] D. J. Noelle, M. Wang, A. V. Le, Y. Shi, Y. Qiao, *Appl. Energy* **2018**, *212*, 796.
[12] F. Croce, A. D'Aprano, C. Nanjundiah, V. R. Koch, C. W. Walker, M. Salomon, *J. Electrochem. Soc.* **1996**, *143*, 154.
[13] K. Hayamizu, Y. Aihara, S. Arai, C. G. Martinez, *J. Phys. Chem. B* **1999**, *103*, 519.
[14] J. B. Bates, N. J. Dudney, G. R. Gruzalski, R. A. Zuhr, A. Choudhury, C. F. Luck, J. D. Robertson, *J. Power Sources* **1993**, *43*, 103.
[15] a) C. Li, Y. Liu, J. He, K. S Brinkman, *J. Alloys Compd.* **2017**, *695*, 3744; b) J.-F. Wu, E.-Y. Chen, Y. Yu, L. Liu, Y. Wu, W. K. Pang, V. K. Peterson, X. Guo, *ACS Appl. Mater. Interfaces* **2017**, *9*, 1542.
[16] N. Kamaya, K. Homma, Y. Yamakawa, M. Hirayama, R. Kanno, M. Yonemura, T. Kamiyama, Y. Kato, S. Hama, K. Kawamoto, A. Mitsui, *Nat. Mater.* **2011**, *10*, 682.
[17] P. Bron, S. Johansson, K. Zick, J. Schmedt auf der Günne, S. Dehnen, B. Roling, *J. Am. Chem. Soc.* **2013**, *135*, 15694.
[18] R.-C. Xu, X.-H. Xia, X.-L. Wang, Y. Xia, J.-P. Tu, *J. Mater. Chem. A* **2017**, *5*, 2829.

[19] C. Yu, S. Ganapathy, E. R. H. v. Eck, H. Wang, S. Basak, Z. Li, M. Wagemaker, *Nat. Commun.* **2017**, *8*, 1086.
[20] B. Chen, Z. Huang, X. Chen, Y. Zhao, Q. Xu, P. Long, S. Chen, X. Xu, *Electrochim. Acta* **2016**, *210*, 905.
[21] C. Dietrich, D. A. Weber, S. J. Sedlmaier, S. Indris, S. P. Culver, D. Walter, J. Janek, W. G. Zeier, *J. Mater. Chem. A* **2017**, *5*, 18111.
[22] Z. Liu, W. Fu, E. A. Payzant, X. Yu, Z. Wu, N. J. Dudney, J. Kiggans, K. Hong, A. J. Rondinone, C. Liang, *J. Am. Chem. Soc.* **2013**, *135*, 975.
[23] a) H. Wang, C. Yu, S. Ganapathy, E. R. H. van Eck, L. van Eijck, M. Wagemaker, *J. Power Sources* **2019**, *412*, 29; b) M. Dahbi, F. Ghamouss, F. Tran-Van, D. Lemordant, M. Anouti, *J. Power Sources* **2011**, *196*, 9743; c) C. H. Choi, W. I. Cho, B. W. Cho, H. S. Kim, Y. S. Yoon, Y. S. Tak, *Electrochem. Solid-State Lett.* **2002**, *5*, A14; d) J. Padarti, K. Nishimura, M. Senna, A. Duevel, P. Heitjans, T. Kawaguchi, N. Sakamoto, N. Wakiya, H. Suzuki, *RSC Adv.* **2016**, *6*, 62656; e) K. Arbi, M. Hoelzel, A. Kuhn, F. García-Alvarado, J. Sanz, *Inorg. Chem.* **2013**, *52*, 9290.
[24] R. Kanno, M. Murayama, *J. Electrochem. Soc.* **2001**, *148*, A742.
[25] P. Parkin Ivan, *Appl. Organomet. Chem.* **2000**, *14*, 227.
[26] N. Zheng, X. Bu, P. Feng, *Nature* **2003**, *426*, 428.
[27] a) A. Sakuda, A. Hayashi, M. Tatsumisago, *Sci. Rep.* **2013**, *3*, 2261; b) A. Sakuda, A. Hayashi, Y. Takigawa, K. Higashi, M. Tatsumisago, *J. Ceram. Soc. Jpn.* **2013***121*, 946.
[28] A. Hayashi, S. Hama, H. Morimoto, M. Tatsumisago, T. Minami, *J. Am. Ceram. Soc.* **2004**, *84*, 477.
[29] F. Mizuno, A. Hayashi, K. Tadanaga, M. Tatsumisago, *Solid State Ionics* **2006**, *177*, 2721.
[30] H.-J. Deiseroth, S.-T. Kong, H. Eckert, J. Vannahme, C. Reiner, T. Zaiß, M. Schlosser, *Angew. Chem., Int. Ed.* **2008**, *47*, 755.
[31] S. P. Ong, Y. Mo, W. D. Richards, L. Miara, H. S. Lee, G. Ceder, *Energy Environ. Sci.* **2013**, *6*, 148.
[32] R. C. Xu, X. H. Xia, Z. J. Yao, X. L. Wang, C. D. Gu, J. P. Tu, *Electrochim. Acta* **2016**, *219*, 235.
[33] Y. Wang, W. D. Richards, S. P. Ong, L. J. Miara, J. C. Kim, Y. Mo, G. Ceder, *Nat. Mater.* **2015**, *14*, 1026.
[34] H. Stephen, *Rep. Prog. Phys.* **2004**, *67*, 1233.
[35] W. Li, G. Wu, C. M. Araújo, R. H. Scheicher, A. Blomqvist, R. Ahuja, Z. Xiong, Y. Feng, P. Chen, *Energy Environ. Sci.* **2010**, *3*, 1524.
[36] B. Zhang, R. Tan, L. Yang, J. Zheng, K. Zhang, S. Mo, Z. Lin, F. Pan, *Energy Storage Mater.* **2018**, *10*, 139.
[37] X. He, Y. Zhu, Y. Mo, *Nat. Commun.* **2017**, *8*, 15893.
[38] Z. Zhang, J. H. Kennedy, *Solid State Ionics* **1990**, *38*, 217.
[39] T. Ohtomo, A. Hayashi, M. Tatsumisago, Y. Tsuchida, S. Hama, K. Kawamoto, *J. Power Sources* **2013**, *233*, 231.
[40] a) J. H. Kennedy, *Mater. Chem. Phys.* **1989**, *23*, 29; b) A. Pradel, M. Ribes, *Solid State Ionics* **1986**, *18-19*, 351.
[41] J. L. Souquet, E. Robinel, B. Barrau, M. Ribes, *Solid State Ionics* **1981**, *3-4*, 317.
[42] M. Tatsumisago, A. Hayashi, *Solid State Ionics* **2012**, *225*, 342.
[43] a) S. Kondo, K. Takada, Y. Yamamura, *Solid State Ionics* **1992**, *53-56*, 1183; b) M. Tatsumisago, K. Hirai, T. Minami, K. Takada, S. Kondo, *J. Ceram. Soc. Jpn.* **1993**, *101*, 1315.
[44] a) M. Tatsumisago, K. Hirai, T. Hirata, M. Takahashi, T. Minami, *Solid State Ionics* **1996**, *86-88*, 487; b) A. Hayashi, M. Tatsumisago, T. Minami, *J. Electrochem. Soc.* **1999**, *146*, 3472.
[45] A. Hayashi, R. Komiya, M. Tatsumisago, T. Minami, *Solid State Ionics* **2002**, *152-153*, 285.
[46] A. Yamauchi, A. Sakuda, A. Hayashi, M. Tatsumisago, *J. Power Sources* **2013**, *244*, 707.
[47] R. Mercier, J.-P. Malugani, B. Fahys, G. Robert, *Solid State Ionics* **1981**, *5*, 663.
[48] S. Ujiie, T. Inagaki, A. Hayashi, M. Tatsumisago, *Solid State Ionics* **2014**, *263*, 57.
[49] J. H. Kennedy, Z. Zhang, H. Eckert, *J. Non-Cryst. Solids* **1990**, *123*, 328.
[50] H. Wada, M. Menetrier, A. Levasseur, P. Hagenmuller, *Mater. Res. Bull.* **1983**, *18*, 189.
[51] C. Dietrich, D. A. Weber, S. Culver, A. Senyshyn, S. J. Sedlmaier, S. Indris, J. Janek, W. G. Zeier, *Inorg. Chem.* **2017**, *56*, 6681.
[52] H. Yamane, M. Shibata, Y. Shimane, T. Junke, Y. Seino, S. Adams, K. Minami, A. Hayashi, M. Tatsumisago, *Solid State Ionics* **2007**, *178*, 1163.
[53] R. Mercier, J. P. Malugani, B. Fahys, G. Robert, J. Douglade, *Acta Crystallogr., Sect. B: Struct. Crystallogr. Cryst. Chem.* **1982**, *38*, 1887.
[54] S. T. Kong, Ö. Gün, B. Koch, H. J. Deiseroth, H. Eckert, C. Reiner, *Chem. - Eur. J.* **2010**, *16*, 5138.
[55] R. Mercier, J. P. Malugani, B. Fahys, J. Douglande, G. Robert, *J. Solid State Chem.* **1982**, *43*, 151.
[56] R.-C. Xu, X.-H. Xia, S.-H. Li, S.-Z. Zhang, X.-L. Wang, J.-P. Tu, *J. Mater. Chem. A* **2017**, *5*, 6310.
[57] F. Mizuno, A. Hayashi, K. Tadanaga, M. Tatsumisago, *Adv. Mater.* **2005**, *17*, 918.
[58] M. Tachez, J.-P. Malugani, R. Mercier, G. Robert, *Solid State Ionics* **1984**, *14*, 181.
[59] K. Homma, M. Yonemura, T. Kobayashi, M. Nagao, M. Hirayama, R. Kanno, *Solid State Ionics* **2011**, *182*, 53.
[60] M. Eom, J. Kim, S. Noh, D. Shin, *J. Power Sources* **2015**, *284*, 44.
[61] E. Rangasamy, Z. Liu, M. Gobet, K. Pilar, G. Sahu, W. Zhou, H. Wu, S. Greenbaum, C. Liang, *J. Am. Chem. Soc.* **2015**, *137*, 1384.
[62] A. Hayashi, K. Minami, M. Tatsumisago, *J. Non-Cryst. Solids* **2009**, *355*, 1919.
[63] S. Wenzel, D. A. Weber, T. Leichtweiss, M. R. Busche, J. Sann, J. Janek, *Solid State Ionics* **2016**, *286*, 24.
[64] C. Winkler, *Ber. Dtsch. Chem. Ges.* **1886**, *19*, 210.
[65] E. Gaudin, H. J. Deiseroth, T. Zaiß, *Z. Kristallogr. - Cryst. Mater.* **2001**, *216*, 39.
[66] a) E. Gaudin, F. Boucher, V. Petricek, F. Taullele, M. Evain, *Acta Crystallogr., Sect. B: Struct. Sci.* **2000**, *56*, 402; b) E. Gaudin, V. Petricek, F. Boucher, F. Taulelle, M. Evain, *Acta Crystallogr., Sect. B: Struct. Sci.* **2000**, *56*, 972.
[67] R. P. Rao, S. Adams, *Phys. Status Solidi A* **2011**, *208*, 1804.
[68] N. J. J. de Klerk, I. Rosłoń, M. Wagemaker, *Chem. Mater.* **2016**, *28*, 7955.
[69] H. M. Chen, C. Maohua, S. Adams, *Phys. Chem. Chem. Phys.* **2015**, *17*, 16494.
[70] P. R. Rayavarapu, N. Sharma, V. K. Peterson, S. Adams, *J. Solid State Electrochem.* **2012**, *16*, 1807.
[71] N. Minafra, S. P. Culver, T. Krauskopf, A. Senyshyn, W. G. Zeier, *J. Mater. Chem. A* **2018**, *6*, 645.
[72] M. A. Kraft, S. Ohno, T. Zinkevich, R. Koerver, S. P. Culver, T. Fuchs, A. Senyshyn, S. Indris, B. J. Morgan, W. G. Zeier, *J. Am. Chem. Soc.* **2018**, *140*, 16330.
[73] Y. Inoue, K. Suzuki, N. Matsui, M. Hirayama, R. Kanno, *J. Solid State Chem.* **2017**, *246*, 334.
[74] H.-J. Deiseroth, J. Maier, K. Weichert, V. Nickel, S.-T. Kong, C. Reiner, *Z. Anorg. Allg. Chem.* **2011**, *637*, 1287.
[75] R. Kanno, T. Hata, Y. Kawamoto, M. Irie, *Solid State Ionics* **2000**, *130*, 97.
[76] I. Seo, S. W. Martin, *Acta Mater.* **2011**, *59*, 1839.
[77] T. Kaib, S. Haddadpour, M. Kapitein, P. Bron, C. Schröder, H. Eckert, B. Roling, S. Dehnen, *Chem. Mater.* **2012**, *24*, 2211.
[78] G. Sahu, Z. Lin, J. Li, Z. Liu, N. Dudney, C. Liang, *Energy Environ. Sci.* **2014**, *7*, 1053.
[79] S. Hori, M. Kato, K. Suzuki, M. Hirayama, Y. Kato, R. Kanno, *J. Am. Ceram. Soc.* **2015**, *98*, 3352.
[80] P. Zhou, J. Wang, F. Cheng, F. Li, J. Chen, *Chem. Commun.* **2016**, *52*, 6091.
[81] Y. Ooura, N. Machida, M. Naito, T. Shigematsu, *Solid State Ionics* **2012**, *225*, 350.
[82] S. Adams, R. P. Rao, *J. Mater. Chem.* **2012**, *22*, 7687.

[83] A. Kuhn, J. Kohler, B. V. Lotsch, *Phys. Chem. Chem. Phys.* **2013**, *15*, 11620.
[84] Y. Mo, S. P. Ong, G. Ceder, *Chem. Mater.* **2012**, *24*, 15.
[85] A. Kuhn, V. Duppel, B. V. Lotsch, *Energy Environ. Sci.* **2013**, *6*, 3548.
[86] P. Bron, S. Dehnen, B. Roling, *J. Power Sources* **2016**, *329*, 530.
[87] J. M. Whiteley, J. H. Woo, E. Hu, K.-W. Nam, S.-H. Lee, *J. Electrochem. Soc.* **2014**, *161*, A1812.
[88] A. Kuhn, O. Gerbig, C. Zhu, F. Falkenberg, J. Maier, B. V. Lotsch, *Phys. Chem. Chem. Phys.* **2014**, *16*, 14669.
[89] D. Lei, K. Shi, H. Ye, Z. Wan, Y. Wang, L. Shen, B. Li, Q.-H. Yang, F. Kang, Y.-B. He, *Adv. Funct. Mater.* **2018**, *28*, 1707570.
[90] A. Hayashi, T. Harayama, F. Mizuno, M. Tatsumisago, *J. Power Sources* **2006**, *163*, 289.
[91] A. Hayashi, T. Harayama, F. Mizuno, M. Tatsumisago, *Solid State Ionics* **2011**, *192*, 130.
[92] S. Kohjiya, T. Kitade, Y. Ikeda, A. Hayashi, A. Matsuda, M. Tatsumisago, T. Minami, *Solid State Ionics* **2002**, 154-155, *1*.
[93] I. Villaluenga, K. H. Wujcik, W. Tong, D. Devaux, D. H. C. Wong, J. M. DeSimone, N. P. Balsara, *Proc. Natl. Acad. Sci. USA* **2016**, *113*, 52.
[94] S. S. Berbano, M. Mirsaneh, M. T. Lanagan, C. A. Randall, *Int. J. Appl. Glass Sci.* **2013**, *4*, 414.
[95] M. Whiteley Justin, P. Taynton, W. Zhang, S.-H. Lee, *Adv. Mater.* **2015**, *27*, 6922.
[96] Y. J. Nam, S.-J. Cho, D. Y. Oh, J.-M. Lim, S. Y. Kim, J. H. Song, Y.-G. Lee, S.-Y. Lee, Y. S. Jung, *Nano Lett.* **2015**, *15*, 3317.
[97] Y. Zhao, C. Wu, G. Peng, X. Chen, X. Yao, Y. Bai, F. Wu, S. Chen, X. Xu, *J. Power Sources* **2016**, *301*, 47.
[98] Z. D. Hood, H. Wang, Y. Li, A. S. Pandian, M. Parans Paranthaman, C. Liang, *Solid State Ionics* **2015**, *283*, 75.
[99] E. Rangasamy, G. Sahu, J. K. Keum, A. J. Rondinone, N. J. Dudney, C. Liang, *J. Mater. Chem. A* **2014**, *2*, 4111.
[100] M. Tatsumisago, T. Minami, *Mater. Chem. Phys.* **1987**, *18*, 1.
[101] J. H. Kennedy, Z. Zhang, *J. Electrochem. Soc.* **1989**, *136*, 2441.
[102] M. Tatsumisago, K. Yoneda, N. Machida, T. Hinami, *J. Non-Cryst. Solids* **1987**, *95-96*, 857.
[103] R. B. Schwarz, C. C. Koch, *Appl. Phys. Lett.* **1986**, *49*, 146.
[104] H. Yamamoto, N. Machida, T. Shigematsu, *Solid State Ionics* **2004**, *175*, 707.
[105] Z. Zhang, L. Zhang, Y. Liu, C. Yu, X. Yan, B. Xu, L.-m. Wang, *J. Alloys Compd.* **2018**, *747*, 227.
[106] C. Yu, L. van Eijck, S. Ganapathy, M. Wagemaker, *Electrochim. Acta* **2016**, *215*, 93.
[107] a) S. Teragawa, K. Aso, K. Tadanaga, A. Hayashi, M. Tatsumisago, *J. Power Sources* **2014**, *248*, 939; b) S. Teragawa, K. Aso, K. Tadanaga, A. Hayashi, M. Tatsumisago, *J. Mater. Chem. A* **2014**, *2*, 5095.
[108] X. Yao, D. Liu, C. Wang, P. Long, G. Peng, Y.-S. Hu, H. Li, L. Chen, X. Xu, *Nano Lett.* **2016**, *16*, 7148.
[109] D. H. Kim, D. Y. Oh, K. H. Park, Y. E. Choi, Y. J. Nam, H. A. Lee, S.-M. Lee, Y. S. Jung, *Nano Lett.* **2017**, *17*, 3013.
[110] T. Inada, K. Takada, A. Kajiyama, M. Kouguchi, H. Sasaki, S. Kondo, M. Watanabe, M. Murayama, R. Kanno, *Solid State Ionics* **2003**, *158*, 275.
[111] N. H. H. Phuc, M. Totani, K. Morikawa, H. Muto, A. Matsuda, *Solid State Ionics* **2016**, *288*, 240.
[112] N. H. H. Phuc, K. Morikawa, T. Mitsuhiro, H. Muto, A. Matsuda, *Ionics* **2017**, *23*, 2061.
[113] S. Ito, M. Nakakita, Y. Aihara, T. Uehara, N. Machida, *J. Power Sources* **2014**, *271*, 342.
[114] E. Choi Young, H. Park Kern, H. Kim Dong, Y. Oh Dae, R. Kwak Hi, Y.-G. Lee, S. Jung Yoon, *ChemSusChem* **2017**, *10*, 2605.
[115] H. Park Kern, Y. Oh Dae, E. Choi Young, J. Nam Young, L. Han, J.-Y. Kim, H. Xin, F. Lin, M. Oh Seung, S. Jung Yoon, *Adv. Mater.* **2016**, *28*, 1874.
[116] Y. Seino, T. Ota, K. Takada, A. Hayashi, M. Tatsumisago, *Energy Environ. Sci.* **2014**, *7*, 627.
[117] F. Han, Y. Zhu, X. He, Y. Mo, C. Wang, *Adv. Energy Mater.* **2016**, *6*, 1501590.
[118] Y. Zhu, X. He, Y. Mo, *ACS Appl. Mater. Interfaces* **2015**, *7*, 23685.
[119] L. Sang, R. T. Haasch, A. A. Gewirth, R. G. Nuzzo, *Chem. Mater.* **2017**, *29*, 3029.
[120] F. Wu, W. Fitzhugh, L. Ye, J. Ning, X. Li, *Nat. Commun.* **2018**, *9*, 4037.
[121] Y. Zhu, X. He, Y. Mo, *J. Mater. Chem. A* **2016**, *4*, 3253.
[122] J. Haruyama, K. Sodeyama, L. Han, K. Takada, Y. Tateyama, *Chem. Mater.* **2014**, *26*, 4248.
[123] a) A. Zhamu, G. Chen, C. Liu, D. Neff, Q. Fang, Z. Yu, W. Xiong, Y. Wang, X. Wang, B. Z. Jang, *Energy Environ. Sci.* **2012**, *5*, 5701; b) D. Aurbach, E. Zinigrad, H. Teller, P. Dan, *J. Electrochem. Soc.* **2000**, *147*, 1274.
[124] J. M. Tarascon, M. Armand, *Nature* **2001**, *414*, 359.
[125] N. Nitta, F. Wu, J. T. Lee, G. Yushin, *Mater. Today* **2015**, *18*, 252.
[126] S. Wenzel, T. Leichtweiss, D. Krüger, J. Sann, J. Janek, *Solid State Ionics* **2015**, *278*, 98.
[127] S. Wenzel, S. J. Sedlmaier, C. Dietrich, W. G. Zeier, J. Janek, *Solid State Ionics* **2018**, *318*, 102.
[128] S. Wenzel, S. Randau, T. Leichtweiß, D. A. Weber, J. Sann, W. G. Zeier, J. Janek, *Chem. Mater.* **2016**, *28*, 2400.
[129] Y. Gao, D. Wang, Y. C Li, Z. Yu, T. E Mallouk, D. Wang, *Angew. Chem., Int. Ed.* **2018**, *57*, 13608.
[130] N. D. Lepley, N. A. W. Holzwarth, Y. A. Du, *Phys. Rev. B* **2013**, *88*, 104103.
[131] T. Yamada, S. Ito, R. Omoda, T. Watanabe, Y. Aihara, M. Agostini, U. Ulissi, J. Hassoun, B. Scrosati, *J. Electrochem. Soc.* **2015**, *162*, A646.
[132] L. Sang, K. L. Bassett, F. C. Castro, M. J. Young, L. Chen, R. T. Haasch, J. W. Elam, V. P. Dravid, R. G. Nuzzo, A. A. Gewirth, *Chem. Mater.* **2018**, *30*, 8747.
[133] X. Yao, N. Huang, F. Han, Q. Zhang, H. Wan, J. P. Mwizerwa, C. Wang, X. Xu, *Adv. Energy Mater.* **2017**, *7*, 1602923.
[134] S. Choudhury, Z. Tu, S. Stalin, D. Vu, K. Fawole, D. Gunceler, R. Sundararaman, A. Archer Lynden, *Angew. Chem., Int. Ed.* **2017**, *56*, 13070.
[135] K. Takada, N. Aotani, K. Iwamoto, S. Kondo, *Solid State Ionics* **1996**, *86-88*, 877.
[136] M. Nagao, A. Hayashi, M. Tatsumisago, *Electrochem. Commun.* **2012**, *22*, 177.
[137] W. D. Richards, L. J. Miara, Y. Wang, J. C. Kim, G. Ceder, *Chem. Mater.* **2016**, *28*, 266.
[138] J. Auvergniot, A. Cassel, J.-B. Ledeuil, V. Viallet, V. Seznec, R. Dedryvère, *Chem. Mater.* **2017**, *29*, 3883.
[139] A. Sakuda, A. Hayashi, M. Tatsumisago, *Chem. Mater.* **2010**, *22*, 949.
[140] S. Chen, D. Xie, G. Liu, J. P. Mwizerwa, Q. Zhang, Y. Zhao, X. Xu, X. Yao, *Energy Storage Mater.* **2018**, *14*, 58.
[141] R. Koerver, I. Aygün, T. Leichtweiß, C. Dietrich, W. Zhang, J. O. Binder, P. Hartmann, W. G. Zeier, J. Janek, *Chem. Mater.* **2017**, *29*, 5574.
[142] C. Wang, X. Li, Y. Zhao, M. Norouzi Banis, J. Liang, X. Li, Y. Sun, K. R. Adair, Q. Sun, Y. Liu, F. Zhao, S. Deng, X. Lin, R. Li, Y. Hu, T. K. Sham, H. Huang, L. Zhang, R. Yang, X. Sun, *Small Methods* **2019**, *3*, 1900261.
[143] N. Ohta, K. Takada, I. Sakaguchi, L. Zhang, R. Ma, K. Fukuda, M. Osada, T. Sasaki, *Electrochem. Commun.* **2007**, *9*, 1486.
[144] N. Ohta, K. Takada, L. Zhang, R. Ma, M. Osada, T. Sasaki, *Adv. Mater.* **2006**, *18*, 2226.
[145] H. Kitaura, A. Hayashi, K. Tadanaga, M. Tatsumisago, *Solid State Ionics* **2011**, *192*, 304.
[146] K. Takada, N. Ohta, L. Zhang, K. Fukuda, I. Sakaguchi, R. Ma, M. Osada, T. Sasaki, *Solid State Ionics* **2008**, *179*, 1333.

[147] T. Kato, T. Hamanaka, K. Yamamoto, T. Hirayama, F. Sagane, M. Motoyama, Y. Iriyama, *J. Power Sources* **2014**, *260*, 292.
[148] A. Sakuda, H. Kitaura, A. Hayashi, K. Tadanaga, M. Tatsumisago, *Electrochem. Solid-State Lett.* **2008**, *11*, A1.
[149] a) Y. Jin, N. Li, C. H. Chen, S. Q. Wei, *Electrochem. Solid-State Lett.* **2006**, *9*, A273; b) Y. Ito, Y. Sakurai, S. Yubuchi, A. Sakuda, A. Hayashi, M. Tatsumisago, *J. Electrochem. Soc.* **2015**, *162*, A1610.
[150] N. Machida, J. Kashiwagi, M. Naito, T. Shigematsu, *Solid State Ionics* **2012**, *225*, 354.
[151] J. H. Woo, J. J. Travis, S. M. George, S.-H. Lee, *J. Electrochem. Soc.* **2015**, *162*, A344.
[152] K. H. Park, Q. Bai, D. H. Kim, D. Y. Oh, Y. Zhu, Y. Mo, Y. S. Jung, *Adv. Energy Mater.* **2018**, *8*, 1800035.
[153] S. Hoo Jung, K. Oh, Y. Jin Nam, D. Y. Oh, P. Brüner, K. Kang, Y. S. Jung, *Chem. Mater.* **2018**, *30*, 8190.
[154] K. Nagao, A. Hayashi, M. Tatsumisago, *J. Ceram. Soc. Jpn.* **2016**, *124*, 915.
[155] a) T. Kobayashi, Y. Imade, D. Shishihara, K. Homma, M. Nagao, R. Watanabe, T. Yokoi, A. Yamada, R. Kanno, T. Tatsumi, *J. Power Sources* **2008**, *182*, 621; b) M. Agostini, Y. Aihara, T. Yamada, B. Scrosati, J. Hassoun, *Solid State Ionics* **2013**, *244*, 48.
[156] M. Nagao, Y. Imade, H. Narisawa, T. Kobayashi, R. Watanabe, T. Yokoi, T. Tatsumi, R. Kanno, *J. Power Sources* **2013**, *222*, 237.
[157] a) Q. Wang, J. Jin, X. Wu, G. Ma, J. Yang, Z. Wen, *Phys. Chem. Chem. Phys.* **2014**, *16*, 21225; b) M. Hagen, S. Dörfler, H. Althues, J. Tübke, M. J. Hoffmann, S. Kaskel, K. Pinkwart, *J. Power Sources* **2012**, *213*, 239.
[158] M. Eom, S. Son, C. Park, S. Noh, W. T. Nichols, D. Shin, *Electrochim. Acta* **2017**, *230*, 279.
[159] H. Muramatsu, A. Hayashi, T. Ohtomo, S. Hama, M. Tatsumisago, *Solid State Ionics* **2011**, *182*, 116.
[160] A. Hayashi, H. Muramatsu, T. Ohtomo, S. Hama, M. Tatsumisago, *J. Alloys Compd.* **2014**, *591*, 247.
[161] C. L. Carnes, K. J. Klabunde, *Chem. Mater.* **2002**, *14*, 1806.
[162] A. Hayashi, H. Muramatsu, T. Ohtomo, S. Hama, M. Tatsumisago, *J. Mater. Chem. A* **2013**, *1*, 6320.
[163] M. Nagao, A. Hayashi, M. Tatsumisago, *J. Mater. Chem.* **2012**, *22*, 10015.
[164] A. Sakuda, A. Hayashi, T. Ohtomo, S. Hama, M. Tatsumisago, *Electrochem. Solid-State Lett.* **2010**, *13*, A73.
[165] H. Kitaura, A. Hayashi, T. Ohtomo, S. Hama, M. Tatsumisago, *J. Mater. Chem.* **2011**, *21*, 118.
[166] S. Noh, W. T. Nichols, M. Cho, D. Shin, *J. Electroceram.* **2018**, *40*, 293.
[167] D. Y. Oh, D. H. Kim, S. H. Jung, J.-G. Han, N.-S. Choi, Y. S. Jung, *J. Mater. Chem. A* **2017**, *5*, 20771.
[168] M. Yamamoto, M. Takahashi, Y. Terauchi, Y. Kobayashi, S. Ikeda, A. Sakuda, *J. Ceram. Soc. Jpn.* **2017**, *125*, 391.
[169] S.-J. Choi, S.-H. Choi, A. D. Bui, Y.-J. Lee, S.-M. Lee, H.-C. Shin, Y.-C. Ha, *ACS Appl. Mater. Interfaces* **2018**, *10*, 31404.
[170] Y. J. Nam, D. Y. Oh, S. H. Jung, Y. S. Jung, *J. Power Sources* **2018**, *375*, 93.
[171] T. Inada, K. Takada, A. Kajiyama, H. Sasaki, S. Kondo, M. Watanabe, M. Murayama, R. Kanno, *J. Power Sources* **2003**, *119–121*, 948.
[172] T. Inada, T. Kobayashi, N. Sonoyama, A. Yamada, S. Kondo, M. Nagao, R. Kanno, *J. Power Sources* **2009**, *194*, 1085.
[173] F. Strauss, T. Bartsch, L. de Biasi, A. Y. Kim, J. Janek, P. Hartmann, T. Brezesinski, *ACS Energy Lett.* **2018**, *3*, 992.
[174] F. Han, T. Gao, Y. Zhu, K. J. Gaskell, C. Wang, *Adv. Mater.* **2015**, *27*, 3473.
[175] S. Boulineau, M. Courty, J.-M. Tarascon, V. Viallet, *Solid State Ionics* **2012**, *221*, 1.
[176] K. Minami, A. Hayashi, S. Ujiie, M. Tatsumisago, *Solid State Ionics* **2011**, *192*, 122.
[177] A. Hwang, *Int. J. Electrochem. Sci.* **2017**, *12*, 7795.
[178] M. Nagao, A. Hayashi, M. Tatsumisago, *Energy Technol.* **2013**, *1*, 186.
[179] H. Nagata, Y. Chikusa, *J. Power Sources* **2014**, *263*, 141.
[180] S. Kinoshita, K. Okuda, N. Machida, T. Shigematsu, *J. Power Sources* **2014**, *269*, 727.
[181] M. Nagao, K. Suzuki, Y. Imade, M. Tateishi, R. Watanabe, T. Yokoi, M. Hirayama, T. Tatsumi, R. Kanno, *J. Power Sources* **2016**, *330*, 120.
[182] M. Chen, S. Adams, *J. Solid State Electrochem.* **2015**, *19*, 697.
[183] R. Xu, Z. Wu, S. Zhang, X. Wang, Y. Xia, X. Xia, X. Huang, J. Tu, *Chem. - Eur. J.* **2017**, *23*, 13950.
[184] N. Tanibata, H. Tsukasaki, M. Deguchi, S. Mori, A. Hayashi, M. Tatsumisago, *J. Mater. Chem. A* **2017**, *5*, 11224.
[185] D. Y. Oh, Y. E. Choi, D. H. Kim, Y.-G. Lee, B.-S. Kim, J. Park, H. Sohn, Y. S. Jung, *J. Mater. Chem. A* **2016**, *4*, 10329.
[186] R. C. Xu, X. L. Wang, S. Z. Zhang, Y. Xia, X. H. Xia, J. B. Wu, J. P. Tu, *J. Power Sources* **2018**, *374*, 107.
[187] Z. Lin, Z. Liu, N. J. Dudney, C. Liang, *ACS Nano* **2013**, *7*, 2829.
[188] M. Nagao, A. Hayashi, M. Tatsumisago, *Electrochim. Acta* **2011**, *56*, 6055.
[189] a) C. Peng, G.-H. Ning, J. Su, G. Zhong, W. Tang, B. Tian, C. Su, D. Yu, L. Zu, J. Yang, M.-F. Ng, Y.-S. Hu, Y. Yang, M. Armand, K. P. Loh, *Nat. Energy* **2017**, *2*, 17074; b) Y. Liang, Z. Tao, J. Chen, *Adv. Energy Mater.* **2012**, *2*, 742; c) B. Häupler, A. Wild, U. S. Schubert, *Adv. Energy Mater.* **2015**, *5*, 1402034.
[190] C. Luo, X. Ji, J. Chen, K. J. Gaskell, X. He, Y. Liang, J. Jiang, C. Wang, *Angew. Chem., Int. Ed.* **2018**, *57*, 8567.
[191] a) C. Luo, R. Huang, R. Kevorkyants, M. Pavanello, H. He, C. Wang, *Nano Lett.* **2014**, *14*, 1596; b) H. Chen, M. Armand, M. Courty, M. Jiang, C. P. Grey, F. Dolhem, J.-M. Tarascon, P. Poizot, *J. Am. Chem. Soc.* **2009**, *131*, 8984; c) S. Muench, A. Wild, C. Friebe, B. Häupler, T. Janoschka, U. S. Schubert, *Chem. Rev.* **2016**, *116*, 9438.
[192] Y. Zhang, R. Chen, T. Liu, B. Xu, X. Zhang, L. Li, Y. Lin, C.-W. Nan, Y. Shen, *ACS Appl. Mater. Interfaces* **2018**, *10*, 10029.
[193] A. Sakuda, K. Kuratani, M. Yamamoto, M. Takahashi, T. Takeuchi, H. Kobayashi, *J. Electrochem. Soc.* **2017**, *164*, A2474.

